7-1-2016

CO2 Flux Along Faults of the Central Rio Grande Rift, New Mexico

Jared Smith

Recommended Citation

Smith, Jared. "CO2 Flux Along Faults of the Central Rio Grande Rift, New Mexico." (2016). https://digitalrepository.unm.edu/eps_etds/108

Jared R. Smith
Candidate

Earth and Planetary Sciences
Department

This thesis is approved, and it is acceptable in quality and form for publication:

Approved by the Thesis Committee:

Dr. Karl E. Karlstrom

Dr. Laura J. Crossey

Dr. Lindsay L. Worthington

CO_2 FLUX ALONG FAULTS OF THE CENTRAL RIO GRANDE RIFT, NEW MEXICO

by

JARED R. SMITH

B.S. GEOLOGY, UNIVERSITY OF OKLAHOMA

THESIS

Submitted in Partial Fulfillment of the
Requirement for the Degree of

Master of Science
Earth and Planetary Sciences

The University of New Mexico
Albuquerque, New Mexico

July 2016

Acknowledgements

I would like to thank the Earth and Planetary Sciences Department for giving me the opportunity to further my academic career. I wish to thank my committee for their ideas and direction over these two years. I would like to thank Tobias Fischer and Hyunwoo Lee for generously donated their resources and time for collected gas samples and understanding the CO_2 flux method. I would like to thank Laura Crossey for her enthusiasm for geochemistry and being a great mentor both on and off the academic field; I would not have been a part of the EPS family without her. I would like to thank Karl Karlstrom for his wisdom and guidance for understanding Earth systems, and always being available to meet anytime for questions. Thank you Tanner Grulke, Graham Thomas, Valerie Blomgren, Mark Holland, Hitesh Changela, Jeff Hrncir, Tehnuka Ilanko, Brad Jeffrey, Vanessa Ward, and Rayanna Benally, and Holly Smith for helping me collect CO_2 flux measurements. Thank you to EPSCoR for funding the instrument used to conduct this research. Thank you Bruce Black for donating your time and knowledge about the subsurface of the northern Albuquerque basin. I would like to thank my parents Bill and Jean Smith for the support they have given me during my lifetime, I would not have made it this far without them. Finally, I would like to thank my wife for being so supportive and understanding when it came to all the academic hours spent away from home, I love you.

CO_2 FLUX ALONG FAULTS OF THE CENTRAL RIO GRANDE RIFT, NEW MEXICO

By

Jared R. Smith

B.S. Geology, University of Oklahoma, 2012

M.S., Earth and Planetary Sciences, University of New Mexico, 2016

Abstract

The Albuquerque basin, a part of the central Rio Grande rift, is host to a complex fault network that influences deep and shallow fluid migration. This study examines CO_2 flux along these faults at the northern and western borders with the Valles caldera and San Juan basin, using a CO_2 flux device with an accumulation chamber (PP-Systems). These major and minor Quaternary faults have damage zones that can influence CO_2 degassing, hydrocarbon migration, and groundwater flow and mixing, including geothermal waters related to the Valles caldera geothermal system, ultimately acting as conduits or barriers to fluid flow. Rift systems are known to emit significant amounts of CO_2 to the atmosphere, and the location of the central Rio Grande rift accompanied by a relatively recent caldera eruption and the Jemez Volcanic Lineament make this area a field laboratory for examining links between the mantle and surface. To test these hypotheses, 8 sites were targeted, the first 6 of which have springs located along faults: 1) The Valles caldera geothermal system at Sulphur Springs, 2) CO_2 rich springs in the caldera at Alamo Canyon, 3) The Soda Dam area of the Valles geothermal outflow plume, 4) Travertine springs of Penasco Springs on the Nacimiento fault, 5) Travertine

springs at San Ysidro on the Nacimiento fault, and 6) Travertine springs at Carrizo Arroyo on western rift bounding faults in the area of the Socorro magma body. Two cemented fault zone sites were also targeted: 7) Four faults at the Santa Ana Fault network on the Zia Pueblo and 8) the carbonate cemented Sand Hill fault. There were over 600 CO_2 flux measurements taken, in units of grams of CO_2 per square meter per day (g_{CO2}/m^2d). Collectively, these sites provide a set of transects that allows comparison of CO_2 flux from springs and faults north (Alamo Canyon) to south (Carrizo Arroyo) with increasing distance away from the Valles caldera (~ 135 km).

Cumulative probability plots were utilized to classify CO_2 flux in terms of local background, diffuse, and high point source fluxes (HPSF) at each site. Local background at each site ranges from 0.7 – 4.0 g_{CO2}/m^2d (Alamo Canyon), 0.2 – 2.8 g_{CO2}/m^2d (Soda Dam), 0.0 – 2.5 g_{CO2}/m^2d (Penasco Springs), 0.0 – 1.3 g_{CO2}/m^2d (San Ysidro), 0.0 – 1.7 g_{CO2}/m^2d (Zia Pueblo), 0.0 – 1.1 g_{CO2}/m^2d (Sand Hill Fault), and 0.0 – 1.0 g_{CO2}/m^2d (Carrizo Arroyo). Background at Sulphur Springs was uniformly high, possibly the results of an enhanced fault damage zone coupled with an active geothermal system that influences the entire area where measurements were taken.

Above background CO_2 fluxes are observed in areas around fault zones and are termed diffuse. These moderate CO_2 fluxes may be the result of multiple processes surrounding fluid migration and the degassing of CO_2 on the surface. A considerable number of these moderate fluxes were measured at most sites except for the carbonate cemented faults at the Zia Pueblo, where one measurement is attributed to a diffuse flux on a silica cemented fault (9.6 g_{CO2}/m^2d). Diffuse CO_2 flux at each site ranged from 15.5 – 1,778 g_{CO2}/m^2d (Alamo Canyon), 8.6 – 60.3 g_{CO2}/m^2d (Sulphur Springs), 2.8 – 32.4

g_{CO2}/m^2d (Soda Dam), 4.0 – 13.2 g_{CO2}/m^2d (Penasco Springs), 1.3 – 5.1 g_{CO2}/m^2d (San Ysidro), 1.7 – 9.6 g_{CO2}/m^2d (Zia Pueblo), 2.5 – 7.7 g_{CO2}/m^2d (Sand Hill Fault), and 2.5 – 11.3 g_{CO2}/m^2d (Carrizo Arroyo). Relatively high diffuse fluxes measured at most sites attests to fault damage zones providing pathways for volatiles, whereas low or background fluxes measured along faults may indicate barriers to fluid flow.

High CO_2 fluxes (HPSF) are attributed to the migration of fluids along fault damage zones where the degassing of CO_2 occurs directly over the fault or at the intersection of multiple faults. The HPSF are most likely a combination of three types of fluxes (background, diffuse, and HPSF) with a more significant CO_2 flux from deeper and/or distal sources. These are typically measured at carbonic springs, but HPSF were also measured on dry surfaces at Sulphur Springs, Soda Dam, Penasco Springs, and San Ysidro. HPSF range from 1,778 - 144, 239 g_{CO2}/m^2d (Alamo Canyon), 302 – 170,122 g_{CO2}/m^2d (Sulphur Springs), 200 – 9,675 g_{CO2}/m^2d (Soda Dam), 13.2 – 2,400 (Penasco Springs), and 42.7 – 149,322 g_{CO2}/m^2d (San Ysidro). No HPSF were measured at Zia Pueblo, Sand Hill fault, or Carrizo Arroyo. The Zia Pueblo site hosts tight carbonate and silica cemented faults that block CO_2 degassing on the surface. Sand Hill fault and Carrizo Arroyo may not have any HPSF, however, large amounts of diffuse flux attest to permeability along the fault zones.

CO_2 flux measurements were conducted across various geologic areas and environments over relatively wide distances. The total annual CO_2 flux (in tons/year) for each site was calculated based on fault damage zone areas and distal damage zone areas. The total annual CO_2 flux from two areas at the Valles caldera (Alamo Canyon and Sulphur Springs) were calculated to be $9.1x10^5$ t/y (total area of evaluation ~ $3.15x10^5$

m^2), at 4 areas in the Albuquerque basin (PS, SY, SHF, and CA) to be 5.4×10^5 t/y (total area of evaluation ~ 9.1×10^5 m^2), and at 1 area in between these two locations (Soda Dam) to be 1,856 t/y (total area of evaluation ~ 3.2×10^4 m^2). When compared to other geothermal and magmatic sites such as Yellowstone and the East African rift, the Valles caldera and Albuquerque basin faults provide pathways for significant amounts of CO_2 degassing from the solid Earth. Gas analyses ($^3He/^4He$ ratios, carbon isotopes, and whole gas analyses) show there are components of CO_2 from a magmatic source (i.e. endogenic). It is clear that the initiation of major extension along the Rio Grande rift and the eruption of volcanoes along the Jemez Volcanic Lineament contribute significantly to the CO_2 that is degassing along structures at the Albuquerque basin and Valles caldera, and have been a significant source of CO_2 to the atmosphere over millions of years.

Table of Contents

List of Figures

List of Tables

List of Appendices

1. Introduction

This paper reports the first effort to conduct CO_2 gas flux surveys across faults and springs in the Albuquerque basin and Valles caldera geothermal system of the Rio Grande rift (RGR). The northern Albuquerque basin resides at the confluence of potential geothermal, hydrocarbon, and water resources. The Valles caldera geothermal system was the location for the first hot dry rock geothermal experiment (Goff and Janik, 2002), and has geologically influenced its surroundings in terms of volcanic rock deposition (i.e. Bandelier Tuff), faults and fracture networks, and aquifers. These geologic and socioeconomically important regions are the focus of this study because they provide a field laboratory for examining links between mantle degassing and faults as fluid conduits and/or barriers to volatile flux. To address this issue, CO_2 flux (g_{CO2}/m^2d) measurements were taken at 8 sites in the Valles caldera geothermal system and adjacent areas (Alamo Canyon - AC, Sulphur Springs – SS, and Soda Dam – SD) and Albuquerque basin (Penasco Springs – PS, San Ysidro – SY, Zia Pueblo – ZP, Sand Hill Fault – SHF, and Carrizo Arroyo – CA; Figure 1).

CO_2 degassing at the surface can be derived from multiple sources: anthropogenic, plant respiration, soil gas, carbonate dissolution, and deeper geological sources such as magmatism. The of this study is to characterize CO_2 degassing from the solid earth that takes place through springs and faults of the central RGR. Measuring CO_2 flux across the surface of the Earth can be applied to academic and industrial exploration. In tectonically active settings, high surface CO_2 fluxes may indicate the presence of a deep fault system that conveys volatiles from Earth's mantle (Lewicki and Brantley, 2000; Lewicki et al, 2003; Werner et al., 2008; Crossey et al., 2009; Lee et al., 2016). In magmatic systems, high surface CO_2 flux is often associated with the presence of a fault that facilitates geothermal fluid migration and circulation related to geothermal resources at depth (Chiodini et al., 2007). The central RGR is host to active tectonic (Albuquerque basin; Ricketts et al., 2014) and magmatic (Valles caldera; Goff et al., 1985; Zimmerer et al., 2016a) regimes that may have significant CO_2 signatures. This study uses CO_2 flux measurements collected by a hand held meter (Chiodini et al., 1998) to provide information for the location of permeable or impermeable faults, classify fault zones, assess potential geothermal activity and resources, and provide further constraints for sources of CO_2 degassing from the solid Earth, an important baseline for quantifying anthropogenic CO_2 contributions (Kerrick, 2001; Lee et al., 2016).

To quantify CO_2 flux across faults and in different parts of the Albuquerque basin and Valles caldera geothermal system, there were three levels of CO_2 flux identified. These are: 1) background flux, 2) diffuse flux, and 3) high point source fluxes (HPSF) localized around hot springs, carbonic cool spring vents, and travertine deposits. To evaluate potential sources for these CO_2 fluxes a combination of surface water geochemistry, gas geochemistry, and geology were used to create a more detailed fault network map. This is useful for assessing the distribution and differential values of CO_2 flux along faults and in different settings in the Albuquerque basin and Valles caldera.

Previous studies suggested that the Valles caldera geothermal system may have an influential role in providing high CO_2 to help explain the travertine deposition and carbonic warm springs as far southwest as San Ysidro and Penasco Springs (McGibbon, 2015) and as far northeast as Ojo Caliente spring (Blomgren, 2016). If so, there may be higher flux near the Valles geothermal system and decrease away from it. Alternatively, there is also a tectonic component from the RGR itself, both faults and the Socorro magma body, that may be contributing magmatic CO_2 to the surface. The long term goal of this study is to use CO_2 flux measurements of the type pioneered here, in combination with water and gas chemistry of springs, to investigate CO_2 degassing patterns in the northern Albuquerque basin and Valles caldera. By better characterizing ongoing neotectonics related to magmatism, fault conduits, active rifting, and geothermal activity one can better understand the sources and transport of gases emitted at the surface.

Finally, another motivation for this study is that Mesozoic and Paleozoic formations below the Albuquerque basin may contain a substantial amount of hydrocarbons (Black, 2002; Black, 2013). These hydrocarbons have migrated along faults and permeable layers, where they have become locally trapped within structural highs associated with Laramide basement uplifts that have now been down-faulted beneath Santa Fe Group cover (Black, 2002; Black, 2013). Studying potential hydrocarbon emissions (i.e. CH_4) along faults may provide more evidence for hydrocarbon reservoirs and permeable faults that are transferring these fluids.

2. Geologic Background

2.1. Regional Geologic Background

The Albuquerque basin is a major asymmetrical (Russell and Snelson, 1994) sedimentary basin oriented with a northern half graben tilted down to the east and a southern half graben tilted down to the west (Chapin and Cather, 1994). It is a part of the RGR, a late Cenozoic continental rift system trending north-south from southern Colorado though central New Mexico and into northern Mexico (Chapin, 1971; Keller and Baldridge, 1999). Continental extension of the RGR started ca. 36-37 Ma with the thinning and stretching of Earth's crust in a westerly direction between the Colorado Plateau (west) and the Great Plains (east) provinces (Kelley and Chamberlin, 2012; Ricketts, Karlstrom, and Kelley, 2015). The upper crust of the RGR consists of interconnected structural basins (usually half grabens) filled with thick deposits of clastic sediments and local interbedded basalt flows (Grauch and Connell, 2013). A simplified map of the geology surrounding the Albuquerque basin and Valles caldera is shown in Figure 1.

The age and evolution of the Albuquerque basin are constrained by syn-rift sediments known as the Santa Fe Group, and ages of movement on flanking structures. The Santa Fe Group sediments were deposited on top of Mesozoic and Paleozoic bedrock during the late Oligocene (Grauch and Connell, 2013 – Appendix A) and early Miocene (Connell, Koning, and Cather, 1999) through early Quaternary. Reverse faults reactivated as normal faults along the eastern flanking mountains and northwestern border of the Albuquerque basin indicate continental extension due to tectonism during the early Miocene (Karlstrom et al., 1999). Presently, the Albuquerque basin is bordered by the Colorado Plateau to the west, the Jemez Mountains and Espanola basin to the north, Sandia Mountains and Great Plains to the east, and Socorro magma body to the south. Recent studies suggest that overall extensional deformation is still active at very slow strain rates (Berglund et al., 2012), except in localized areas around spring and groundwater systems that can enhance strain rates (Ricketts et al., 2014).

Parts of the RGR and the intersecting Jemez Volcanic Lineament have been active in the Quaternary. The last two major caldera eruptions occurred 1.6 Ma depositing the

Otowi Member (from the collapse of the Toledo caldera) and 1.26 Ma depositing the Tshirege Member (from the eruption of the Valles caldera), both members of the Bandelier Tuff (Spell, Kyle, and Baker, 1996; Goff, 2009; Phillips et al., 2007; Zimmerer et al., 2016a). Continued magmatic activity has persisted until 68 ka, and there is still a magma body and active geothermal system in the SW part of the Valles caldera (Zimmerer et al., 2016b). The Jemez caldera eruptions are located where the NE trending zone of volcanism known as the Jemez Volcanic Lineament (Heiken et al., 1990) crosses the RGR. The Jemez volcanic fields began erupting basaltic and rhyolitic magmas more than 13 Ma (Heiken et al., 1990) with the most recent eruption occurring 68 ka (Zimmerer et al., 2016a; 2016b). Figure 2 shows mantle tomography (shear-waves) at 60 km depth where there is a zone of low mantle velocity that contains partial melt along the Jemez Volcanic Lineament and RGR; compared to higher velocity mantle beneath bounding physiographic regions of the Colorado Plateau to the west and Great Plains to the east (Schmandt and Lin, 2014).

Figure 2 also plots $^3He/^4He$ values measured from springs and wells in northern New Mexico (Karlstrom et al., 2013; Blomgren, 2016, Crossey, et al., 2015). This map shows that nearly all the samples collected at carbonic springs in the region have $^3He/^4He$ values greater than 0.1 R_A indicating the presence of mantle-derived helium in the spring waters. Hot springs and wells from the Valles caldera show values up to 6 R_A which approach MORB values of 8 ± 1 R_A (Gautheron and Moreira, 2002). $^3He/^4He$ values decrease systematically both NE and SW of the Valles caldera to distal values of 0.1-0.2 R_A (McGibbon et al., 2015, Blomgren, 2016, Crossey et al., 2015). This motivated the choice of sites for CO_2 flux measurements, and to test whether there would be detectable decreases of CO_2 flux with distance from the Caldera, versus whether fault conduits throughout the rift may be zones of high CO_2 flux.

The stratigraphy associated with all of the Albuquerque basin sites is shown in Appendix A and a cross section through the northern Albuquerque basin was constructed and shown in Figure 3. The major aquifer resides in the Santa Fe Group system, and supplies the groundwater resources for the Albuquerque metropolitan area and surrounding communities within the Albuquerque basin (Bartolino and Cole, 2002). Brines entering the Albuquerque basin are indicated by high concentrations of chlorine sourced from Paleozoic rocks (Plummer et al., 2012), and sulfate (SO_4) sourced from gypsum in Mesozoic rocks (Plummer et al., 2012, McGibbon, 2015). Fluids circulating through these rocks are transported to the surface along faults, indicating other complex hydrostratigraphic sources of water in the Albuquerque basin.

2.2. Local Sites: geologic and hydrologic Background

The 8 study sites follow fault networks that lead from the Valles caldera down along the western and northern edges of the Albuquerque basin towards the southern end of the Albuquerque basin (Figure 1). From north to south these are Alamo Canyon (AC), Sulphur Springs (SS), Soda Dam (SD), Penasco Springs (PS), Zia Pueblo (ZP), San Ysidro (SY), Sand Hill Fault (SHF), and Carrizo Arroyo (CA). Several of the sites have springs that are depositing travertine including: SD, PS, and SY. The deposition of travertine along active fault settings has been well discussed in Hancock et al. 1999. Their findings suggest that the fissure-ridge style travertine deposits, as seen at SD and SY (Figures 3 and 5) in the Valles caldera and Albuquerque basin, respectively, occur along intersecting normal faults where there are also high CO_2 fluxes (Hancock et al., 1999). There is also a significant correlation of travertines preferentially depositing on the hanging wall side of normal faults at sites, however, there are instances where deposits have been found on the footwall side (Hancock et al., 1999).

2.2.1. Alamo Canyon

The Valles caldera sites (including AC and SS), have large magmatic signatures in their gases, as seen by the large $^3He/^4He$ (1.01 – 6.0 R_A). Depth to the magma chamber below the Redondo resurgent dome was estimated by Brothelande and Merle (2015) to be 3.4 km, using an approximate fault dip of 60 degrees. This sets a limit for the depths of Quaternary faults in the Valles caldera to access this magma chamber. AC is approximately 1.75 km northeast of SS and has numerous faults trending both N-S and E-W. The two main faults pass through the marsh-like valley and intersect with two N-S trending faults to the west, and possibly one inferred fault to the east (Figure 10). The surface geology through the valley consists of Quaternary alluvium flanked by landslide, caldera-fill debris flow, sinter, colluvium, caldera-fill lacustrine, and fluvial deposits. The Redondo Creek member (Qrc) is also present.

2.2.2. Sulphur Springs

SS is an acidic-sulfate hot spring system with fumarolic activity (Goff et al., 1985). The SS site resides on Sulphur Creek near its headwaters in the Valles caldera (Figure 11). The major Sulphur Creek fault is a E-W trending Quaternary normal fault, and is most likely intersected by a nearby NE-SW trending fault to the south (Goff et al., 1985). This intersection of faults is a likely candidate for the conduit that produces the fumarolic activity and bubbling hot springs. The surface geology at SS consists of Quaternary rhyolites and caldera-fill deposits (Goff et al., 1985). The Redondo Creek and

Deer Canyon Members are present to the northeast of the site. Landslide deposits surround SS to the south and east. Early caldera-fill debris flow, landslide, alluvium, and colluvium deposits are to the southwest.

2.2.3. Soda Dam

SD lies above the hydrothermal outflow plume that is produced by the Valles caldera geothermal system (Goff and Gardner, 1994). It is also the location of the Jemez fault network. The Jemez fault network consist of NE-SW trending normal faults that extend approximately 30 km away from the Valles caldera to where it truncates along the Nacimiento fault to the southwest. The Jemez fault system has been proposed to transport fluids from the Valles caldera geothermal system to the Nacimiento fault (Renick et al., 1931; Cron, 2011; McGibbon, 2015).

SD is a large fissure-ridge style travertine, with minor travertine mounds around it, that transects the Jemez river (Figure 4). Two NE-SW-trending Quaternary faults associated with the Jemez fault network (Soda Dam fault to the south and Jemez fault to the north) pass through this location where numerous carbonic springs are located within the river and along the roadside (Figure 12). The Soda Dam fault offsets Proterozoic granite gneiss and Paleozoic limestone. The Paleozoic limestone and Pennsylvanian age Madera Limestone Formation are offset by the Jemez fault. Quaternary alluvium covers the eastern portion of this site where these faults are buried.

2.2.4. Penasco Springs

PS is the location of numerous carbonic springs depositing travertine along and near the Nacimento fault (Figure 5 and 13). The Albuquerque basin is currently bound by the Nacimiento Fault to the northwest, which is interpreted to be a major western bounding fault system of the Albuquerque basin, including the Sand Hill, Santa Fe, Puerco, and Comanche faults (see below). The Nacimiento fault is a Laramide thrust fault that has been reactivated as a normal fault during continental extension of the RGR. PS resides on the border of the Albuquerque basin and San Juan basin, but it's location along the Nacimiento fault make it a good field site for studying CO_2 flux traveling along this major reactivated Quaternary fault.

Travertine deposits of Quaternary age are dispersed throughout the site where the majority of them are located to the northeast. At this location, the Nacimento fault offsets the Triassic Petrified Forest Member against the Permian Yeso Formation, where Quaternary age terrace deposits lie on top of these stratigraphic units.

2.2.5. San Ysidro

SY resides on the Nacimento fault and Tierra Amarilla anticline ~6.25 km south of PS (Figure 14), along the northwest border of the Albuquerque basin. The Nacimiento fault makes up the core of the 1.6-km-long, N-S trending, Laramide age Tierra Amarilla anticline (Woodward, 1972). These two features combined help to channel fluids along the dip slope of the Tierra Amarilla anticline towards the Nacimiento fault, promoting springs and travertine deposits (Cron, 2011; McGibbon, 2015). The Tierra Amarilla anticline has a southern plunge. The fissure-ridge style travertine at SY is the site where large amounts of spring and surface CO_2 is degassing (Figure 5).

SY and PS have been well studied in terms of their water and gas chemistry (Karlstrom et al., 2013; Crossey, 2016; Cron, 2011; McGibbon, 2015; Blomgren, 2016). Generally, sources for CO_2 around active carbonic springs depositing travertine, and around volcanic systems, mainly include endogenic and organic carbon, known as external carbon (C_{ext}), with some carbon derived from the dissolution of carbonate (C_{carb}; Crossey et al., 2009; Chiodini et al., 1999). Endogenic CO_2 is attributed to a magmatic source, where the nearest magma is the cooling magma chamber of the Valles caldera. McGibbon (2015) measured carbon isotopes that attest to an endogenic source at SY and PS. $^3He/^4He$ ratios (0.1 to 1.0) at SY and PS (Figure 2) also confirm a magmatic signature that may be attributed to the Valles caldera and/or mantle-crust boundary ($^3He/^4He$ table in Appendix C). Since, the Nacimiento fault is a major rift bounding fault, it has the potential to be a connecting structure between the mantle and crust.

2.2.6. Zia Pueblo

The ZP site consists of the Pico Butte and Santa Ana fault network, where many of the Quaternary normal faults have been cemented with calcite, and to a lesser extent silica (Figure 5 and 16). The Santa Ana fault network is located around the north-central Albuquerque basin border. The faults have been highly cemented with mainly carbonate (sparry calcite), and to a lesser extent, silica cement towards the north around the Jemez Mountains (Figure 6 - Minor and Hudson, 2006; Caine and Minor, 2009). These cements attest to past southward and upward fluid migration from the Valles caldera and Jemez Mountains to the north. The majority of the surface is composed of Santa Fe Group syn-rift deposits that are overlain by Quaternary volcanics (mainly basalt) to the east.

2.2.7. Sand Hill Fault

The SHF is located on the western border of the Albuquerque basin and is a major RGR bounding fault. It is a steeply dipping down-to-the-east normal fault that is cemented with calcium carbonate, and separates synrift sedimentary rocks of the lower Santa Fe Group from the upper Santa Fe Group (Mozley and Goodwin, 1995). The length of this fault from end-to-end is 35.6 km with a dip of 63-82 °E (Machette et al., 2000 - Figure 5 and 17).

2.2.8. Carrizo Arroyo

The Carrizo Arroyo site hosts the Comanche and Santa Fe faults (Figure 5 and 17) with travertine deposits located to the far west of the site. The Santa Fe fault is a major western bounding normal fault of the RGR and Albuquerque basin (Machette et al, 2000). It offsets Pliocene to early Pleistocene Sierra Lardons Formation (upper Santa Fe Group) against older rocks of the Triassic Chinle Formation. Displacement along this fault is down-to-the-east with a dip of 55-60°E. The length of this fault from end-to-end is 29.6 km (Ricketts and Karlstrom, 2014; Machette et al., 2000). The Comanche fault is a high-angle reverse fault that dips to the west. It offsets Pennsylvanian sedimentary rocks (Red Tanks Formation) on the western side from Permian sedimentary rocks (Yeso Formation) on the eastern side (Ricketts and Karlstrom, 2014). The Laramide-age Comanche fault has been reactivated as a normal fault during the extension of the RGR (Ricketts and Karlstrom, 2014).

3. Classifying CO_2 Flux Ranges

CO_2 degassing on the surface from Earth's interior is generally derived from three sources: 1) soil (organics and inorganics), 2) dissolved carbonate, and 3) magmatic or mantle (Crossey et a., 2009). Attributing specific CO_2 flux ranges to these sources is difficult without geochemical data collected at the same time of CO_2 flux measurement. However, geochemical results from previous authors (Crossey et al., 2016; Karlstrom 2013; Newell et al., 2005; Cron, 2011; McGibbon, 2015; Blomgren, 2016) suggest there is a combination of all three sources at most of the study sites. These geochemical results will be discussed later on in this paper.

CO_2 flux data is described in terms of CO_2 flux ranges encountered at each site (i.e. local background, diffuse, and HPSF). Further attempts are made to give some general constraints on the types of sources that can produce the ranges of CO_2 flux measured at each site. An illustration is used to help comprehend the three populations (i.e. groups) of CO_2 flux encountered at most of the study sites (Figure 7). For this study, local background CO_2 flux is produced by the soil profile with little or no inputs of CO_2 from the fault zone. Here, the term diffuse CO_2 flux is referred to as above background values that generally produce moderate fluxes. The mechanisms for producing a diffuse flux may be a combination of background and HPSF, where CO_2 gas has migrated through the rocks and soil along fractures away from the fault zone, rather than in the fault damage zone, but still constitutes a local relationship with the fault. Elevation changes in groundwater that is enriched with dissolved CO_2 may also be a mechanism that produces a diffuse CO_2 flux (Chiodini et al., 2004).

HPSF are localized around springs emitted directly over the fault zone, and may also be produced at the intersection of faults (Hancock et al., 1998). It is proposed these fluxes have a component of deeply sourced fluids (i.e. endogenic) that ascend through the crust containing other mantle gases (e.g. helium -Crossey et al., 2016; Karlstrom 2013; and Newell et al., 2005). Furthermore, these HPSF are most likely a mixture of local background flux, diffuse flux, meteoric groundwater, dissolution of carbonate, and endogenic fluids that have migrated along the flow path in the fault damage zone (McGibbon, 2015).

3.1. Local Background CO_2

It is important to understand what processes control the generation of a CO_2 flux, no matter how small this value may be, because these processes may be a determining factor for when to perform a CO_2 flux survey and what local considerations need to be taken into account (e.g. temperate, arid, or boreal environments). CO_2 that makes up background fluxes are generally the result of biological and inorganic CO_2 production from the soil profile (Chiodini et al., 2008). This has been well documented by biologists and follows chemical responses due to precipitation, microbial and plant activity (Sponseller 2007; Emmerich, 2003; Huxman et al., 2004). Inorganic CO_2 is generally derived from chemical weathering controlled by the carbonate reaction series (Emmerich, 2003):

$$CO_2 + H_2O \leftrightarrow HCO_3^- + H^+ \qquad (1)$$

$$CaCO_3 + H^+ \leftrightarrow Ca^{2+} + HCO_3^- \qquad (2)$$

When acidic precipitation infiltrates through the soil, equation (2) is driven to the right and equation (1) to the left (Emmerich, 2003). During periods of precipitation where the surface becomes sufficiently wet, this reaction reaches its maximum CO_2 flux within a 24-hour period, where it then significantly decreases. Precipitation filling up pore spaces can also lead to an increase in the CO_2 flux (Emmerich, 2003). Furthermore, due to the increased global atmospheric CO_2 concentration over the past 57 years (Dlugokencky and Tans, 2016), the potential effects of carbonic acid on the soil profile must be taken into consideration when performing geologically motivated CO_2 flux surveys. Therefore, it is important that CO_2 flux surveys be conducted during dry periods to decrease the potential effects of soil activity.

4. Methods

The methods used for gathering, grouping, and interpreting the CO_2 gas flux data combine cumulative probability plots (Sinclair, 1974), geospatial analyses from geologic maps of fault networks, analytical analyses, and water and gas geochemistry of spring vents to show whether faults are known conduits for deeply sourced CO_2. Geological and geospatial analyses of study sites show mapped fault networks (Figures 1 and 10-17), nature of fault cementation (Figure 6 - Minor and Hudson, 2006; Plummer et al., 2012), and nature of any travertine deposits. All geospatial and most of the geological analyses performed during this study used Geographic Information Systems (GIS) ArcMap to plot the geology, including major and minor Quaternary faults, from various geologic maps downloaded from the New Mexico Bureau of Geology and Mineral Resource and USGS Earthquake Hazard Program websites. GIS was used to plot all CO_2 flux measurements, depict appropriate flux group values, and calculate areas for total CO_2 flux degassing at each site.

4.1 CO_2 Flux - Field and Technical Procedures

The instrument used to measure CO_2 flux (g_{CO2}/m^2d) was an EGM-4 CO_2 gas analyzer (PP-Systems) with a cylindrical accumulation chamber (Chiodini et al., 1998). This is a noninvasive technique that measures CO_2 degassing on the surface by pressing the bottom of the accumulation chamber firmly into the soil (~1-3cm). For measurements recorded at springs, a pvc cylindrical attachment was used (volume ~ 8.29×10^{-4} m^3) to couple the instrument to the water surface while ensuring enough spacing between the water and the fan within the accumulation chamber. The CO_2 is collected in the accumulation chamber, where it is then transported by a fan to the infrared gas analyzer. From there it is sent back through the accumulation chamber to insure a properly sealed system. The gas analyzer uses a non-dispersive infrared microprocessor control and linearization technique, where the measurements are automatically corrected for temperature and pressure (i.e. elevation – Figure 8).

The accumulation chamber has a volume of 1.18 x 10^{-3} m^3. The infrared gas analyzer has a measurement range of 0-100,000 ppm with an accuracy of <1% error. The maximum output flux measured by this instrument is approximately 100 g_{CO2}/m^2hr (or 2,400 g_{CO2}/m^2d), with a minimum flux of 0.01 g_{CO2}/m^2hr (or 0.24 g_{CO2}/m^2d) in the presence of a positive flux. However, by logging the concentrations at 5 second intervals a flux may be calculated by hand that exceeds the 2,400 g_{CO2}/m^2d maximum flux produced by the instrument utilizing a similar formula the instrument uses:

$$R = \frac{\frac{d_{CO2}}{dt}}{V/_{h}} \tag{1}$$

Where *R* is the flux (g/m^2sec), d_{CO2} is the change in CO_2 (g), *dt* is the change in time (sec.), *V* is the volume of the chamber (1.178x10^{-3} m^3), and *h* is the height of the chamber (0.15 m). The CO_2 for the d_{CO2} component was simply converted from ppm (µmol/mol) to grams:

$$CO_{2(\mu mol)} = b \times CO_{2(\frac{\mu mol}{mol})} \tag{2}$$

$$CO_{2(grams)} = \frac{CO_{2(\mu mol)}}{1000000_{(\frac{\mu mol}{mol})}} \times M \tag{3}$$

Where *b* is the bulk gas (moles) and *M* is the molar mass of CO_2 (44.01 g/mol). The concentration of CO_2 is corrected for by subtracting out atmospheric CO_2 concentrations obtained at each site using the instrument.

Air within the system was filtered through soda lime, removing all the CO_2, between each measurement, and the chamber was flushed prior to each recording. For each recording, the changes in the concentration of CO_2 over a period of 120 seconds was measured, unless the maximum flux or concentration was reached before the 120 second mark. The device uses an internal 12 V; 2.0 Ah lead acid rechargeable battery.

Spacing between each measurement varied at each site depending on the size of the area and flux conditions. At sites with moderate-high flux, spacing was maintained between approximately 5-25 m. In areas where low flux persisted, spacing was approximately 30 m and was narrowed down to 5-10 m approaching a fault (e.g. ZP, SHF, and CA). Transects were utilized to depict the relationships between fault zone width and CO_2 flux, and also hypothesized was buried faults could be detected. CO_2 flux measurements were recorded during dry periods to decrease any CO_2 gas produced by biological or geochemical reactions initiated by precipitation. Measurements and samples were taken during the summer of 2015 and winter of 2015-2016.

4.2. Analytical Approach – Cumulative Probability Plots

Cumulative probability plots are used to assess the modal distribution of one-dimensional data in log space (Sinclair, 1974). By partitioning the data this way, one is able to readily see log-normal groups overlapping from complex statistical data distributions, which are then segregated into individual groups (Chiodini et al., 2008). This technique is more useful than plotting the data on histograms, which requires an arbitrarily chosen bin range for the log CO_2 flux, and then another arbitrarily chosen point where overlaps between log-normal distributions and groups occur. By using cumulative probability plots one can quickly plot the data and empirically determine bin ranges via inflection points while keeping a consistent scale between all plots produced at each location. Further details about this approach are in Chiodini et al. 1998 and 2008; Werner et al., 2008; Lee et al., 2016; Bergfeld, Goff, and Janik, 2001; Cardellini, Chiodini, and Fondini, 2003; etc.

Negative values were removed from the analysis, because these measurements are obtained when the system is not sealed properly and/or wind penetrates into the chamber, diluting the concentration and generating negative flux. Measurements collected in the open air were also excluded from these analyses.

Cumulative probability plots, used by Chiodini et al., 1998 for use at geothermal sites in Italy, are convenient for determining threshold (i.e. groups) values for local CO_2 background flux, diffuse flux, and HPSF. This method is depicted and explained in Figure 9, where the SY cumulative probability plot is used as an example. In general, if the data plots as a straight line on cumulative probability paper it has a unimodal distribution, which represents a single, non-anomalous, source (i.e. log-normal distribution - Sinclair, 1973; Chiodini, et al., 2008). Polymodal distributions, indicated by infection points, or maximum curvature of the data, indicate the presence of multiple groups of data (i.e. data clusters or multi-log-normal distributions). The choice for the exact locations of the inflection points that segregate out the data into groups is somewhat arbitrary in the sense that groups will generally overlap with one another. However, this approach at best gives an approximation for thresholds, and at worst may result in a high proportion of anomalous values going unrecognized (Sinclair, 1974).

Once the inflection points along all the data are determined the data can be segregated into CO_2 flux bins (e.g. Figure 9 shows 3 data bins). The data in the bins are then redistributed/plotted onto the cumulative probability plot based on inflection point "cut-offs." A trend line is drawn through the redistributed data, and then group threshold values are determined. Threshold values are determined from overlaps between 1% and 99% of the data where the trend lines cross, or when there is no overlap, from where the trend line of the group crosses 1%. In the event an overlap exists, the 99% of the lower population and the 1% of the upper population on the trend lines were chosen. This provides a range of CO_2 flux values that are interpreted to fall into the category of background, diffuse, and/or HPSF.

This method is useful for determining the impact of CO_2 flux in an area. However, it only gives a quantitative estimate of the total CO_2 released along faults, and little about its source. In order to obtain a more detailed analysis of the sources of CO_2, the biology, soil, and geologic settings combined with geochemistry need to be evaluated in order to provide more confidence to the terms local background, diffuse, and HPSF fluxes.

4.3. Gas and Water Compositions

A T-shaped connecter was used to collect 16 gas samples from AC, SD, and SY in pre-evacuated Labco 12 ml Borosilicate Vials during flux measurements (Lee et al., 2016; Chiodini et al., 2008). Whole gas analyses were performed to construct ternary diagrams of N_2, He, and Ar (Giggenbach, 1992 and 1995) in hopes that mixing lines could provide constraints on a magmatic source. The whole gas analyses were also performed to see if methane (CH_4), a primary resource for natural gas production in the San Juan basin, was present in the Albuquerque basin. The gas samples for AC were collected in the summer of 2015. SD and SY were collected during the winter of 2016. Whole gas analyses were run on all of these samples during the winter of 2016. Whole gas analysis followed Lee et al., 2016. Gas compositions were measured at the University of New Mexico (UNM) in the Volcanic and Geothermal Fluid Analysis Laboratory (GFAL). The GFAL has a combined Gow-Mac series G-M 816 Gas Chromatograph (GC) and Pfeiffer Quadrupole Mass Spectrometer (QMS – range of 0 to 120 AMU), that permits the measurement of CO_2 concentrations and relative abundances (volume %) of gas species (CH_4, H_2, Ar, O_2, N_2, CO, CO_2, and He).

To assist with interpretations for the sources of the CO_2 flux groups (i.e. background, diffuse, and HPSF), gas and water geochemistry provided further insight into the sources of CO_2 carried by groundwater. Water and gas geochemistry performed by McGibbon (2015); Blomgren (2016); Goff and Janik (2002); Cron (2011); Crossey et al., (2016); Karlstrom et al. (2013); Newell et al. (2005); Zhou et al. (2005); Williams et al. (2013); Phinney et al. (1987); and Truesdell and Janik (1986) at or near the study sites was relied upon.

Carbon in the CO_2 gas can come from the dissolution of carbonates (C_{carb}), biologically derived sedimentary carbon (C_{org}), and deeply derived sources (C_{endo} – Chiodini et al., 1999; Crossey et al., 2009). The percentages of each of these carbon components in the CO_2 gas varies between sites. In order to depict deeply derived carbon, the carbon is broken up into C_{org} and C_{endo} components that make up the external carbon (C_{ext}). This C_{ext} is then plotted on a graph that has $\delta^{13}C_{ext}$ (%) against total C_{ext} (mol/L), where generally higher $\delta^{13}C_{ext}$ (%) depicts higher concentrations of the heavier stable isotope of carbon (^{13}C) that comes from endogenic sources (mantle values around -5%; Sharp, 2007).

The large percentages of CH_4 from gas samples extracted directly from wells within the northwestern San Juan basin attest to hydrocarbon bearing rocks (Zhou et al., 2005). Black (1992;2002;2013) discusses the potential for large hydrocarbon reservoirs located in the Albuquerque basin sourced from the same rocks as the San Juan basin. With the SY site located along the border of these two regions, and the ZP along the northern border of the Albuquerque basin, whole gas analyses were conducted on samples collected from the surface and springs to measure for methane (CH_4). Results of the gas analyses are discussed below for each site

4.4. Calculating Total Annual Flux

The total annual CO_2 flux (tons/year – t/y) at each site was calculated in 4 steps and follows a similar method outlined in Lee et al. (2016). See Figure 14 as an example for this process. 1) After generating groupings based on cumulative probability plots the CO_2 flux and elevation were plotted along a line that crossed faults. In most cases the CO_2 flux measurements did not track on this line, so instead the values were projected onto the line to help constrain fault zone widths. It should be noted that in the event CO_2 flux measurements were taken away from the main CO_2 producing fault, or if there was another fault zone at the same site, two separate calculations were made for the total annual CO_2 flux (e.g. Figures 10, 13, and 17). 2) The faults were placed on the cross sections and the data were broken up into fault damage zone (red dashed lines) and distal damage zones (blue dashed lines) based on HPSF and diffuse fluxes, respectively. 3) The widths of the damage zone and distal damage zone were then projected onto the map containing fault locations. 4) the area of these zones was then obtained and multiplied by the average flux within each zone to obtain the total CO_2 flux (in t/y).

5. CO_2 Flux Results, Gas Analysis, and Interpretations

Analytical results for CO_2 degassing at the different sites in the Albuquerque basin and Valles caldera are shown in Table 1. Negative values and air measurements are excluded from these tables. Table 1 is broken up into surface, spring, and surface and spring flux measurements for convenience of distinguishing between what type of media the measurements were collected on. Breaking up the data this way allows the reader to see that the majority of the HPSFs come from springs (i.e. spring flux), but there are also significant fluxes attributed to HPSF that come from dry ground measurements (i.e. surface flux). Table 2 gives the groups (background, above background diffuse, and HPSF) for each site.

Damage zones (highlighted by red on figures 10-17) for each site are constrained by HPSF and relatively high diffuse fluxes. Distal damage zone fluxes are primarily constrained by diffuse fluxes (highlighted by blue on figures 10-17), with minor components of background fluxes mixed in. Distal damage zones are likely the result of degassing of CO_2 along the fault zone at depth, which then travels towards the surface away from the primary fault damage zone (see Figure 7 for a schematic of this process). HPSF and relatively high diffuse fluxes are measured directly over the damage zone on the surface. Appendix B gives the results of the CO_2 flux measurements at all the sites including location (latitude and longitude), date, and time.

5.1. Alamo Canyon

There were 60 CO_2 flux measurements collected at AC (Table 1). Figure 10 shows a suite of illustrations and analyses used to group the different CO_2 flux ranges (cumulative probability plot), display geospatial results, and calculate the annual CO_2 flux at AC. Measurements taken in the air have an average concentration of 445 ppm (umol/mol). Table 1 shows that AC has the highest average CO_2 flux (11,286 g_{CO2}/m^2d) of all sites combining both surface and spring measurements. The average spring and surface fluxes are 61,349 g_{CO2}/m^2d and 47 g_{CO2}/m^2d, respectively. Groups of CO_2 fluxes consist of background (0.7 - 4.0 g_{CO2}/m^2d), diffuse (15.5 – 1,778 g_{CO2}/m^2d), and HPSF (1,778 – 144,239 g_{CO2}/m^2d), with overlaps (i.e. combinations) of background and diffuse (4.0 – 15.5 g_{CO2}/m^2d - Table 2 and Figure 10). Local background CO_2 is elevated slightly at this location, due to the combination of the Valles geothermal system and the marsh like conditions of the valley that promotes biological activity in the soil profile.

The two main faults that pass through the valley center are interpreted to be the major contributors to CO_2 degassing, with minor contributions made from faults trending N-S, and another inferred fault to the southeast. Fault zone widths (i.e. damage zones) are represented by CO_2 flux for the two major E-W trending faults and one N-S trending fault to the southeast. Figure 10 shows the damage zones (red polygons) where HPSF and above average diffuse fluxes were measured. Fault motions for all the faults in this area are unknown, so fault geometry here will use terms of their geographical relation. There is an increase in width of the northern fault damage zone from east to west of 24 m to

135m, respectively. The northern fault has a wider damage zone on its northern wall compared to its southern wall. The damage zone on the southern fault (68 m) is also wider on its northern wall and maintains its width as seen by the HPSF measured along it. The southeast fault was determined to have a damage zone on its northwest side of 66 m, and no measurements were collected on its southeast side, due to the presence of dense vegetation combined with marsh like conditions. The total amount of CO_2 degassing at AC, based on the areas (blue + red polygons = 226,526 m^2) of these damage zones and distal damage zones is $7.8x10^5$ t/y.

Whole gas analyses from AC show air-like components (Figure 18), however, these results are inconclusive due to errors in the sampling and analytical methods. These samples were collected during the summer of 2015, and they were analyzed during the winter of 2016 (over 8 months). The low He concentration could be either due to gases mixing with air during collection or the dissipation of He through the glass vials prior to analyzing them (Fischer et al., 1998).

5.2. Sulphur Springs

There are very high background flux measurements at SS due its geothermally enhance location. CO_2 flux measurements were collected on two different dates. During the second measuring trip, CO_2 flux was measured at springs (Tony’s, Men’s Bathhouse, and Footbath Spring) and these replaced previous spring measurements at the same location. The rest were collected from the first survey, where only a maximum flux value of 2,400 g/m^2d could be obtained. There were 55 measurements taken at SS (Table 1). The average air concentration measured here with the CO_2 flux device is 711 ppm. SS is host to the highest average surface flux of all sites at 754 g_{CO2}/m^2d (n = 50). The overall average flux, including spring and surface measurements is 5,937 g_{CO2}/m^2d, with an average spring flux of 5,759 g_{CO2}/m^2d.

There are two groups of CO_2 flux at SS (Table 2). Diffuse fluxes range from 8.6 – 60.3 g_{CO2}/m^2d, and HPSF fluxes range from 302 – 170,112 g_{CO2}/m^2d. Combinations of each group were also calculated (60.3 – 302 g_{CO2}/m^2d) from the cumulative probability plot (seen on Figure 11). Fault damage zone width along Sulphur Creek Fault is 72 m on the footwall (northern side) and 117 m on the hanging wall (southern side). The fault has a distal damage zone component that was measured out beyond the damage zones. Combining the average CO_2 flux of each zone, and multiplying this by the area (total area = 88,000 m^2) gives a total annual CO_2 flux at SS of $1.3x10^5$ t/y. The source of this CO_2 is highly indicative of a magmatic system due to the $^3He/^4He$ (R_C/R_A) ratios, which are shown on Figure 2. Gas samples collected at Footbath Spring, Men’s Bathhouse, and Women’s Bathhouse springs by Goff and Janik (2002) have $^3He/^4He$ (R_C/R_A) that range from 5.16 – 6.16 (see Appendix C for $^3He/^4He$ results from various authors).

5.3. Soda Dam

SD is host to two major NE-SW trending normal faults (Soda Dam and Jemez Faults) and massive travertine deposits with active carbonic springs that were targets for this survey (Figure 12). There were 90 CO_2 flux measurements taken at SD (Table 1). CO_2 flux was measured at 4 main carbonic springs where continuous CO_2 rich bubbles are present. The average air concentration here measured by the CO_2 flux device is 425 ppm (much lower than SS). The average CO_2 flux at SD is 252 g_{CO2}/m^2d (n = 90). The average surface flux is 97 g_{CO2}/m^2d (n = 85) and the average spring flux is 2,887 g_{CO2}/m^2d (n = 5).

Three different groups were calculated at SD (Figure 12). Background CO_2 flux ranges from 0.2-2.8 g_{CO2}/m^2d, diffuse flux ranges from 2.8-32.4, and the HPSF flux ranges from 200-9,675 g_{CO2}/m^2d. There is a combination of diffuse and HPSF flux that ranges from 32.4 – 200 g_{CO2}/m^2d, based on the cumulative probability plots. A HPSF flux and elevated diffuse fluxes were measured to the north of the two mapped faults indicating the presence of a potential third fault that was previously unknown. Furthermore, there is another potential fault that trends NW-SE that transects the SD fault, potentially enhancing the damage zone and therefore permeability of this area.

Fault damage zones are wider on the footwall side of the two main faults, and also on the southern side of the previously unmapped fault to the north, which is proposed to be its footwall. The SD fault has a damage zone width of 83 m on its footwall and 13 meters on its hanging wall. The Jemez fault has a damage zone width of 12 m on its footwall and no damage zone (or increased permeability) on its hangingwall. The unmapped fault has a damage zone width of 12 m on its footwall, which is the same as the Jemez fault, and no measurements were recorded to the north of the fault. Distal damage zone fluxes were measured in between the faults, that represent zones of above background fluxes that are partly produced by the location of the faults.

The total amount of CO_2 degassing at SD is approximately 1,856 t/y over a combined area (damage zone + distal damage zone) of 2,300 m^2. The source of this CO_2, as indicated by a $\delta^{13}C_{ext}$ of -0.731% (McGibbon, 2015), shows an endogenic component that may be related to the Valles caldera outflow plume. There are also components of C_{org} (organic carbon) and C_{carb} (dissolved carbonate) that may be associated with the La Madera limestone that outcrops along the west side of the site (McGibbon, 2015). Whole gas analysis from SD show air like components (Figure 18) making these results inconclusive due to errors in the sampling and analytical methods. These samples were collected and analyzed within 4 weeks, and air most likely mixed with other gases before sampling causing the air like values seen on Figure 18. Goff and Janik. (2002) collected gas samples from the same locations and their results plot on the deeply sourced fluid mixing line (Figure 18), indicating a deeply derived fluid that is partly derived from the Valles caldera magmatic system (Goff and Janik, 2002). $^{3}He/^{4}He$ ratios of 0.81 RA, from Goff and Janik (2002), show some magmatic input.

5.4. Penasco Springs

40 measurements were collected along transects that cross two travertine mounds, one on the Nacimiento fault and one to the southwest of the Nacimiento fault (Figure 13). one air measurement produced a concentration of 434 ppm. The average CO_2 flux at PS is 251 g_{CO2}/m^2d (n=40), with an average spring flux of 1,980 g_{CO2}/m^2d (n=5) and an average surface flux of 4.1 g_{CO2}/m^2d (n=35 - Table 1). Three groups were calculated with CO_2 flux ranges of 0.0-2.5 g_{CO2}/m^2d, 4.0-13.2 g_{CO2}/m^2d, and 13.2 – 2,400 g_{CO2}/m^2d for background, diffuse, and HPSF, respectively. A combination of background and diffuse flux was also calculated (2.5 – 4.0 g_{CO2}/m^2d). The spring to the west of the Nacimiento fault (ca. 850m) has a high CO_2 flux which is interpreted to be a possible unmapped N-S trending fault (Figure 13).

The Nacimiento fault at this study area has a damage zone width of 20 m hosted on the hangingwall (Figure 13). There were no HPSF measured on the footwall side of the fault, but there were distal damage zone components on the footwall and hangingwall. The total CO_2 degassing along the Nacimiento fault at this location was calculated to be approximately 480 t/y. The inferred N-S trending fault that passes through the survey to the southwest was drawn from the location of other travertine mounds that align to the north of this location. There is also displacement of Mesozoic rocks to the northeast where another NE-SW inferred fault has been drawn that transects the N-S inferred fault. These inferred faults could help explain the location of the active carbonic spring that the measurements were taken over. At this location a total annual CO_2 flux of 3,588 t/y was calculated, which gives a total annual CO_2 flux of 4,068 t/y (total area of damage zones + distal damage zones = 112,647 m^2) at PS from measured locations.

The source of this CO_2 has been proposed to be a combination of fluids traveling along the Nacimiento fault from the San Juan basin, and mixing with fluids that have travelled from the Valles caldera geothermal system along the Jemez Fault network (McGibbon, 2015). The $^3He/^4He$ ratios from gases collected at PS are greater than 0.1 RA (Figure 2) indicating a mantle signature (Crossey et al., 2016), and carbon $\delta^{13}C_{ext}$ range from -1.78 to 2.251 (n = 13) indicating a mixture of C_{endo}, C_{carb}, and C_{org} (McGibbon, 2015)

5.5. San Ysidro

San Ysidro has the highest calculated CO_2 flux of all the sites (149,323 g_{CO2}/m^2d), measured on the Twin Mounds west travertine spring. The average air concentration measured at SY is 427 ppm. The average CO_2 flux measured at SY is 1,169 g_{CO2}/m^2d (n=256), with an average surface flux of 14 g_{CO2}/m^2d (n=238), and an average spring flux of 16,442 (n=18 - Table 1). The highest flux may not hold true when compared to sites at the Valles caldera geothermal system, because, at AC, SS, and SD the instrument maxed out (100,000 ppm) after the first measurement was taken, so no flux could be calculated by hand.

There are three CO_2 flux groups calculated at SY. These range from 0.0-1.3 g_{CO2}/m^2d for background, 1.3-5.1 g_{CO2}/m^2d for diffuse, and 42.7-149,322 g_{CO2}/m^2d for HPSF (Table 2 and Figure 14). There was overlap between diffuse and HPSF groups (5.1 – 42.7 g_{CO2}/m^2d). The major structure contributing to the high CO_2 flux at SY is the Nacimiento fault. The Tierra Amarilla anticline may also help channel fluids along-dip of the stratigraphy towards the surface.

The Nacimiento fault damage zone increases somewhere between PS and SY as shown on Figures 13 and 14. At SY, the Nacimento has a footwall (west side) damage zone width of approximately 98 m and a hangingwall (west side) damage zone width of approximately 72 m, for a total damage zone width of 169 m on the Nacimiento fault at this location. The faults damage zone was carried across the entire survey, due to the HPSF and relatively high diffuse fluxes measured on the surface in between HPSF measurements at springs. SY is degassing approximately $5.3x10^5$ t/y of CO_2 (over an area of 2,841,199 m^2), which is comparable to sites at the Valles caldera geothermal system. It should be noted that the area of SY, compared to Valles caldera sites, is much larger, which partly explains why the total CO_2 released at this site is comparable. However, the large fissure-ridge style travertine deposit and multiple active carbonic springs that extend the majority of this site attests to large amounts of CO_2 degassing in the geologic past and present.

$^3He/^4He$ ratios from gases collected at SY are greater than 0.1 R_A (Figure 2 and Appendix C) indicating a mantle signature this far southwest of the Valles caldera

(Crossey et al., 2016). $\delta^{13}C_{ext}$ ranges from -1.78 to 2.251 (n = 13) indicating a mixture of C_{endo}, C_{carb}, and C_{org} (McGibbon, 2015). There was no CH_4 (appendix B) measured at any of the springs, possibly indicating a lack of hydrocarbon production at depth below this site or to the north along the Nacimiento fault. 7 gas samples were collected from springs and the dry surface, and their relative He, N, and Ar percentages were plotted on the ternary diagram on Figure 18. Most of these values plotted as air due to air mixing with other gases prior to sampling. One sample collected from a small bubbling spring to the southeast of the Twin Mounds area plotted near the deeply derived mixing line, indicating significant amounts of He are degassing along the Nacimiento fault at SY. Newell et al (2005) also collected gas samples at the same springs, which are shown on the same ternary diagram on Figure 18. These results suggest a relatively high concentration of He that plots on the deeply derived mixing line.

5.6. Zia Pueblo

CO_2 flux transects were performed across four different cemented faults of the Santa Ana Fault Network (3 carbonate and 1 silica to the northeast – Figure 15). 38 CO_2 flux measurements were taken at ZP, and one air measurement that has a concentration of 434 ppm. The average surface CO_2 flux is 0.7 g_{CO2}/m^2d (n=38 - Table 1). One high anomalous flux (9.6 g_{CO2}/m^2d), which is attributed to a diffuse flux, was measured along the Silica cemented fault. There are two assigned groups ranging from 0.0-1.7 g_{CO2}/m^2d (n=37) for background and from 1.7-9.6 g_{CO2}/m^2d (n = 1) for diffuse. The CO_2 fluxes measured at ZP are considered to represent typical background values around faults in the Albuquerque basin.

There was no total annual flux calculated for this site due to the abundance of background measurements. The goal at this site was to investigate if any CO_2 degassing along these cemented structures could be linked to geologic processes at depth, or if they were barriers to fluid flow. Compared to sites like SHF and SY, and due to the abundance of background fluxes, these faults are proposed to be barriers to upward, and possibly cross-ward, fluid flow. Furthermore, there was no CH_4 measured from a sample collected on the silica cemented fault, where the diffuse flux measurement was taken. This could be due to the cement blocking any upward hydrocarbon migration.

5.7. Sand Hill Fault

There were 40 CO_2 flux measurements taken along transects at the carbonate cemented SHF site. One air measurement taken at this location has a concentration of 423 ppm. The average surface CO_2 flux measured at this site is 3.3 g_{CO2}/m^2d (n=40 - Table 1). There are two defined groups consisting of background (0.01 – 1.12 g_{CO2}/m^2d) and diffuse (2.5 - 7.7 g_{CO2}/m^2d) fluxes, with a combination of background and diffuse (1.12 – 2.5 g_{CO2}/m^2d – Table 2 and Figure 16). When compared to the ZP site, there is an increase in CO_2 flux around this carbonate cemented fault, where the average surface flux is one order of magnitude larger than the ZP site (0.7 g_{CO2}/m^2d). Therefore, the SHF is interpreted to be a semi-conduit for fluids migrating up along its fault zone.

There are zones along the SHF that are most likely not as fractured, as seen by the low background CO_2 fluxes (Figure 16) along strike with the fault. This owes to the heterogeneity of cement that has been documented by previous authors (Heynekamp et al., 1999; Mozley and Goodwin, 1995: Minor and Hudson, 2006). Compared to the ZP site, the SHF site has a moderate CO_2 flux that is attributed to a diffuse flux. Both sites have similar vegetation and are cemented with carbonate, but the SHF is a deeper and older (Machette, 2000) fault than most faults in the Santa Ana Fault network. The SHF location as a major bounding fault also make it a candidate for deep sources to migrate up along, but is not a complete barrier to upward fluid flow. Fault damage zones were not constrained by CO_2 flux measurements across the fault at this location, but a distal fault zone was classified for the fault so that the total annual CO_2 flux could be calculated. A total CO_2 flux of 258 t/y (total area = 215,932m^2) is degassing along the SHF at this location from a combination of background and diffuse flux types.

5.8. Carrizo Arroyo

This site showed a moderate CO_2 flux, where the CO_2 appears to be channeled along two major faults (Comanche and Santa Fe faults) and two minor faults (unnamed faults) in the center of the site. There were 48 CO_2 flux measurements recorded, and one air measurement with a concentration of 427 ppm was taken at this site. The average surface CO_2 flux is 2.4 g_{CO2}/m^2d (n=48), falling in between ZP and SHF (Table 1). There are two CO_2 flux groups at CA consisting of a background flux (0.0-1.0 g_{CO2}/m^2d) and diffuse (2.5 – 11.3 g_{CO2}/m^2d) flux (Table 2 and Figure 17). There is a combination of background and diffuse (1.0 – 2.5 g_{CO2}/m^2d) that was calculated for this site. CA had a higher maximum CO_2 flux than SHF (11.3 and 7.7 g_{CO2}/m^2d, respectively). An increase from background to above background CO_2 flux (from east to west) indicates these faults impact their surroundings, and are conduits for a diffuse flux of CO_2. The highest fluxes measured at this site are located to the west, where travertine deposits are found.

Due to the lack of HPSFs, fault damage zones were not constrained across the faults at this location. A distal fault zone was classified for each of the faults so that the total annual CO_2 flux could be calculated. The total annual CO_2 flux at CA is 50.2 t/y (total area = 52,214 m^2), which is close to one order of magnitude less than SHF. However, the area size of CA is one order of magnitude less than SHF.

The combination of multiple faults, area size, travertine deposits, and proximity to the Socorro magma body may enhance the CO_2 degassing around this area. The latter could be explained by $^3He/^4He$ ratios collected from springs near CA. Williams et al. (2013) collected a gas sample with a ratio of 0.85 R_A from Eddleman Spring to the west, and Newell et al. (2005) collected a gas sample with a ratio of 0.61 R_A from Salado Arroyo Spring to the south of CA (Appendix C).

6. Discussion and Implications

The method utilized for collecting and analyzing gas samples using the hand held instrument is not the preferred method for quantitative gas analyses, and tends to give more air-like values for the same springs measured by previous authors. The air-like values from ZP might be expected since they were collected on the surface from a moderate CO_2 flux (9.6 g_{CO2}/m^2d) location where the likelihood of air penetrating through the surface and entering the vials is higher, or it could be due to the silica cemented fault blocking fluid flow. The method needs further refinement in terms of the timing of sampling to analysis in the lab. In any event, the high concentrations and fluxes of CO_2 that were measured when combined with previous authors provides evidence for links between Earth's surface and the mantle.

6.1. Fault Conduits and Barriers

Heynekamp et al., (1999) and Caine and Minor (2009) give detailed analyses of why fault zones in poorly lithified rocks, and their components (i.e. cores, mixed zones, and damaged zones), are different from well-lithified rocks in the Albuquerque basin. Faults in poorly lithified sediments have a decrease of damage zone, and an increase in cemented and clay-rich cores, which make them fundamentally different than faults in well lithified rocks (Caine and Minor, 2009). Early mechanical entrainment of low-permeability clays into the fault core likely causes a pressure gradient and flow of calcite-saturated waters in higher permeability, fault entrained siliclastic sediments, ultimately promoting their cementation of sparry calcite (Caine and Minor, 2009). Grain size distribution of the faulted sedimentary rock also controls the permeability along sections of the fault zone. This has less of an effect on the rocks around AC, SS, SD, PS and SY, since bedrock (i.e. Mesozoic, Paleozoic, and Precambrian rocks) outcrop on the surface, and at the Valles caldera where volcanics exist. There are also no documented cemented faults at any of these sites. However, in the central and western borders of the basin it poses some consideration and could be the reason for more diffuse and low fluxes measured at ZP, SHF, and CA.

Cemented faults in the Albuquerque basin are preferentially cemented compared to their host rocks (Heynekamp et al., 1999). Cementation along these structures represents past fluid flow, and preferential cementation along the hangingwall or footwall shows preferential migration along the cemented fault (Heynekamp et al., 1999). Cements are typically focused in the inner damage zone and mixed zone of either the hangingwall or footwall side of the fault, but do not always precipitate on basinward sides of faults (Minor and Hudson, 2006). Minor and Hudson (2006) concluded that based on these observations, cemented faults create heterogeneity in the basin aquifer systems, which to some extent was confirmed by Plummer et al. (2012) groundwater geochemistry. The CO_2 flux results support this conclusion, and show that these faults are still controlling the heterogeneity of the basin aquifer system, at least in the northern basin around the Santa Ana Fault network. However, around the carbonate cemented SHF site there is still a moderate CO_2 flux. This flux is produced by fault zone permeabilities controlled by fracture densities in and along this fault zone that are still acting as conduits for upward fluid migration.

An indicator for faults as conduits or barriers includes the geochemistry of the groundwater in the northern Albuquerque basin. Deep saline fluids occupy the deep rift basins with salts (e.g. SO_4) derived from Mesozoic and Paleozoic bedrock and/or deep fluids that have moved through basement granite (Plummer et al., 2012; McGibbon, 2015). Plummer et al. (2012) indicated that the presence of major faults near hydrochemical zones could affect groundwater flow. However, on the eastern side of the Albuquerque basin (near the Sandia Fault zone), where documented cemented faults are perpendicular to basin recharge, the flow of ground water appears to be unaffected by major faults (Plummer et al., 2012). There appears to be a correlation between cemented faults in Figure 6 to the hydrochemical boundaries that were constructed by Plummer et al., (2012).

The diffuse flux around the cemented SHF in the Albuquerque basin suggests CO_2 is migrating up along fractures connected to the fault network, but where there is not a significant amount of CO_2 traveling up along the center of the fault zone. This is due to the impermeable fault core documented in most carbonate cemented faults of the Albuquerque basin (Heynekamp et al., 1999; Minor and Hudson, 2006). This impermeable fault core, at SHF, could be diverting the CO_2 away from the fault center, out where there could be an increase in the permeability (due to fracture density) along the footwall and/or hangingwall compared to the fault core. Compare this to the 4 cemented faults at ZP where all recorded measurements (except one) are background. This shows that using CO_2 flux across faults may be used as a proxy for establishing cemented faults as conduits or barriers for fluid flow.

The same hydrocarbon producing rocks and reservoirs (Mancos Shale, Niobrara, Dakota Sandstone etc.) found in the San Juan basin are also present in the Albuquerque basin. There is no evidence for the migration of hydrocarbons (i.e. CH_4) along faults in the Albuquerque basin. The non-detect of CH_4 from the Albuquerque basin sites could be due to 3 reasons: 1) the vials used were not permanent and allowed leakage to occur, 2) there was no methane present, or 3) there was no methane present at SY, however, the faults from ZP were cemented enough to block the migration of CH_4 to the surface. The third option seems most likely, since there were low CO_2 fluxes (mainly background fluxes with an average of 0.7 g_{CO2}/m^2d) measured along all the faults at ZP. CH_4 (0.001-0.045 vol%) was measured at springs at AC in the Valles caldera, indicating this method is not highly susceptible to the diffusion of CH_4 through the vials over time (Appendix D).

The migration of hydrocarbons along the Nacimiento fault from the San Juan basin to the Albuquerque basin is highly unlikely. The hydrocarbon producing rocks from the Mesozoic and Paleozoic sections outcrop along the fault and to the west of it. If any hydrocarbons were present in the past they have long since vanished during uplift or were never present due to time, pressure, and temperature constraints. McGibbon (2015) found that water flowing at PS and SY springs has some contribution from San Juan basin aquifers that have migrated along the Nacimiento fault, but no indication of hydrocarbons.

6.2. Comparisons of CO_2 Flux

Figure 19 shows a comparison of the total annual CO_2 flux (in t/y) and the average flux (in g_{CO2}/m^2d) at each location. The total annual CO_2 flux measurements at SY ($5.3x10^5$ g_{CO2}/m^2d) and PS ($4.1x10^3$ g_{CO2}/m^2d) are comparable to those measured at Valles caldera sites (AC, SS, and SD). These total CO_2 flux results were taken from the area immediately surrounding the faults at each site (see Section 5). The areas, surface geology, and structure must be taken into consideration when viewing graphs of this nature. Although, SY has a higher total CO_2 flux than SS it also has a much larger area ($2.8x10^6$ m^2 and $88x10^3$ m^2, respectively). The same can be said for PS area ($1.1x10^5$ m^2). It is realistic to view these high total CO_2 fluxes as a function of area. However, the area covered by the travertine deposits, location of major faults, and multiple carbonic spring vents at SY and PS attest to large amounts of CO_2 degassing at these areas, which is what is shown on Figure 19.

Figure 19 also shows the average flux at each location to get a sense of which site produces the highest flux per meter squared. This figure shows that SS has the highest CO_2 flux (g_{CO2}/m^2d) compared to all the other sites. It may not be producing as much CO_2 as SY or AC, but on average per-meter-squared, it has the highest surface flux. This graph shows that on an average per-meter-squared basis, Valles caldera sites have the highest compared to Albuquerque basin sites. By considering the area size and geology at each site promotes a basic understanding of which sites produce more CO_2 than others, but it also shows which sites have more significant CO_2 flux.

Large amounts of CO_2 degassing as far south as SY indicates a possible connection with the Valles caldera through north-east-trending fault networks that truncate along the north-trending Nacimiento Fault. Figure 20 shows that $^3He/^4He$ ratios and CO_2 flux decrease away from the Valles caldera and then increase around CA near the Socorro magma body. The presence of travertine along these structures attests to past fluid migration and relatively large amounts of CO_2 degassing. Crossey et al. (2006) recognized that a more significant source of CO_2 is needed to form travertine from cool waters, like those seen at PS and SY. Furthermore, the amount of dissolved CO_2 needed to deposit travertine cannot come from near surface processes (i.e. dissolution of carbonates) alone, but from a more significant contribution from a magmatic source (Crossey et al., 2006; Bellentine et al., 2001; Siegel et al., 2004).

Effects of rainfall have been observed to increase the amount of biological activity, and the size and pulse of precipitation events can control biological responses to producing CO_2 (Huxman et al., 2004). However, the semi-arid environment in which the CO_2 flux measurements were conducted combined with only measuring during dry periods decreased this possibility. Figure 21 shows a comparison of CO_2 flux values from around the world that are attributed to the soil and biology (background) compared to study sites in the Albuquerque basin. There is good correlation between background fluxes (maximum flux of 2-6 g_{CO2}/m^2d) at five other locations from around the world with similar environments and ecosystems (Mongolian Desert, China; Lower Foothills, Sierra, Nevada; Sevilleta Wildlife Refuge, Chihuahuan Desert, New Mexico; Owens Valley, California; and Sonoran Desert, Arizona). This analysis provides acceptable levels for local background flux and is useful for understanding what a background flux is.

The measurements in this study were conducted at localized sites where a total flux from two areas in the Valles caldera (AC and SS) is 9.1×10^5 t/y (total area of evaluation = 3.1×10^5 m^2), and at 4 areas in the Albuquerque basin (PS, SY, SHF, and CA) is 5.4×10^5 t/y (total area of evaluation = 3.2×10^6 m^2). This is to show that the CO_2 contributions at these sites may be significant with respect to the greater RGR system. Lee et al. (2016) found that 4.0×10^6 t/y of mantle derived CO_2 is degassing in the Magadi-Natron basin of the East African Rift (area = 9.8×10^8 m^2). Werner et al. (2008) calculated the total CO_2 flux on altered ground at the Hot Spring basin along the northeast side of the Yellowstone caldera. They determined the acidic ground was releasing 1.5×10^5 t/y across an area of 1×10^6 m^2 (they did not account for fumaroles or bubbling pools). At Latera caldera sites in Italy a CO_2 degassing rate of 1.3×10^5 t/y over an area of 3.1×10^6 m^2 was calculated by Chiodini et al. (2007). The Dixie Valley geothermal field was calculated to have a CO_2 rate of 2.8×10^3 t/d across an area of 1.5×10^5 m^2 (Bergfeld et al., 2001). These results show that sites in the Valles caldera and Albuquerque basin can approach total CO_2 released values at other geothermally and tectonically active sites from around the world.

Figure 22 shows a comparison of average CO_2 flux (g_{CO2}/m^2d) values from various locations around the world. This is to show where the average CO_2 flux values measured at locations for this study compare with other estimates from around the world.

An attempt is being made here to ignore area size, by looking at the average CO_2 flux at each of these sites. Most of these sites have comparable areas, except for the Magadi basin in the East African rift. This is important, because large areas with low CO_2 flux could potentially produce higher total CO_2 degassing rates (in tons/year) than areas that are small and have large CO_2 fluxes. Breaking up the data this way is a convenient way to compare CO_2 fluxes while keeping a somewhat consistent scale. Figure 22 shows SS as the third highest average flux of all the sites considered. This not to say that SS is the third highest in the world, but to show that these fluxes are comparable to other world-class geothermal systems. SY is considered to be on the lower end of the geothermal spectrum, as its location is in a tectonic/rift system.

Table 3 also provides further support that the CO_2 flux measurements in this study can be considered world class in terms of dormant volcanoes, geothermal, and hydrothermal systems. This table also provides CO_2 fluxes from anthropogenic sources to provide context for naturally produced CO_2 fluxes.

If more sites can be measured in the Valles caldera and Albuquerque basin one could make more constraints on the total CO_2 degassing from these major physiographic areas. There are multiple travertine springs in the Albuquerque basin (e.g. Penasco Springs and Coyote Springs) and hot and acidic ground all throughout the Valles caldera that have not been measured. By evaluating a broader area over the RGR a more reliable calculation could be made for the total amount of CO_2 released to the atmosphere from this physiographic province.

6.3. Implications for CO_2 Flux over geologic time

With the RGR in extension during the last 25 million years, and major Jemez Volcanic Lineament eruptions over the last 5-6 Ma, and as recently as ~68 ka (Zimmerer et al., 2016a; 2016b), it is likely that large amounts of CO_2 have constantly been degassing along faults, also as evidence by the localized travertine deposits. To put some constraints on the amount of CO_2 released to the atmosphere from the solid Earth during this time, the age of travertine deposits from SD and SY are considered. The SD travertine has recorded a constant hydrothermal system that was in place soon after the formation of the Valles caldera, and pulses of travertine deposits have been occurring since ca. 1.0 Ma (Goff and Shevenell, 1987; Tafoya, 2012). If a constant flux is considered over this time period, a quantification of the amount of CO_2 that has degassed from this area over time can be made. Using the total present day annual CO_2 flux of 1,856 t_{CO2}/y at SD, over a 1.0 Ma period of time, gives ca. 1.86 $x10^9$ tons of CO_2 released to the atmosphere along faults around SD. Similarly, by using a total flux of $5.34x10^5$ t_{CO2}/y for present day SY, the total amount of CO_2 released to the atmosphere over a period of 270 ka (oldest travertine accumulation – Cron, 2011) is ca. $1.44x10^{11}$ tons of CO_2 due to the Nacimiento fault and Tierra Amarilla anticline. These values are consistent between SD and SY, since SY is a much larger fissure-ridge travertine mound than SD, and SY also has higher CO_2 flux values than SD (including a larger area). These calculated total values may be considered maximums, since pulses of travertine deposition have been recorded in the rock record (Goff and Shevenell, 1987; Tafoya, 2012; Cron, 2011).

Silica cement is common near the Valles caldera geothermal system, due to the higher temperatures needed for Silica to be soluble in water (Drever, 1988 - Figure 6). Carbonate cemented faults are common at greater distances from the Valles caldera and in many locations of the Albuquerque basin. At spring point sources, travertine accumulations record voluminous degassing of such waters. In some locations, fault cementation is related to past subsurface degassing due to CO_2 rich fluid flux, and travertine deposition records CO_2 flux locked up in rocks around spring vents. Priewisch (2014) quantified this component of the CO_2 flux for several travertine platforms in New Mexico, and calculated CO_2 amounts of 3.9 Gt (compared to 144 Gt degassed at SY over 270 ka, and 1.86 Gt over 1 Ma at SD) that are fixed in $CaCO_3$ (travertine) and degassed into the atmosphere during this precipitation reaction from a volume of 1.6 km^3 of travertine. Further geophysical and geochronological analyses of the travertine at SY could be used to help constrain the volume of travertine and ages of it to determine if the calculated 144 Gt of CO_2 over this time is satisfactory.

7. Conclusions

The location of the Valles caldera and Albuquerque basin along the RGR and Jemez Volcanic Lineament produces an opportunity for large amounts of CO_2 to be released from the solid Earth. This study utilized CO_2 flux transects along different fault networks from the Valles caldera (3 sites) and Albuquerque basin (5 sites) to calculate the total amount of CO_2 released to the atmosphere at these sites, depict fault damage zones, and show that faults are either conduits and/or barriers to fluid flow. The annual CO_2 released from Valles caldera and Albuquerque basin sites are: $7.8x10^5$ t/y at AC; $1.3x10^5$

t/y at SS; 1,856 t/y at SD; 4,068 t/y at PS; 5.3×10^5 t/y at SY; 258 t/y at SHF; and 50.2 t/y at CA. The significant annual degassing rates along structures provide evidence that many of these faults are conduits for fluids that are migrating throughout the Valles caldera and Albuquerque basin. These results also provide evidence that rift systems can release significant amounts of CO_2 over geologic time.

The results presented in this paper show the majority of HPSF and relatively high diffuse CO_2 fluxes are located directly over fault zones and around carbonic rich springs. The source of this CO_2 has a deeply derived component of fluid that ascends through the crust. This fluid also contains mantle helium and/or high concentrations of CO_2 (Crossey et al., 2009; Karlstrom 2013; and Newell et al., 2005). Fault damage zone widths were characterized by using a combination of flux groups and geospatial analyses of known or inferred fault locations. One of the faults at AC has a damage zone width that varies across the site from 24 m to 135 m. The Sulphur Creek fault is preferentially more damaged on its footwall (width = 117 m) than its hangingwall (width = 72 m). One potentially unknown fault at SD has a damage zone of 12m. Fault damage zones of the two major faults at SD are wider on their footwall sides (83m and 12m) compared to their hangingwall (13m and 0 m). The fault damage zone width along the Nacimiento fault increases from PS (20 m on its hangingwall and 0 m on its footwall) to SY (98 m on the hangingwall and 71 m on the footwall). At the SHF site, CO_2 flux measurements were not useful for determining damage zone, which ranges from 1 – 3 m at this location from fault scarps, but a distal damage zone component was determined from diffuse flux measurements. Faults at CA also have damage zones that could not be determined directly from CO_2 flux measurements due to the lack of HPSF, so distal damage zone widths were constrained. The four cemented faults at ZP all had background (except for 1 diffuse measurement) fluxes attesting to these faults being conduits to fluid flow in the past, but now have sealed themselves and are barriers to fluid flow, especially when compared to the carbonate cemented SHF.

These high CO_2 fluxes indicate the presence of a deeply derived fluid that is migrating up along permeable Quaternary faults. HPSF values range from 200 g_{CO2}/m^2d to 144,239 g_{CO2}/m^2d in and around the Valles caldera geothermal system (AC, SS, and SD), and from 13.2 g_{CO2}/m^2d to 149,322 g_{CO2}/m^2d in the Albuquerque basin. These high fluxes are attributed to the ascent of carbonic rich fluids that have a component of an endogenic source. Average surface CO_2 flux values at SS (754 g_{CO2}/m^2d), SD (97 g_{CO2}/m^2d), and AC (47 g_{CO2}/m^2d) are comparable to values other authors have obtained in similar geologic areas: 450 g_{CO2}/m^2d at the Latera caldera in Italy (Chiodini et al., 2007); 390 g_{CO2}/m^2d on acidic ground at the Hot Spring basin in the Yellowstone caldera (Werner et al., 2008); and 1,472 g_{CO2}/m^2d from Solfatara of Pozzouli geothermal field in Italy (Chiodini et al., 1998).

Extension, magmatism, and volcanism have been occurring around these sites in the Albuquerque basin and Valles caldera for millions of years. By studying the present day CO_2 flux insights are revealed into what the quantitative release of CO_2 may have been like in the central RGR over this time period, and the significant role rift systems play for understanding the global CO_2 budget for the present and geologic past.

References

Bartolino, J.R. and Cole, J.C., 2002, Ground-Water Resources of the Middle Rio Grande basin: U.S. Geological Survey Circular 1222, 132 p.

Bellentine, C.J., Schoell, M., Coleman, D., and Cain, B.A., 2001, 300-Myr-old magmatic CO_2 in natural gas reservoirs of the west Texas Permian basin: Nature, v. 409, p. 327-330.

Bergfeld, D., Goff, F., and Janik, C.J., 2001, Elevated carbon dioxide flux at the Dixie Valley geothermal field, Nevada; relations between surface phenomena and the geothermal reservoir: Chemical Geology, v. 177, p. 43-66.

Berglund, H.T., Sheehan, A.F., Murray, M.H., Roy, M., Lowry, A.R., Nerem, R.S., and Blume, F., 2012, Distributed Deformation Across the Rio Grande Rift, Great Plains, and Colorado Plateau: Geological Society of America, Geology, v. 40, p. 23-26.

Black, B. A., 1982, Oil and Gas Exploration in the Albuquerque basin: New Mexico Geological Society Guidebook, 33r Field Conference, p. 313 – 324.

Black, B.A., 2002, Surprises in Stratigraphy and Structure found during Hydrocarbon Exploration in the Rio Grande Rift, New Mexico: American Association of Petroleum Geologists Search and Discovery Article, Southwest Section Meeting, Ruidoso, New Mexico, p. 70-74.

Black, B.A., 2013, “Elephant Tracks” … In Search of a Possible “Giant”: Geological Society of America Abstracts with Programs, v. 45, no. 7, p. 443.

Black, B. A. and Hiss, W. L., 1974, Structure and stratigraphy in the vicinity of the Shell oil Co. Santa Fe Pacific No. 1 Test Well, Southern Sandoval, County, New Mexico: New Mexico Geological Society, Guidebook, 25th Field Conference, p. 365 – 370.

Blomgren, V., Hot Springs Hydrochemistry on Opposite sides of the Rio Grande Rift in Northern New Mexico and a Tie between Valles Caldera and Ojo Caliente: Thesis, University of New Mexico.

Borjesson, G. and Scensson, B.H., 1997, Seasonal and Diurnal Methane Emissions from a landfill and their Regulations by Methane Oxidation: Waste Management and Research, v. 15, p. 33-54.

Brothelande, E. and Merle, O., Estimation of magma depth for resurgent domes: An experimental approach: Earth and Planetary Science Letters, v. 412, p. 143-151.

Caine, J. A and Minor, S. A., 2009, Structural and geochemical characteristics of faulted sediments and inferences on the role of water in deformation, Rio Grande Rift, New Mexico: Geological Society of America, Bulletin, v. 121, no. 9/19, p. 1325-1340.

Carbone, M. S., Winston, G. C., and Trumbore, S.E., 2008, Soil respiration in perennial grass and shrub ecosystems: linking environmental controls with plant and microbial sources on seasonal and diel timescales: Journal of Geophysical Research, v. 113, p. 1-14.

Cardellini, C., Chiodini, G., and Frondini, F., 2003, Application of stochastic simulation to CO_2 flux from soil: Mapping and quantification of gas release: Journal of Geophysical Research, v. 108, no. B9, p. 3-1 – 3-13.

Chapin, C. E., 1971, The Rio Grande Rift, Part I: Modifications and Additions, in James, H.L., ed., San Luis basin (Colorado): New Mexico Geological Society 22nd Annual Fall Field Conference Guidebook, p. 191 – 201.

Chapin, C. E., and Cather, S. M., 1994, Tectonic setting of the axial basins of the northern and central Rio Grande rift: Geological Society of America, Special Paper 291, p. 5-25.

Chiodini, G., Cardellini, C., Amato, A., Boschi, E., Caliro, S., Frondini, F., and Ventura, G., 2004, Carbon Dioxide Earth Degassing and seismogenisis in central and southern Italy: American Geophysical Union, Geophysical Research Letters, v. 31, 4 p.

Chiodini, G., Cioni, R., Guidi, M., Raco, B., and Marini, L., 1998, Soil CO_2 flux measurements in volcanic and geothermal areas: Applied Geochemistry, v. 13, no. 5, p. 543-552.

Chiodini, G., F. Frondini, D.M. Kerrick, J. Rogie, F. Parello, L. Peruzzi, and A.R. Zanzari, 1999, Quantification of Deep CO_2 Fluxes from Central Italy: Examples of Carbon Balance for Regional Aquifers and of Soil Diffuse Degassing: Chemical Geology, v. 159, no. 1–4, p. 205–222.

Chiodini, G., Baldini, A., Barberi, F., Carapezza, M.L., Cardellini, C., Frondini, F., Granieri, D., and Ranaldi, M., 2007, Carbon dioxide degassing at Latera Caldera (Italy): Evidence of geothermal reservoir and evaluation of its potential energy: Geophysical Research, v. 112, 17 p.

Chiodini, G., Caliro, S., Cardellini, C., Avino, R., Granieri, D., and Schmidt, A., 2008, Carbon isotopic composition of soil CO_2 efflux, a powerful method to discriminate different sources feeding soil CO_2 degassing in volcanic-hydrothermal areas: Earth and Planetary Science Letters, v. 274, p. 372-379.

Connell, S.D., Koning, D.J., and Cather, S.M., 1999, Revisions to the stratigraphic nomenclature of the Santa Fe Group, northwestern Albuquerque basin, New Mexico: New Mexico Geological Society Guidebook, 50th Field Conference, Albuquerque Geology, p. 337-354.

Connell, S.D., 2006, Preliminary Geologic Map of the Albuquerque-Rio Rancho Metropolitan Area and Vicinity, Bernalillo and Sandoval Counties, New Mexico: New Mexico Bureau of Geology and Mineral Resources, Open-File Report 496, Plate 2, version 2.0.

Cron, B., 2011, Geochemical Characteristics and Microbial Diversity of CO_2-Rich Mound Springs of the Tierra Amarilla Anticline, New Mexico: M.S. Thesis, University of New Mexico,122 p.

Crossey, L. J., Fischer, P., Ptchett, J., Karlstrom, K. E., Hilton, D. R., Newell, D. L., Huntoon, P., Reynolds, A. C., and de Leeuw, A. M., 2006, Dissected hydrologic system at the Grand Canyon: Interaction between deeply derived fluids and plateau aquifer waters in modern springs and travertine: Geological Society of America, Geology, v. 34, no. 1, p. 25 – 28.

Crossey, L.J., Karlstrom, K.E., Springer, A.E., Newell, D., Hilton, D.R., and Fischer, T., 2009, Degassing of mantle-derived CO_2 and He from springs in the southern Colorado Plateau region-Neotectonic connections and implication for groundwater systems: Geological Society of America Bulletin, v. 121, no. 7/8, p. 1034-1053.

Crossey, L.J., Karlstrom, K.E., Schmandt, B., R.R. Crow, Colman, D.R., Cron, B., Takacs-Vesbach, C.D., Dahm, C.N., Northup, D.E., Hilton, D.R., Ricketts, J.W., Lowry, A.R., 2016, Continental smokers couple mantle degassing and distinctive microbiology within continents: Earth and Planetary Science Letters, v. 435, p. 22-30.

Dlugokencky, E. and Tans, P, 2016, Recent Global Monthly Mean CO_2: National Oceanic Atmospheric Administration and Earth Systems Research Laboratory. URL www.esrl.noaa.gov/gmd/ccgg/trends/ (accessed on April 18, 2016).

Drever, J.I., 1988, The Geochemistry of Natural Waters: Pearson Education Canada, 437 p.

Emmerich, W. E., 2003, Carbon dioxide fluxes in a semiarid environment with high carbonate soils: Agricultural and Forest Meteorology, v. 116, p. 91-102.

Erickson, D.J., Mills, R.T., Gregg, J., Blasing, T.J., Hoffman, F.M., Andres, M.D., Zhu, Z., and Kawa, S.R., 2008, An estimate of monthly global emmissions of anthropogenic CO_2: Impact on the seasonal cycle of atmospheric CO_2: Geophysical Research, v. 113, 10 p.

Fischer, T.P., Giggenbach, W.F., Sano, Y., and Williams, S.N., 1998, Fluxes and sources of volatiles discharged from Kudryavy, a subduction zone volcano, Kurile Islands: Earth and Planetary Science Letters, v. 160, p. 81-96.

Gautheron, C. and Moreira, M., Helium signature of the subcontinental lithosphere mantle: Earth and Planetary Science Letters, v. 199, p. 39-4.

Giggenbach, W.F., 1992, The composition of gases in geothermal and volcanic systems as a function of tectonic setting, *in* Kharaka, Y.K., and Maest, K., eds., Proceedings of the 7th International Symposium on Water-Rock Interaction: Rotterdam, A.A. Balkema, p. 873–878.

Giggenbach, W.F., 1992, The composition of gases in geothermal and volcanic systems as a function of tectonic setting: Water-Rock Interaction, p. 873-878

Giggenbach, W.F., 1995, Variations in the chemical and isotopic composition of fluids discharged from the Taupo Volcanic Zone, New Zealand: Volcanology and Geothermal Research, v. 68, p. 89-116.

Goff, F., Gardner, J., Vidale, R., and Charles, R., 1985, Geochemistry and isotopes of fluids from Sulphur Springs, Valles Caldera, New Mexico: Volcanology and Geothermal Research, v. 23, p. 237-297.

Goff, F. and Gardner, J. N., 1994, Evolution of a Mineralized Geothermal System, Valles Caldera, New Mexico: Economic Geology, v. 89, p. 1803 – 1832.

Goff, F. and Shevenell, L., 1987, Travertine deposits of Soda Dam, New Mexico, and their implications for the age and evolution of the Valles Caldera hydrothermal system: Geological Society of America Bulletin, v. 99, p. 292-302.

Goff, F. and Janik, 2002, Gas geochemistry of the Valles Caldera region, New Mexico and comparisons with gases at Yellowstone, Long Valley and other geothermal systems: Volcanology and Geothermal Research, v. 116, p. 299-323.

Goff, F., 2009, Valles Caldera: a Geologic History: University of New Mexico Press, 1st ed.

Goff, F., Gardner, J.N., Reneau, S.L., Kelley, S.A., Kempter, K.A., Lawrence, J.R., 2011, Geologic Map of the Valles caldera, Jemez Mountains, New Mexico: New Mexico Bureau of Geology and Mineral Resources, Geologic Map 79.

Grauch, V.J.S., and Connell, S.D., 2013, New perspectives on the geometry of the Albuquerque basin, Rio Grande rift, New Mexico: Insights from geophysical models of rift-fill thickness, *in* Hudson, M.R., and Grauch, V.J.S., eds., New Perspectives on Rio Grande Rift basins: From Tectonics to Groundwater: Geological Society of America Special Paper 494, p. 427–462.

Hancock, P.L., Calmers, R.M.L., Altunnel, E., and Cakir, Z., 1999, Travitonics: using travertines in active fault studies: Structural Geology, v. 21, p. 903-916.

Heiken, G., Goff, F., Gardner, J.N., and Baldridge W.S., 1990, The Valles/Toledo Caldera Complex, Jemez Volcanic Field, New Mexico: Annual Review of Earth and Planetary Sciences, v. 18, p. 27-53.

Heynekamp, M.R., Goodwin, L.B., Mozley, P.S., and Haneberg, W.C., 1999, Controls on Fault-Zone Architecture in poorly lithified sediments, Rio Grande Rift, New Mexico: Implications for fault-zone permeability and fluid flow: in Faults and Subsurface Fluid Flow in the Shallow Crust, American Geophysical Union Geophysical Monograph 113, p. 27-49.

Huxman, T.E., Snyder, K.A., Tissue, D., Leffler, A.J., Ogle, K., Pockman, W.T., Sandquist, D.R., Potts, D.L., and Schwinning, S., 2004, Precipitation pulses and carbon fluxes in semiarid and arid ecosystems: Oecologia, v. 141, no. 2, p. 254-268.

Karlstrom, K.E., Cather, S.M., Kelley, S.A., Heizler, M.T., Pazzaglia, F.J., and Roy, M., 1999, Sandia Mountains and Rio Grande Rift: Ancestry of structures and history of deformation: New Mexico Geological Society Guidebook, 50th Field Conference, Albuquerque Geology, p. 155-166.

Karlstrom, K.E., Crossey, L.J., Hilton, D.R., and Barry, P.H., 2013, Mantle ^{3}He and CO_2 degassing in carbonic and geothermal springs of Colorado and implications for neotectonics of the Rocky Mountains: Geological Society of America Geology, published online as doi:10.1130/G34007.1.

Keller, R.G. and Baldridge, W.S., 1999, The Rio Grande rift: A geological and geophysical overview: Rocky Mountain Geology, v. 34, no. 1, p. 121-130.

Kelley, S.A. and Chamberlin, R.M., 2012, Our Growing Understanding of the Rio Grande Rift: New Mexico Earth Matters, v. 12, no. 2, p. 1-4.

Kelley, S., Kempter, K.A., Goff, F., Rampey, M., Osburn, G.R., Ferguson, C.A., 2003, Geologic Map of the Jemez Springs Quadrangle, Sandoval County, New Mexico: New Mexico Bureau of Geology and Mineral Resources, Open-file Digital Geologic Map OF-GM 073.

Kerrick, D.M., 2001, Present and Past Nonanthropogenic CO2 Degassing from the Solid Earth: American Geophysical Union, v. 39, no. 4, p. 565-585.

Kucks, R.P., Hill, P.L., and Heywood, C.E., 2001, New Mexico Aeromagnetic and gravity maps and data: a web site for distribution of data: U.S. Geological Survey Open-file report 01-0061, http://pubs.usgs.gov/of/2001/ofr-01-0061/html/newmex.htm

Lee, H., Muirhead, J. D., Fischer, T. P., Edinger, C. J., Kattenhorn, S. A., Sharp, Z. D., and Kianji, G., 2016, Massive and prolonged deep carbon emissions associated with continental rifting: Nature Geoscience Letters, p. 1-6.

Lewicki, J.L. and Brantley, S.L., 2000, CO_2 degassing along the San Andreas fault, Parkfield, California: Geophysical Research Letters, v. 27, no. 1, p. 5-8.

Lewicki, J. L., Connor, C., St-Amand, K., and Spinner, W., 2003, Self-potential, soil CO_2 flux, and temperature on Masaya volcano, Nicaragua: Geophysical Research Letters, v. 30, no. 15, p. 2-1 – 2-4.

Ma, S., Baldocchi, D. D., Hatala, J. A., Detto, M., and Yuste, C., 2012, Are rain-induced ecosystems respiration pulses enhanced by legacies of antecedent photodegradation in semi-arid environments: Agricultural and Forest Meteorology, v. 154-155, p. 203-213.

Machette, M.N., Personius, S.F., Kelson, K.I., Dart, R.L., Haller, K.M., 2000, Map and data for Quaternary faults and folds in New Mexico: United States Geological Survey, Open-File Report 98-521 (electronic version), 367 p.

McGibbon, C., 2015., Carbonic Springs as Distal Manifestations of the Jemez Geothermal System, SanYsidro, New Mexico, Highlighting the Importance of Fault Pathways and Hydrochemical Mixing: M.S. Thesis, University of New Mexico, 123 p.

Minor, S.A. and Hudson, M.R., 2006, Regional survey of structural properties and cementation patterns of fault zones in the northern part of the Albuquerque basin, New Mexico-Implications for ground-water flow: United States Geological Survey Professional Paper 1719, 34 p.

Mozley, P. S. and Goodwin, L.B., 1995, Patterns of cementation along a Cenozoic normal fault: A record of paleoflow orientations: Geology, v. 23, no. 6, p. 539 – 542.

Newell, D.J., Crossey, L.J., Karlstrom, K.E., and Fischer, T.P., 2005, Continental-scale links between the mantle and groundwater systems of the western United States: Evidence from travertine springs and regional He isotope data: Geological Society of America Today, v. 15, no. 12, p. 4-10.

Phillips, E. H., Goff, F., Kyle, P.R., McIntosh, W. C., Dunbar, N. W., and Gardner, J. N., 2007: The ^{40}Ar/^{39}Ar age constraints on the duration of resurgence at the Valles caldera, New Mexico: Geophysical Research, v. 112, 15 p.

Piper, A.M., 1944, A Graphic Procedure in the Geochemical Interpretation of Water-Analysis: American Geophysical Union, Transactions, v. 25, is. 6, p. 914-928.

Plummer, N.L., Bexfield, L.M., Anderholm, S.K., Sanford, W.E., Eurybiades, B., 2012, Geochemical characterization of ground-water flow in the Santa Fe Group aquifer system, Middle Rio Grande basin, New Mexico: United States Geological Survey, Water-Resources Investigation Report 03-4131, v. 1.2. 414 p.

Priewisch, A., 2014, Characterization of Quaternary large-volume travertine deposits in the southwestern United States and their implications for CO_2 sequestration: University of New Mexico Lobo Vault, Doctor of Philosophy Dissertation, 164 p.

Renick, B.C. 1931, Geology and ground-water resources of western Sandoval County New Mexico: United States Geological Survey, Water Supply Paper 620. 135 p.

Ricketts, J.W. and Karlstrom, K.E., 2014, Geologic Map of the South Garcia SE 7.5-minute Quadrangle, Valencia County, New Mexico: New Mexico Bureau of Geology and Mineral Resources, Open-file Geologic Map OF-GM 246.

Ricketts, J. W., Karlstrom, K. E., Priewisch, A., Crossey, L. J., Polyak, V. J., and Asmerom, Y., 2014, Quaternary extension in the Rio Grande rift at elevated strain rates recorded in travertine deposits, central New Mexico: Lithosphere, v. 6, no. 1, p. 3-16.

Ricketts, J. W., Karlstrom, K. E., and Kelley, S. A., 2015, Embryonic core complexes in narrow continental rifts: The importance of low-angle normal faults in the Rio Grande rift of central New Mexico: Geosphere, v. 11, no. 2, p. 1-20.

Russell, L. R. and Snelson, S., 1994, Structure and tectonics of the Albuquerque basin segment of the Rio Grande rift: Insights from reflection seismic data, in Keller, G.R., and Cather, S.M., eds., basins of the Rio Grande Rift: Structure, Stratigraphy, and Tectonic Setting: Boulder, Colorado, Geological Society of America Special Paper 291, p. 83-112.

Schmandt, B. and Lin, F., 2014, P- and S-wave tomography of the mantle beneath the United States: Geophysics Research Letters, v. 41, 6342-6349.

Scholle, P., 2003, Geologic Map of New Mexico: New Mexico Bureau of Geology and Mineral Resources.

Sharp, Z., 2007, Principles of Stable Isotope Geochemistry*:* Upper Saddle River, N.J.: Pearson/Prentice Hall.

Siegel, D.I., Lesniak, K.A., and Stute, M., 2004, Isotopic geochemistry of the Saratoga springs: Implications for the origin of solutes and source of carbon dioxide: Geological Society of America, v. 32, no. 3, p. 257-260.

Sinclair, A.J., 1974, Selection of threshold values in geochemical data using probability graphs: Geochemical Exploration, v. 3, p. 129-149.

Spell, T.L., Kyle, P.R., and Baker, J., 1996, Geochronology and geochemistry of the Cerro Toledo Rhyolite: New Mexico Geological Society Guidebook, 47th Field Conference, Jemez Mountain Region, p. 263-268.

Sponseller, R. A., 2007, Precipitation pulses and soil CO_2 flux in a Sonoran Desert ecosystem: Global Change Biology, v. 13, p. 426-436.

Tafoya, J.A., 2012, Uranium-Series Geochronology and Stable Isotope Analysis of Travertine from Soda Dam, New Mexico: A Quaternary Record of Episodic Spring Discharge and River Incision in the Jemez Mountains Hydrothermal System: M.S. Thesis, University of New Mexico, 112 p.

Tang, S., Zhang, Y., Guo, Y., Zhai, X., Wilkes, A., Han, G., Jiang, Y., Liu, K., Zhou, P., Wang, K., and Wang, C., 2015, Changes of soil CO_2 flux under different stocking rates during spring-thaw period in a northern desert steppe, China: Atmospheric Environment, v. 122, p. 343-348.

Truesdell, A.H. and Janik, C. J., 1986, Reservoir Processes and Fluid Origins in the Baca Geothermal System, Valles Caldera, New Mexico: Geophysical Research, v. 91, no. B2, p. 1817-1833.

Vargas, R., Collins, S. L., Thomey, M. L., Johnson, J. E., Brown, R. F., Natvig, D. O., and Friggens, M. T., 2012, Precipitation variability and fire influence temporal dynamics of soil CO_2 efflux in an arid grassland: Global Change Biology, v. 18, p. 1401-1411.

Werner, C., Hurwitz, S., Evans, W. C., Lowenstern, J. B., Bergfeld, D., Heasler, H., Jaworowski, C., Hunt, A., 2008, Volatile emissions and gas geochemistry of Hot Springs basin, Yellowstone National Park, USA: Journal of Volcanology and Geothermal Research, v. 178, p. 751-762.

Williams, A.M., Crossey, L.J., Karlstrom, K.E., Newell, D., Person, M., Woolsey, E., 2013, Hydrochemistry of the Middle Rio Grande aquifer System-Fluid mixing and salinization of the Rio Grande due to fault inputs: Chemical Geology, v. 351, p. 281-298.

Woodward, L.A. and Ruetschilling, R.L., 1976, Geology of San Ysidro Quadrangle, New Mexico: New Mexico Bureau of Mines and Mineral Resources, Geologic Map 37.

Zhou, Z., Ballentine, C.J., Kipfer, R., Schoell, M., and Thibodeaux, S., 2005, Noble gas tracing of groundwater/coalbed methane interaction in the San Juan basin: Geochimica et Cosmochimica Acta, v. 69, no. 23, p. 5413-5428.

Zimmerer, M.J., Lafferty, J., and Coble, M.A., 2016a, The eruptive and magmatic history of the youngest pulse of volcanism at the Valles caldera: Implications for successfully dating late Quaternary eruptions: Volcanology and Geothermal Research, v. 310, p. 50-57.

Zimmerer, M. J., Lafferty, J., and Ramos, R.C., 2016b, Volcanic Hazards at the Southwest’s Supervolcano: Ongoing Efforts to Temporally Dissect the Eruptive and Magmatic History of the Valles Caldera: New Mexico Geological Society, Spring 2016 Meeting, Abstract.

Figures and Tables

Figure 1: Simplified geologic map with hill shade relief of the Albuquerque basin. White line is the cross section line for Figure 3. The inset map shows major physiographic provinces surrounding the Albuquerque basin and Rio Grande rift (orange outline). Site locations for this study are: AC = Alamo Canyon; SS = Sulphur Spring; SD = Soda Dam; PS = Penasco Springs; ZP = Zia Pueblo; SY = San Ysidro; SHF = Sand Hill Fault; CA = Carrizo Arroyo. SFP 1 = Santa Fe Pacific #1 well. Faults are from Machette et al. (2000) and Scholle (2003). Albuquerque basin outline (purple line) modified from Grauch and Connell (2013); geologic map modified from Scholle (2003); Outline of Socorro magma body modified from Ricketts et al., 2015

Figure 2: $^3He/^4He$ ratios (R_C), reported relative to air (R_A), of springs plotted on mantle tomography of relative shear-wave (s-wave) velocities imaged at 60 km depth (Schmandt and Lin, 2014). Slow mantle velocities (red) indicate the presence of partial melt at this depth. $^3He/^4He$ ratios above 0.1 R_A indicate degassing of mantle helium from springs with CO_2, which is an important carrier gas (Karlstrom et al., 2013, Blomgren, 2016). Green dots are locations of the CO_2 flux sites of this study (see Figure 1 for site abbreviations). Blue dashed line through the map is the Jemez Volcanic Lineament, following areas of partial melt at this depth. See Appendix C for table of He data (also published in Crossey et al., 2015).

Figure 3: Cross section of northern Albuquerque basin (see Figure 1 for reference line). Base of Santa Fe Group from Grauch and Connell (2013) geophysical data. Faults are from Machette et al., 2000 and Scholle, 2003. Mesozoic and Paleozoic thicknesses from Santa Fe Pacific # 1 well (Black and Hiss, 1974). Cementation on either the hangingwall or footwall based on Minor and Hudson, 2006 (see Figure 6 for map view of cemented faults). Arrows show idealized flowpaths; bubbles show schematic locations for derivation of endogenic CO_2 (C_{endo}) versus CO_2 dissolved in carbonate aquifers (C_{carb}). The structure of the brittle-ductile transition zone was taken from Kucks et al (2001) isostatic gravity anomaly map, and correlates well with Connell (2006) depth and structure of the brittle-ductile transition zone.

Figure 4: Site photographs for Alamo Canyon (A and B), Sulphur Springs (C and D), and Soda Dam (E). CO_2 degassing at a carbonic rich pond (A) and the marsh like valley (B) at Alamo Canyon. Fumarolic activity (C) and active CO_2 degassing at Tony's mud spring (D) at Sulphur Springs. Fissure-ridge style travertine deposit at Soda Dam (E) with the Jemez river to the right of the photograph.

Figure 5: Site photographs for Penasco Springs (A), Zia Pueblo (B), San Ysidro (C and D), Sand Hill Fault (E), and Carrizo Arroyo (F). One of many travertine mounds at Penasco Springs (A). Carbonate cemented fault, with a man to the

lower left for scale, where the cement is more prominent on the hangingwall (east-side) of the fault (B). View of the San Ysidro site (C) showing the large fissure-ridge style travertine deposits surrounded by outcropping rocks that make up the Tierra Amarilla anticline. Mound style travertine deposits (D) at San Ysidro, commonly referred to as the Twin Mounds. Carbonate cemented Sand Hill fault (E) with the cement on the hangingwall (east-side). Looking down transect (looking west) at Carrizo Arroyo (F), where change in lithology (reddish to greyish colors) is from the Triassic Moenkopi Formation to the Permian San Andres Formation, respectively.

Figure 6: Map view of cemented faults in the northern Albuquerque basin (modified from Minor and Hudson, 2006). Green circles are site locations from this study – see Figure 1 for details about site locations. LB = La Bajada fault; NC = Nacimiento fault; PB = Pico Butte fault; SF = San Francisco fault; SY = San Ysidro fault; SHF = Sand Hill fault; SA = Santa Ana fault network; SI = Sile fault;

Figure 7: Schematic of fault zones that produce carbonic rich springs that deposit travertines (modified from Priewisch, 2014). Intersecting faults produce high point source fluxes (HPSF) measured on the surface. Arrows show schematic fluid flow paths. Bubbles show examples for locations of background, diffuse, and HPSF CO_2 fluxes. HPSF are found at spring vents and along faults; diffuse or above background fluxes are found on both sides of faults and are interpreted to reflect fracture permeability in a wide fault damage zone; background values differ from site to site and are interpreted to reflect mainly biological CO_2.

Figure 8: Schematic of CO_2 flux device and proper use in the field. Photo is from Alamo Canyon. The accumulation chamber circulates the CO_2 gas into the CO_2 infrared analyzer then out back into the chamber maintaining a closed system. Gas samples are collected on the out-flow.

Figure 9: Example of using measured data to define flux groups (data comes from the SY site). Measured CO_2 flux values are plotted on a log scale cumulative probability plot to locate inflection points (black arrows) indicating the presence of a polymodal distribution of values. Inflection points are used to define distinct unimodal distributions of data that are classified herein as groups. Solid lines are trend lines through the redistributed data groups that are used to select threshold values. When overlaps exist, threshold values are selected from the trend lines by taking the 99% of the next lower group and the 1% of the above group. Dashed lines represent threshold values for HPSF (>42.7 g_{CO2}/m^2d), combination of HPSF and diffuse (5.1 – 42.7 g_{CO2}/m^2d), diffuse (1.3 – 5.1 g_{CO2}/m^2d), and background (< 1.3 g_{CO2}/m^2d). The arrows indicate the log CO_2 flux threshold values used to separate groups.

Figure 10: Alamo Canyon CO_2 flux Analysis. **A)** CO_2 flux bubbles grouped by background, combination of background and diffuse, diffuse, and HPSF plotted on the local geology (geology modified from Goff et al., 2011). The main sources of HPSF appear to be the two E-W trending faults that run parallel to the canyon, and one fault to the southeast. Dashed lines are inferred faults and solid lines are well constrained faults. **B1)** Cross section showing CO_2 flux and the elevation profile (solid black line) across the two E-W trending faults (cross section line shown on B2). This cross section was used to obtain fault damage zone (red dashed lines) and distal damage zone (blue dashed lines) widths shown on B2. **B2)** Fault damage zone (red) and distal damage zone (blue) generated from inset B1 (Lee et al., 2016). Yellow stars are HPSF locations and orange dots are diffuse and combination of background and diffuse points. **C1 and C2)** Cross section showing CO_2 flux and elevation profile for the southeast fault (C1), and fault damage zone and distal damage zone along the southeast fault (C2). **D)** Cumulative probability (%) plot used to group the different CO_2 fluxes.

Figure 11: Sulphur Springs CO_2 flux Analysis. **A)** CO_2 flux bubbles grouped by diffuse, combination of diffuse and HPSF, and HPSF plotted on local geology (geology from Goff et al., 2011). Solid black lines are well constrained faults and dashed black lines are inferred faults. The majority of HPSF were measured on the dry surface and appear to be located around the Sulphur Creek fault, with significant fluxes also present to the south-southwest of the site. **B)** Cumulative probability (%) plot used to group the different CO_2 fluxes. **C)** Cross section with elevation and CO_2 fluxes projected onto the A-A' line shown on inset D. **D)** Fault damage zone (red) and distal fault damage zone (blue) generated from inset C. There is a larger damage zone on the southern hangingwall side of the Sulphur Creek normal fault. Yellow stars are HPSF locations and orange dots are diffuse and combination of HPSF and diffuse. The inferred fault to the south-southwest could be promoting higher fluxes measured at this location.

Figure 12: Soda Dam CO_2 flux Analysis. **A)** CO_2 flux bubbles grouped by background, diffuse, combination of diffuse and HPSF plotted on local geology (geology modified from Kelly et al., 2003 and Karlstrom, unpublished). Solid black lines are well constrained faults and dashed black lines are inferred faults. Stick and ball indicates the hangingwall sides of the normal faults. There appears to be relatively higher CO_2 fluxes around the Jemez and Soda Dam fault. **B)** Cumulative probability (%) plot used to group the different CO_2 fluxes. **C)** Cross section with elevation and CO_2 fluxes projected onto the A-A' line shown on inset D. **D)** Fault damage zone (red) and distal fault damage zone (blue) generated from inset C. Yellow stars are HPSF locations and orange dots are diffuse and combination of HPSF and diffuse fluxes. There may be a possible unmapped fault to the north where a HPSF was measured on the dry surface. Wider damage zones are seen on the southern footwall sides of the faults.

Figure 13: Penasco Springs CO_2 flux analysis**. A)** CO_2 flux bubbles grouped by background, combination of background and diffuse, diffuse, and HPSF plotted on local geology (geology modified from Woodward and Reutschilling, 1976). Solid line is the Nacimento fault, that has been reactivated as a normal fault. Relatively higher CO_2 fluxes were measured at carbonic rich springs and along the Nacimento fault. **B)** Cumulative probability (%) plot used to group the different CO_2 fluxes. **C1 and D1)** Cross sections with elevation and CO_2 fluxes projected onto the A-A' and B-B' lines shown on insets C2 and D2. **C2 and D2)** Fault damage zone (red) and distal fault damage zone (blue) widths generated from insets C1 and D1. Yellow stars are HPSF locations and orange dots are diffuse and background fluxes. Larger damage zones appear on the eastern sides of the inferred fault (dashed line – D2) and Nacimento fault (C2). The main N-S trending inferred fault on inset D2 aligns with active carbonic rich springs and travertine mounds to the north.

Figure 14: San Ysidro CO_2 flux analysis**. A)** CO_2 flux bubbles grouped by background, diffuse, combination of diffuse and HPSF, and HPSF plotted on local geology (geology modified from Woodward and Reutschilling, 1976 and Karlstrom, unpublished). Solid black lines are well constrained faults and dashed black lines are inferred/buried faults. Dashed red line is the Tierra Amarilla anticline (TA). The Nacimiento fault is a thrust fault that has been reactivated as a normal fault, which is indicated with the ball and stick and box on the east side of the fault. **B)** Cumulative probability (%) plot used to group the different CO_2 fluxes. **C)** Cross section with elevation and CO_2 fluxes projected onto the A-A' line shown on inset D. The fault damage zones are depicted by red dashed lines and the distal fault damage zones by blue dashed lines on inset C. **D)** Fault damage zone (red) and distal fault damage zone (blue) generated from inset C. Yellow stars are HPSF locations and orange dots are diffuse, combination of diffuse and HPSF, and background fluxes. The width of the Nacimiento fault zone (~170 m) is interpreted to be the damage zone (red) at this site, where the Nacimiento fault zone has increased between PS (20 m) and SY (170 m).

Figure 15: Zia Pueblo CO_2 flux analysis. **A)** CO_2 flux bubbles grouped by background and diffuse plotted on local geology (geology modified from Scholle, 2003 and Machette et al., 2000). **B)** Cumulative probability (%) plot used to group the different CO_2 fluxes. This figure illustrates what a background flux in the Albuquerque basin is. It also demonstrates how cemented faults may be barriers to fluid flow. The three locations to the west (1, 2, and 3) were taken along carbonate cemented faults, and the location to the northeast (4) was taken along a silica cemented fault where one diffuse flux measurement was taken at this site.

Figure 16: Sand Hill Fault CO_2 flux analysis**. A)** CO_2 flux bubbles grouped by background, combination of background and diffuse, and diffuse flux plotted on general geology (geology modified from Scholle, 2003 and Machette et al.,

2000). Here, upper Santa Fe Group offsets lower Santa Fe Group rocks. **B)** Cumulative probability (%) plot used to group the different CO_2 fluxes. **C)** Cross section with elevation and CO_2 fluxes projected onto the A-A’ line shown on inset D. **D)** damage zone (blue) generated from inset C. Orange dots are diffuse, background, and combination of background (see A).

Figure 17: Carrizo Arroyo CO_2 flux analysis**. A)** CO_2 flux bubbles grouped by background, combination of background and diffuse, and diffuse flux plotted on local geology (geology modified from Ricketts and Karlstrom, 2014). CO_2 flux increases from background to above background approaching the Santa Fe Fault going west. The highest CO_2 fluxes measured were near the Comanche fault where there are travertine deposits. **B)** Cumulative probability (%) plot used to group the different CO_2 fluxes. **C)** damage zone (blue) generated from inset D. Orange dots are diffuse, background, and combination of background, see inset A. **D)** Cross section with elevation and CO_2 fluxes projected onto the A-A’ line shown on inset C.

Figure 18: Relative abundances of N_2, He, and Ar plotted on a ternary diagram (Fischer et al., 1998; Giggenbach, 1992). Mixing lines are traced between air, air saturated water, and deeply derived (endogenic) sources. Samples collected by various authors at these sites plot on the mixing line between deeply-derived volatiles and air. The values from this study, except for one (San Ysidro), plot near the air value, where the gas coming out of the ground most likely mixed with air. Various authors include Truesdell and Janik, 1986; Goff and Janik, 2002; and Newell et al., 2005 (See Appendix D for results table)

Figure 19: Histograms comparing the total CO_2 released in tons/year (A) and average CO_2 flux in g_{CO2}/m^2d (B) at sites in the Valles caldera and Albuquerque basin. Valles caldera sites are in bold. **A)** Shows the total amount of CO_2 released at each site that was calculated by taking the area of the fault damage zone and distal damage zone, and multiplying these areas times their average CO_2 flux. These results are considered to be real values for the total amount of CO_2 released at each site with respect to faults. However, some sites have larger fault zone areas than others (e.g. SY [2.8 km^2] is larger than SS [0.1 km^2]). The area of the travertine deposit and multiple carbonic springs at SY clearly show that this is not just an artifact of area, but a combination of multiple processes **B)** Although, AC and SY are releasing the most CO_2, SS, on average, has the highest CO_2 degassing rate per meter squared than any other site. These histograms show that fault zone areas should be considered when evaluating CO_2 degassing from the solid Earth.

Figure 20: Comparison of $^3He/^4He$ ratios of springs (A) and the highest measured dry surface CO_2 flux at each site (B) plotted on mantle tomography. The highest measured surface CO_2 flux is in parentheses in units of g_{CO2}/m^2d. There is good correlation between decreasing He ratios and maximum CO_2 surface flux going south away from the Valles caldera. There is a slight increase in

maximum surface CO_2 flux at Carrizo Arroyo near the Socorro magma body. Green dots are site locations for this study. See Figure 1 for description of abbreviations and Figure 2 for more details about $^3He/^4He$ ratios and mantle tomography).

Figure 21: Histogram of maximum background CO_2 fluxes attributed to soil and biology from various locations from around the world compared with the Albuquerque basin. All sites in the Albuquerque basin were considered for this graph. Well-watered and fertilized grass measurements were taken outside on the lawn of Northrop Hall (Earth and Planetary Sciences, Albuquerque, New Mexico) to give some context to these values. This graph shows background values in arid lands can vary with biology, but are generally low, and background values for this study are suitable for arid lands. Data from Tang et al., 2015, Ma et al., 2012, Vargas et al., 2012, Carbone et al., 2008, and Sponseller, 2007.

Figure 22: Histogram comparing average CO_2 fluxes from various sites around the world. Red dotted line separates geothermal sites to the left from tectonic sites to the right. Sites from this study are bolded. The purpose of this graph is to show that sites in the Rio Grande Rift can be considered world class in terms of their high CO_2 flux, and to give context for CO_2 fluxes seen in similar geothermal and tectonic settings. Most of the area sizes covered by these CO_2 flux surveys are similar. The areas covered by the CO_2 flux surveys for these sites are as follows: Solfatera Crater site in the Phlegraen Caldera is $9.0x10^4$ m^2 (Chiodini et al., 1998); Horseshoe Lake in Mammoth mountain, CA is $2.8x10^5$ m^2 (Werner et al., 2014); Sulphur Springs is $8.8x10^4$ m^2; Western basin site in the Hot Spring Basin (HSB) at the Yellow Stone caldera is $1.6x10^5$ m^2 (Werner et al., 2008); Soda Dam is $3.2x10^4$ m^2; Dixie Valley CO_2 flux survey is $1.7x10^5$ m^2 (Bergfeld et al., 2001); Alamo Canyon is 2.3 $x10^5$ m^2; and Magadi Basin in the East African rift is $4.1x10^8$ (Lee et al., 2016).

Table 1: Analytical Results for CO_2 Flux Measurements by site and by type of media collected on.

Table 2: Local Threshold values for CO_2 flux at Each site

Table 3: Comparison of CO_2 flux from various geothermal and magmatic systems

Figure 1

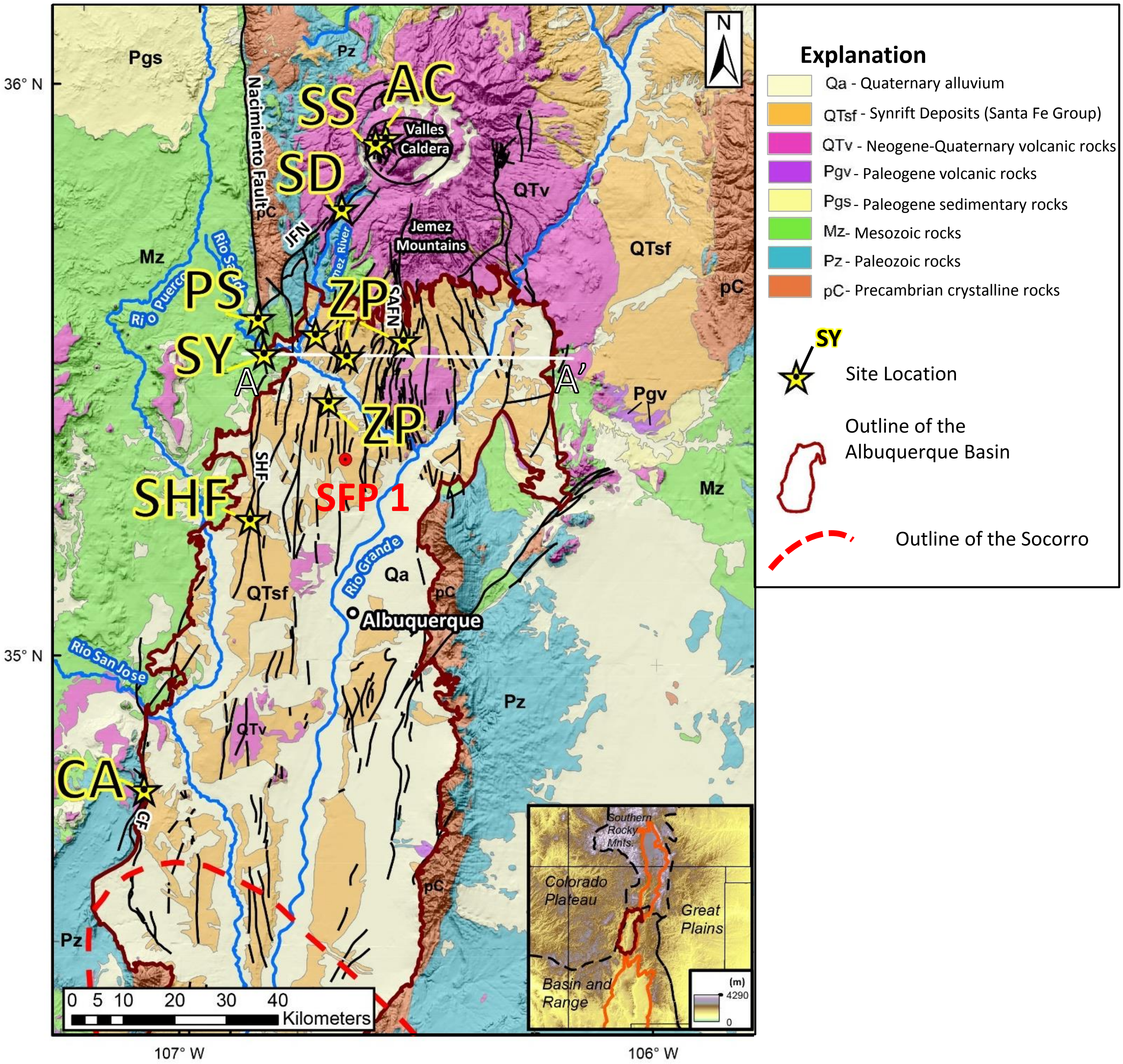
N
36° N
35° N
107° W
106° W
Pgs
Pz
AC
SS
Valles
Caldera
SD
Nacimiento Fault
pC
JFN
Jemez River
Jemez
Mountains
QTv
QTsf
Mz
Rio Salado
Rio Puerco
PS
ZP
SAFN
pC
SY
A
A'
ZP
Pgv
SHF
SFP 1
SHF
Mz
Rio Grande
Qa
QTsf
pC
Albuquerque
Rio San Jose
Pz
QTv
CA
GF
pC
Pz
0 5 10 20 30 40
Kilometers
Southern
Rocky
Mnts.
Colorado
Plateau
Great
Plains
Basin and
Range
(m)
4290
0
Explanation
Qa - Quaternary alluvium
QTsf - Synrift Deposits (Santa Fe Group)
QTv - Neogene-Quaternary volcanic rocks
Pgv - Paleogene volcanic rocks
Pgs - Paleogene sedimentary rocks
Mz- Mesozoic rocks
Pz - Paleozoic rocks
pC- Precambrian crystalline rocks
SY
Site Location
Outline of the
Albuquerque Basin
Outline of the Socorro

Figure 2

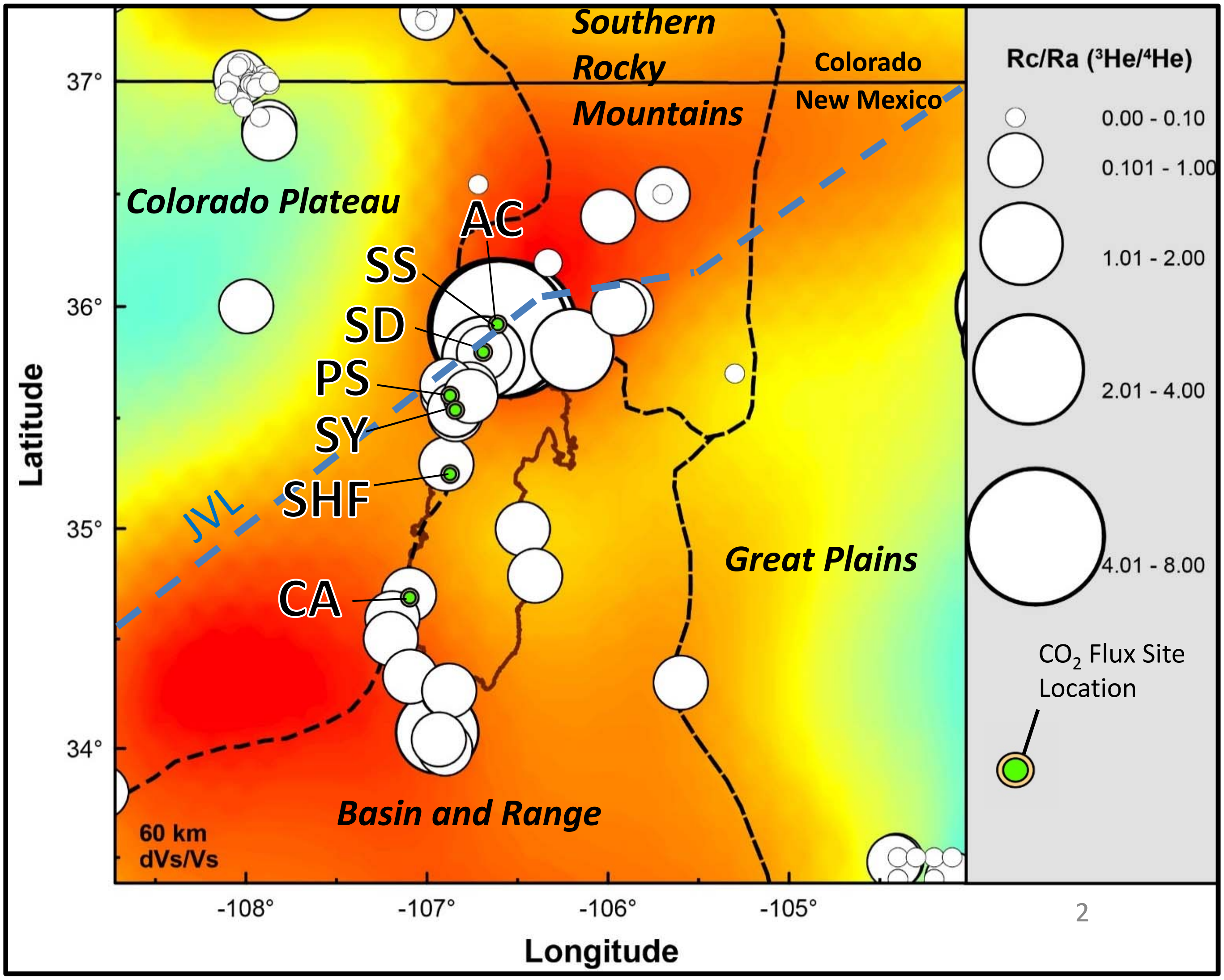
Southern
Rocky
Mountains
Colorado
New Mexico
Colorado Plateau
AC
SS
SD
PS
SY
SHF
JVL
CA
Great Plains
Basin and Range
60 km
dVs/Vs
37°
36°
35°
34°
-108°
-107°
-106°
-105°
Latitude
Longitude
Rc/Ra ($^3He/^4He$)
0.00 - 0.10
0.101 - 1.00
1.01 - 2.00
2.01 - 4.00
4.01 - 8.00
CO_2 Flux Site Location
2

Figure 3

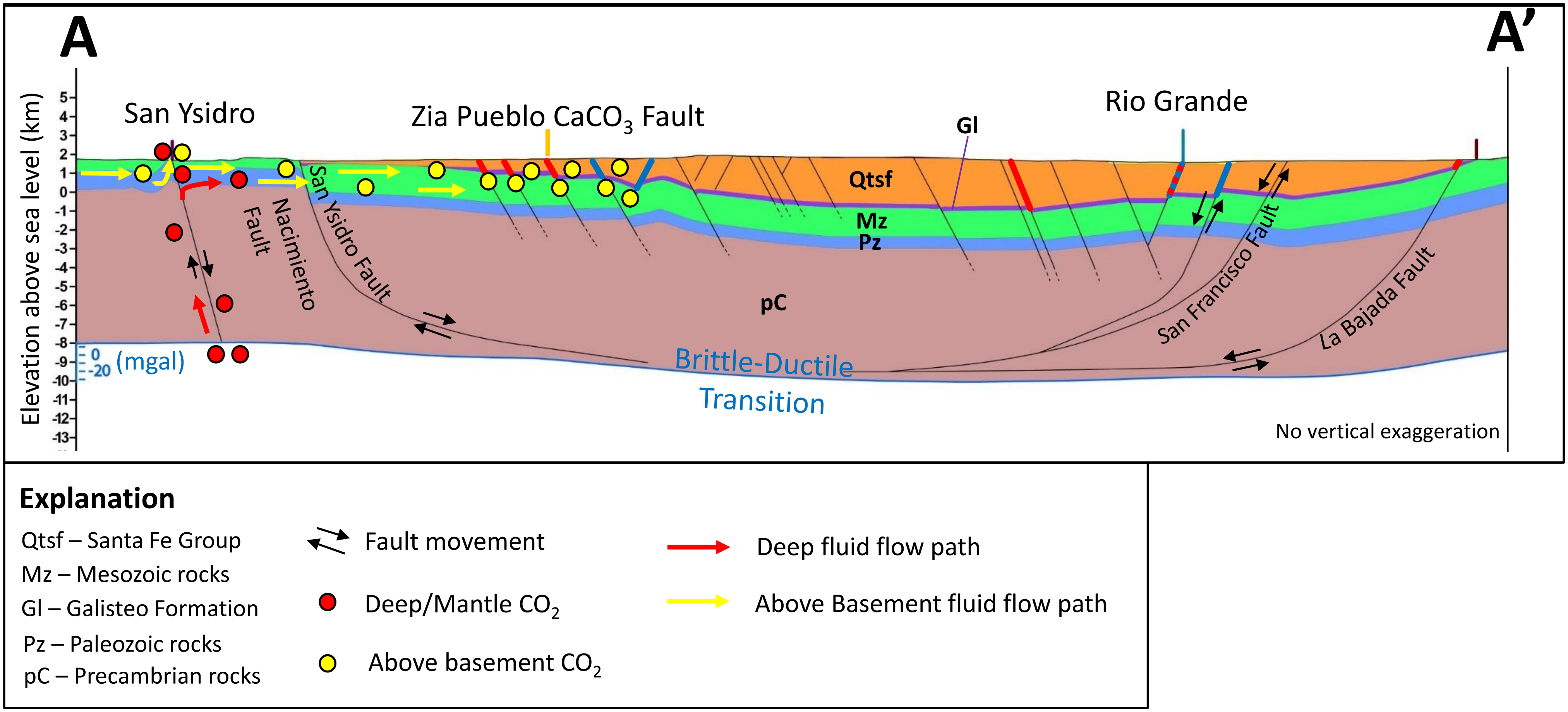
A
A’
Elevation above sea level (km)
5
4
3
2
1
0
-1
-2
-3
-4
-5
-6
-7
-8
-9
-10
-11
-12
-13
0
-20
(mgal)
San Ysidro
Zia Pueblo $CaCO_3$ Fault
GI
Rio Grande
Qtsf
Mz
Pz
pC
Nacimiento Fault
San Ysidro Fault
San Francisco Fault
La Bajada Fault
Brittle-Ductile Transition
No vertical exaggeration
Explanation
Qtsf – Santa Fe Group
Mz – Mesozoic rocks
Gl – Galisteo Formation
Pz – Paleozoic rocks
pC – Precambrian rocks
Fault movement
Deep/Mantle CO_2
Above basement CO_2
Deep fluid flow path
Above Basement fluid flow path

Figure 4

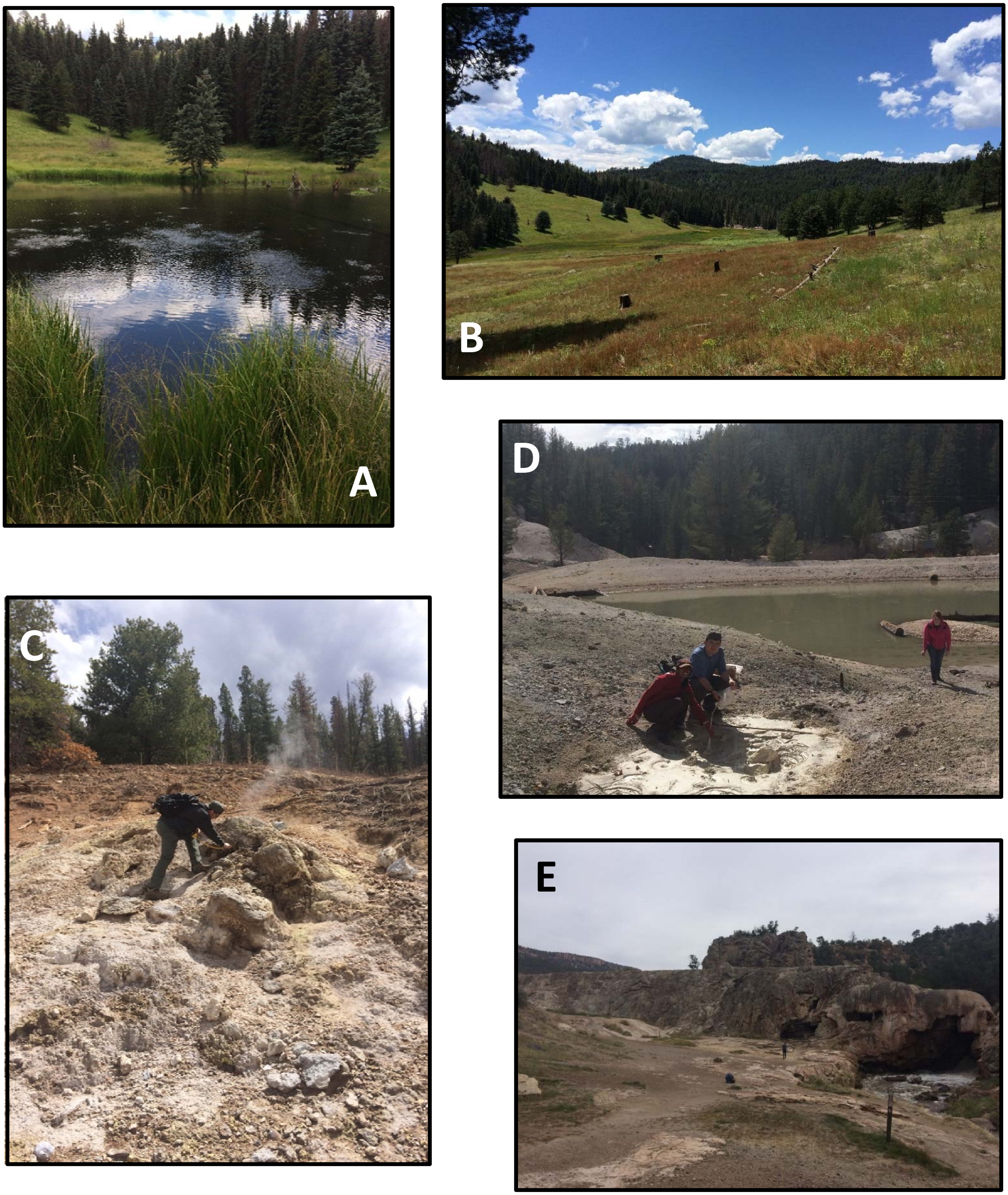

Figure 5

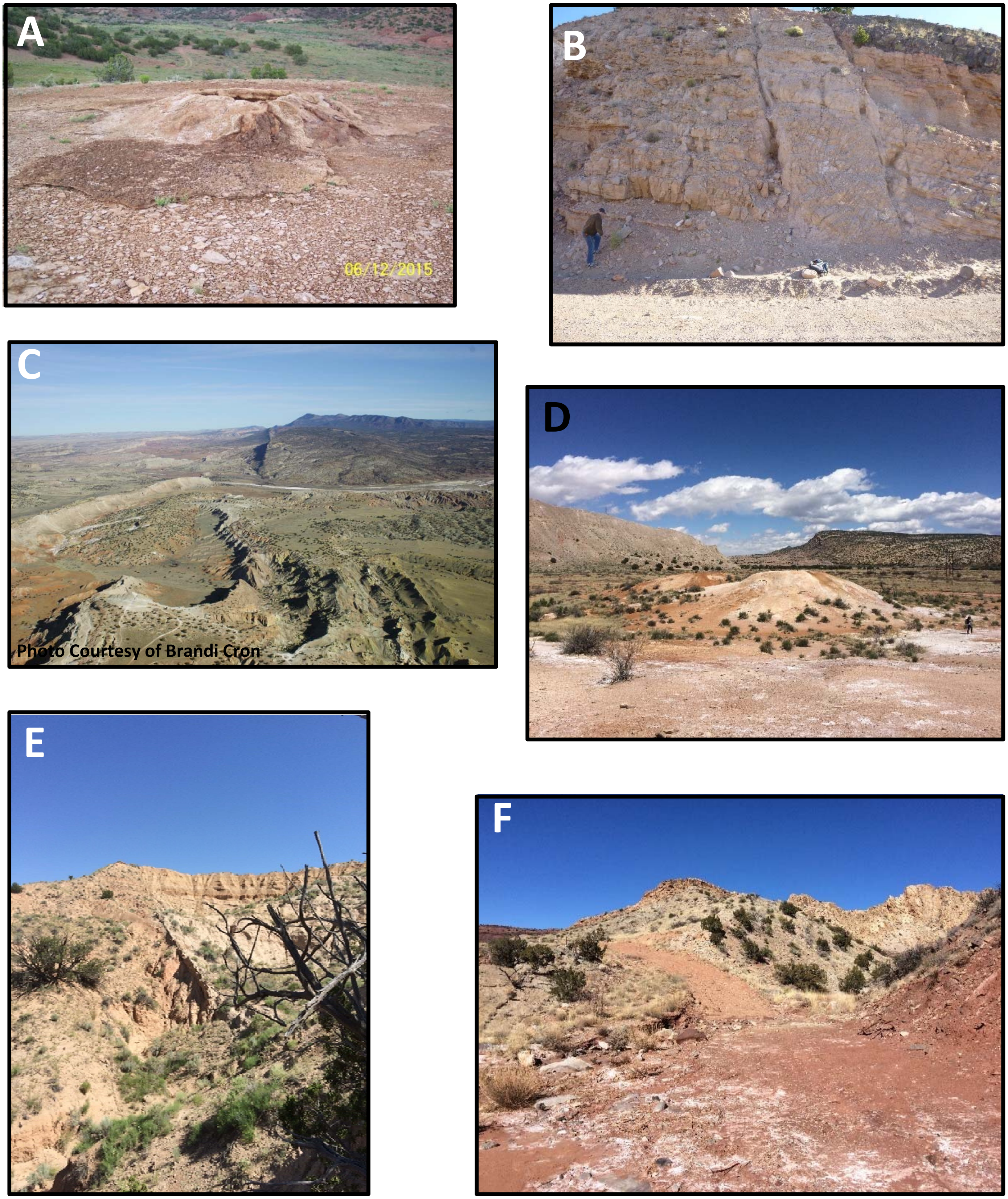

Figure 6

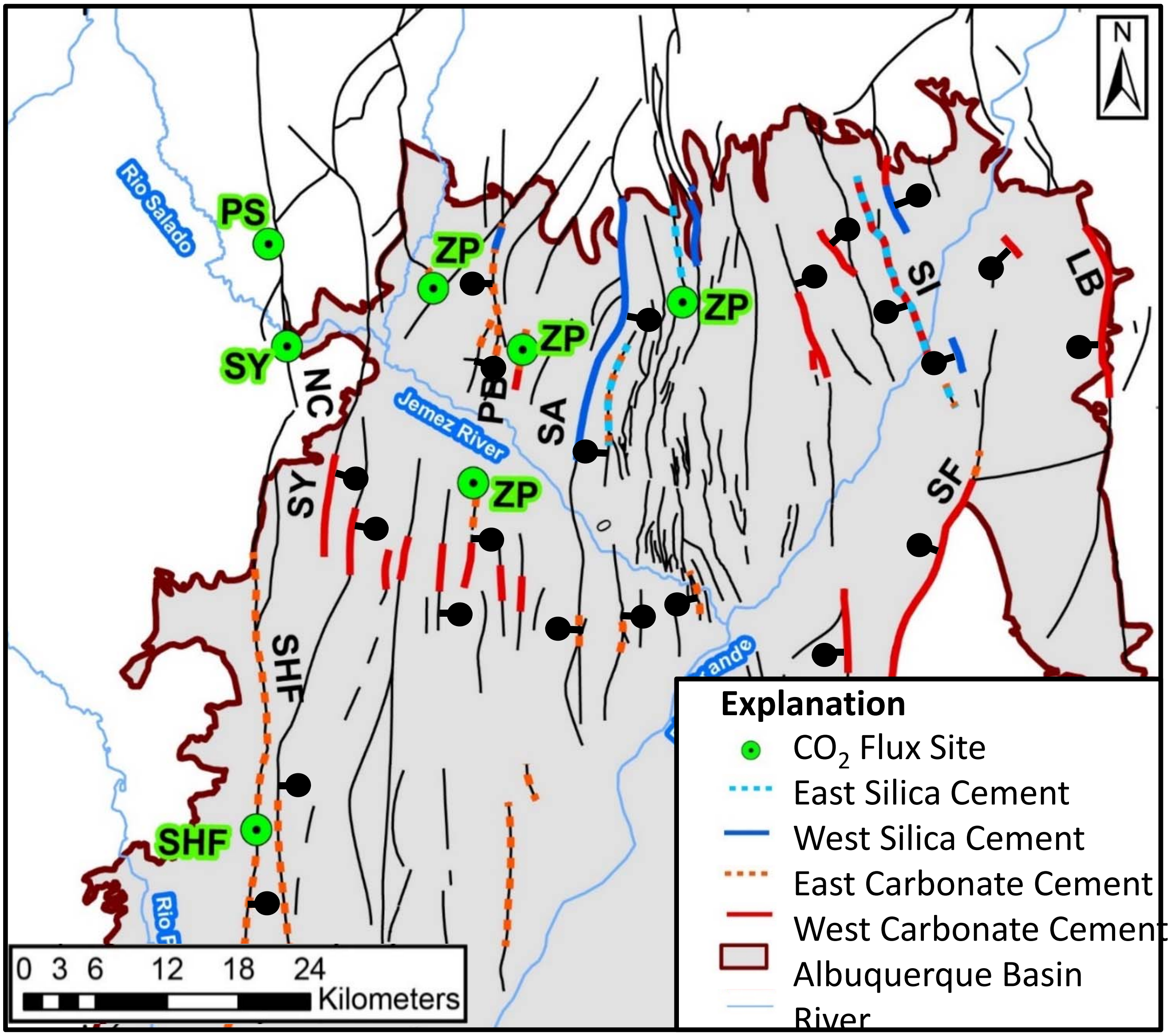
N
PS
SY
ZP
ZP
ZP
ZP
SHF
Rio Salado
Jemez River
Rio Grande
Rio P
NC
PB
SA
SY
SHF
SI
LB
SF
Explanation
CO2 Flux Site
East Silica Cement
West Silica Cement
East Carbonate Cement
West Carbonate Cement
Albuquerque Basin
River
0 3 6 12 18 24
Kilometers

Figure 7

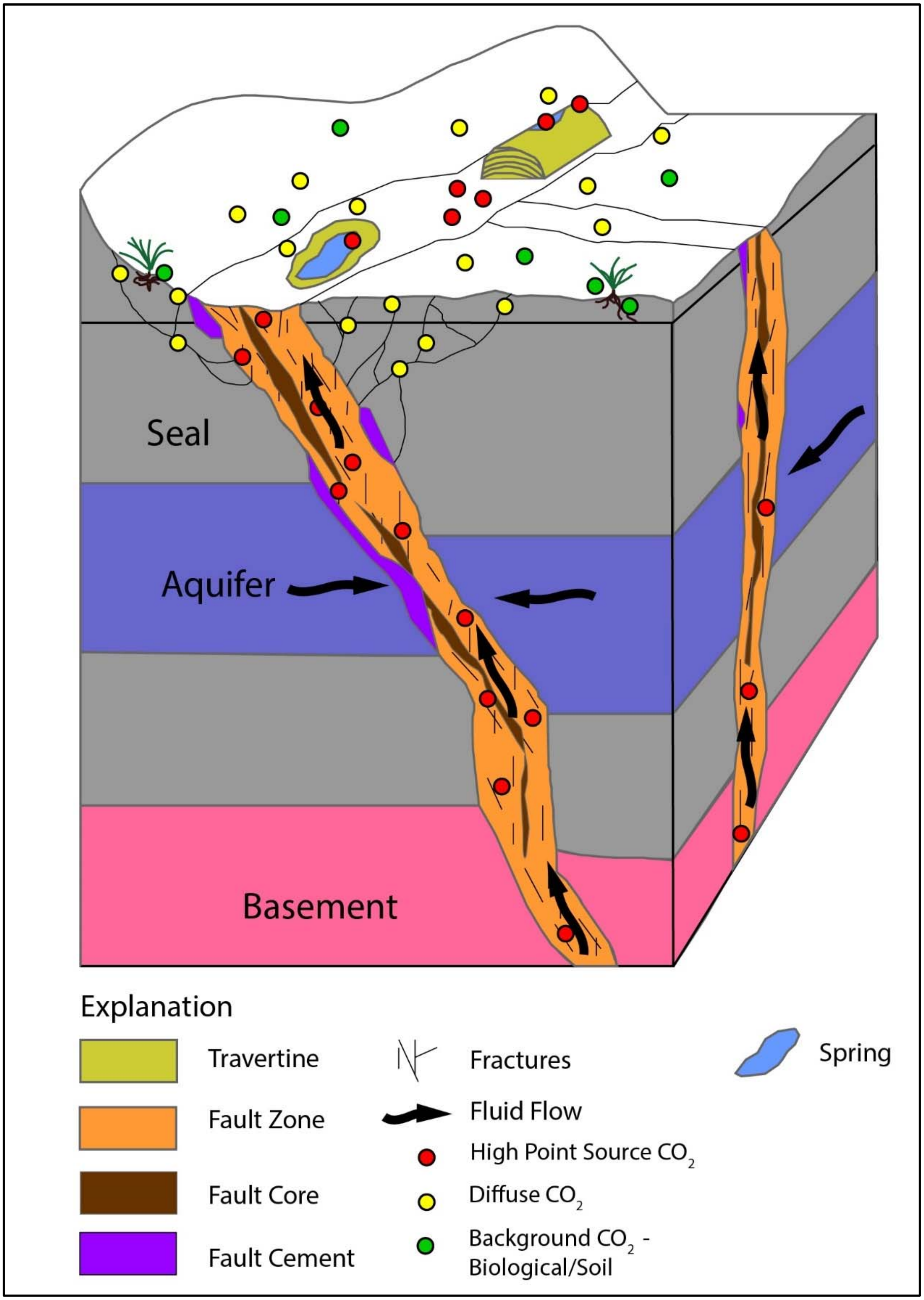
Seal
Aquifer
Basement
Explanation
Travertine
Fault Zone
Fault Core
Fault Cement
Fractures
Fluid Flow
High Point Source CO_2
Diffuse CO_2
Background CO_2 - Biological/Soil
Spring

Figure 8

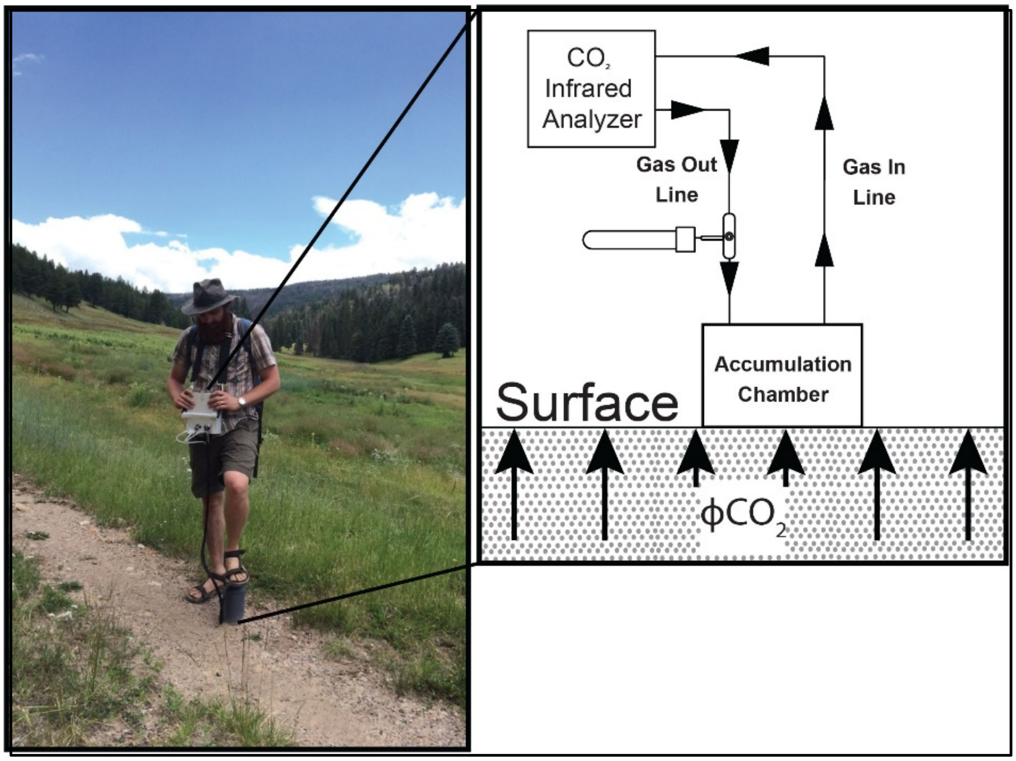
CO_2 Infrared Analyzer
Gas Out Line
Gas In Line
Accumulation Chamber
Surface
ϕCO_2

Figure 9

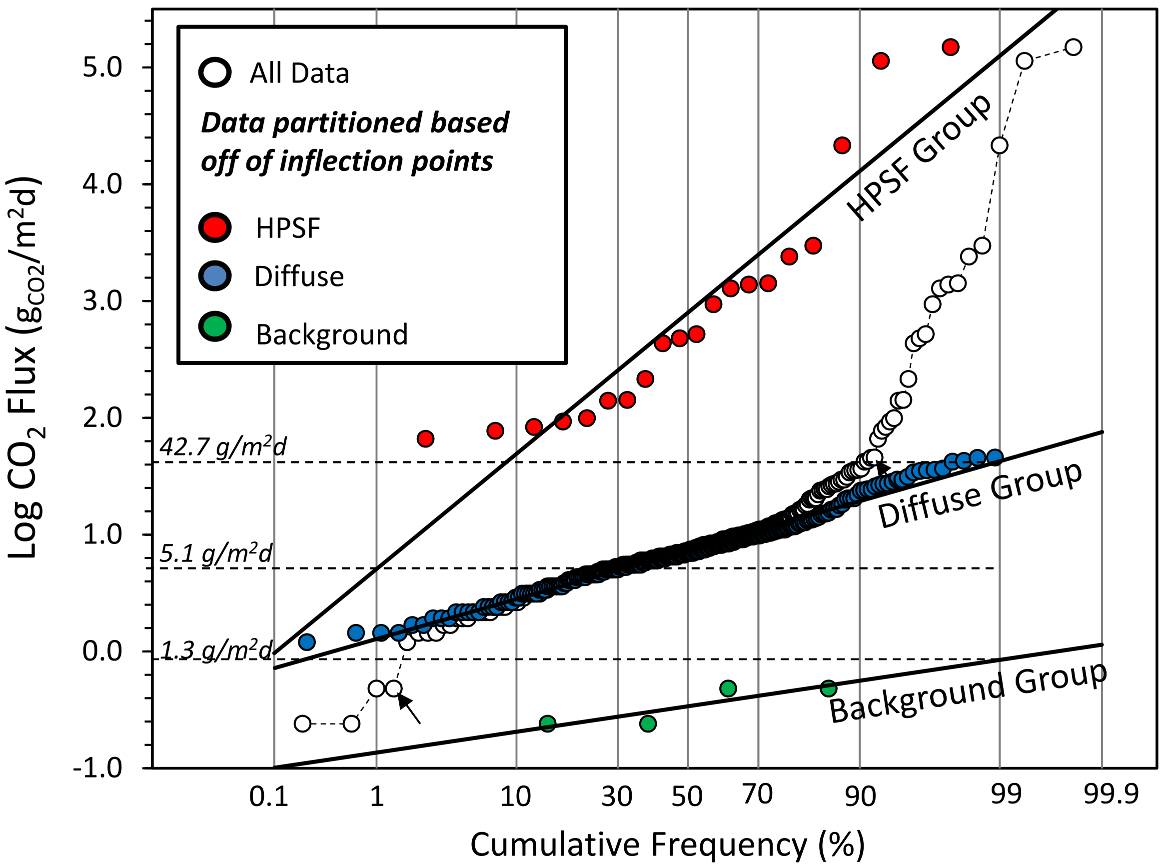

○ All Data
Data partitioned based off of inflection points
● HPSF
● Diffuse
● Background
HPSF Group
Diffuse Group
Background Group
42.7 g/m²d
5.1 g/m²d
1.3 g/m²d
Log CO$_2$ Flux (g$_{CO2}$/m^{2}d)
5.0
4.0
3.0
2.0
1.0
0.0
-1.0
0.1
1
10
30
50
70
90
99
99.9
Cumulative Frequency (%)

Figure 10

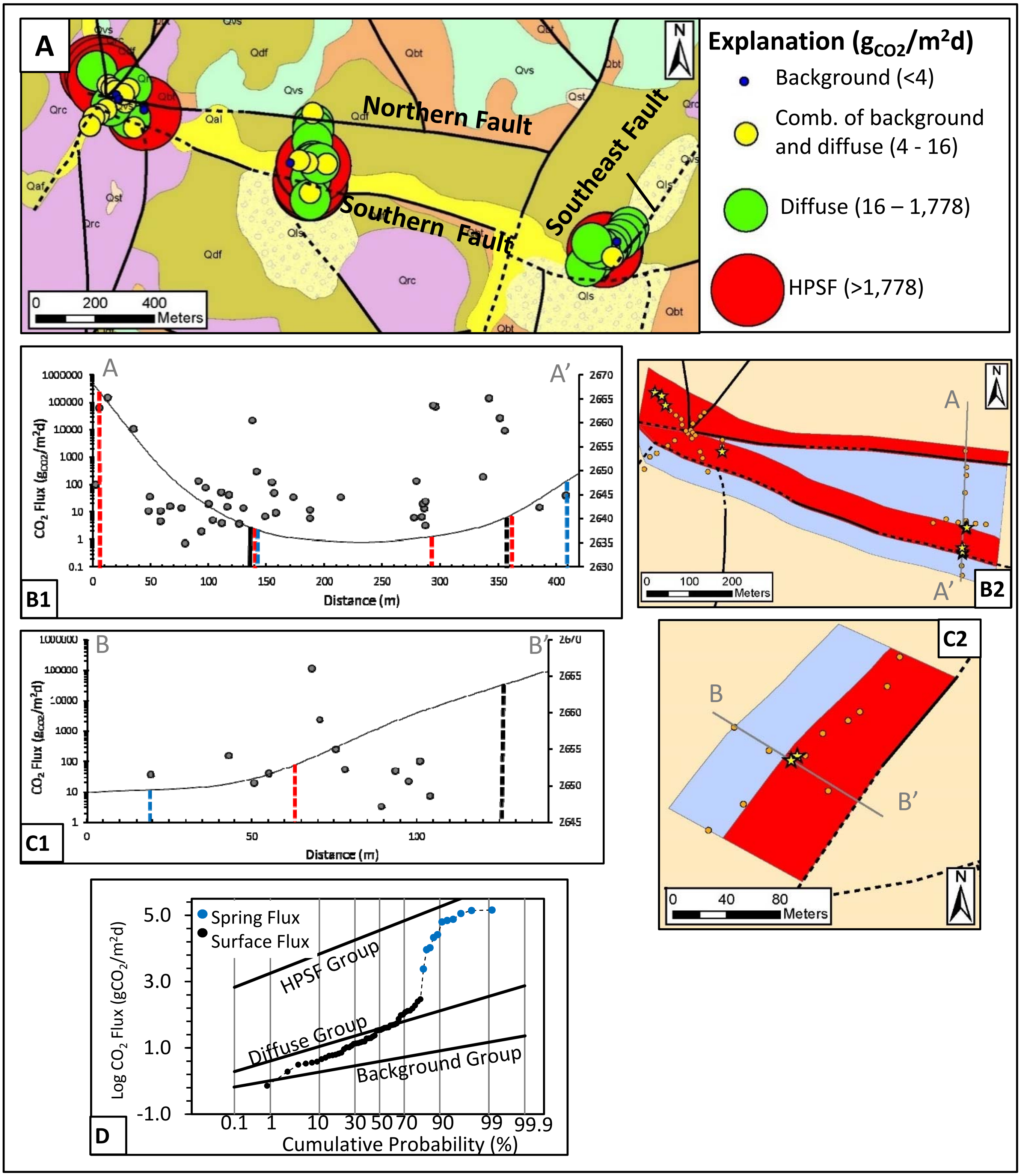
A
Explanation (g_{CO2}/m^2d)
Background (<4)
Comb. of background and diffuse (4 - 16)
Diffuse (16 – 1,778)
HPSF (>1,778)
Northern Fault
Southern Fault
Southeast Fault
Qvs
Qdf
Qbt
Qst
Qrc
Qal
Qaf
Qls
N
0 200 400 Meters
B1
A
A'
CO2 Flux (g_{CO2}/m^2d)
Distance (m)
1000000
100000
10000
1000
100
10
1
0.1
0
50
100
150
200
250
300
350
400
2670
2665
2660
2655
2650
2645
2640
2635
2630
B2
A
A'
0 100 200 Meters
C1
B
B'
CO2 Flux (g_{CO2}/m^2d)
Distance (m)
1000000
100000
10000
1000
100
10
1
0
50
100
2670
2665
2660
2655
2650
2645
C2
B
B'
0 40 80 Meters
D
Spring Flux
Surface Flux
HPSF Group
Diffuse Group
Background Group
Log CO2 Flux (gCO_2/m^2d)
5.0
3.0
1.0
-1.0
0.1
1
10
30
50
70
90
99
99.9
Cumulative Probability (%)

Figure 11

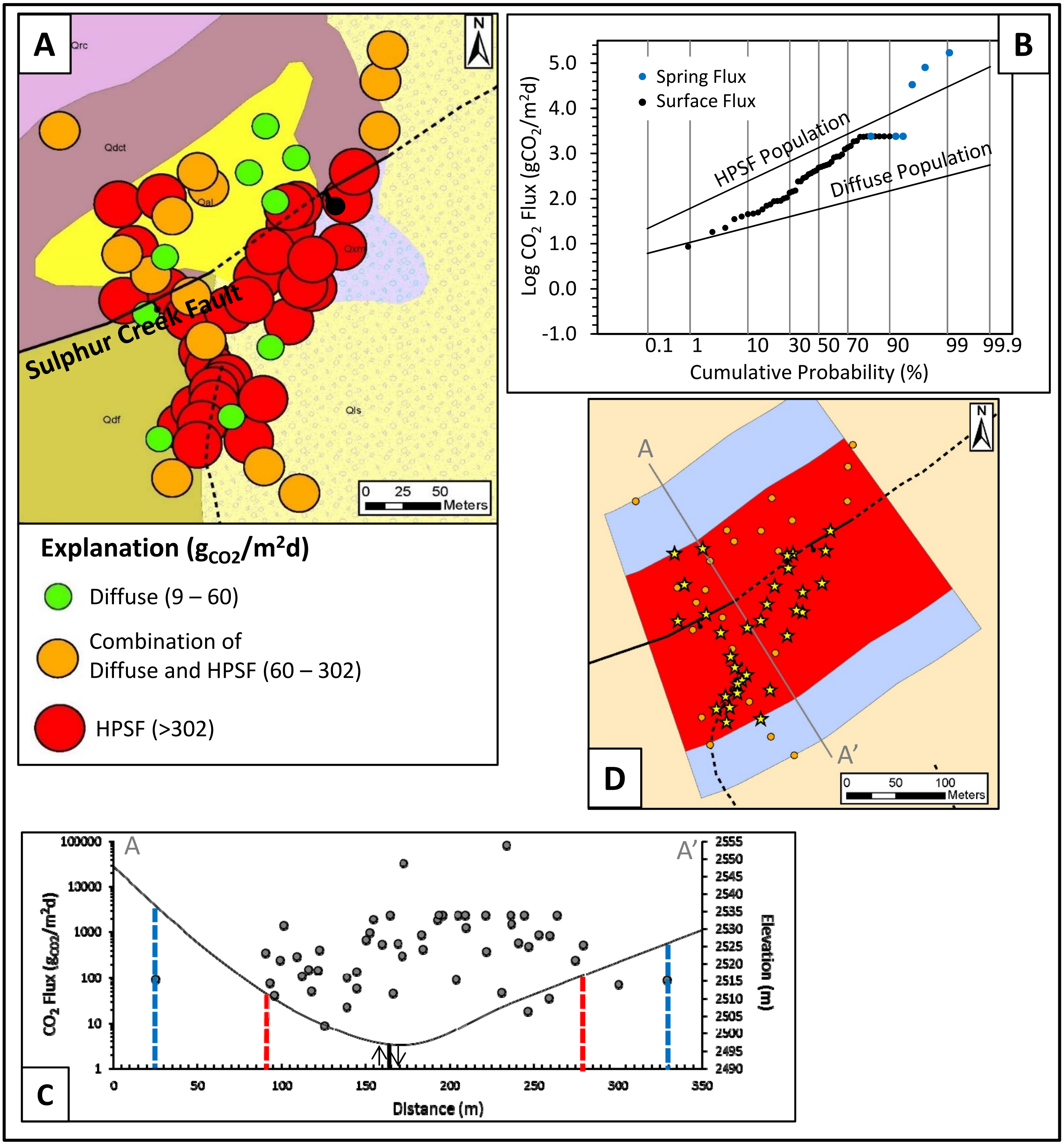
A
Qrc
Qdct
Qal
Qxm
Qdf
Qls
Sulphur Creek Fault
N
0 25 50
Meters
Explanation (g_{CO2}/m^2d)
Diffuse (9 – 60)
Combination of Diffuse and HPSF (60 – 302)
HPSF (>302)
B
Spring Flux
Surface Flux
HPSF Population
Diffuse Population
Log CO$_2$ Flux (gCO$_2$/m^{2}d)
5.0
4.0
3.0
2.0
1.0
0.0
-1.0
0.1
1
10
30
50
70
90
99
99.9
Cumulative Probability (%)
D
A
A'
N
0 50 100
Meters
C
A
A'
CO$_2$ Flux (g_{CO2}/m^2d)
100000
10000
1000
100
10
1
Elevation (m)
2555
2550
2545
2540
2535
2530
2525
2520
2515
2510
2505
2500
2495
2490
0
50
100
150
200
250
300
350
Distance (m)

Figure 12

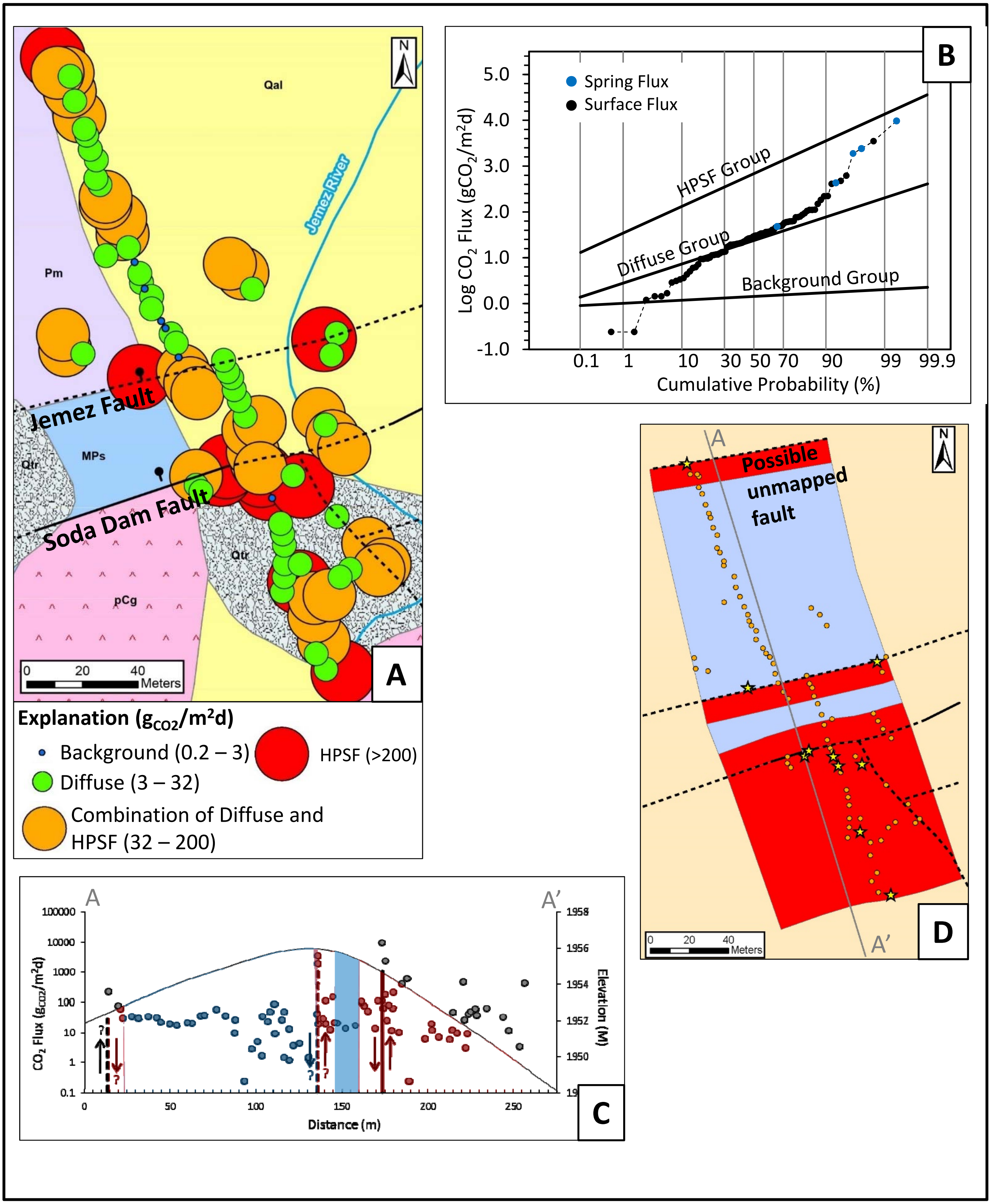
A
Qal
Pm
MPs
Qtr
pCg
Jemez River
Jemez Fault
Soda Dam Fault
N
0 20 40 Meters
Explanation (g_{CO2}/m^2d)
Background (0.2 – 3)
Diffuse (3 – 32)
HPSF (>200)
Combination of Diffuse and HPSF (32 – 200)
B
Spring Flux
Surface Flux
HPSF Group
Diffuse Group
Background Group
Log CO2 Flux (gCO2/m2d)
5.0
4.0
3.0
2.0
1.0
0.0
-1.0
0.1
1
10
30
50
70
90
99
99.9
Cumulative Probability (%)
D
A
A'
N
Possible unmapped fault
0 20 40 Meters
C
A
A'
CO2 Flux (gCO2/m2d)
100000
10000
1000
100
10
1
0.1
Elevation (M)
1958
1956
1954
1952
1950
19
?
0
50
100
150
200
250
Distance (m)

Figure 13

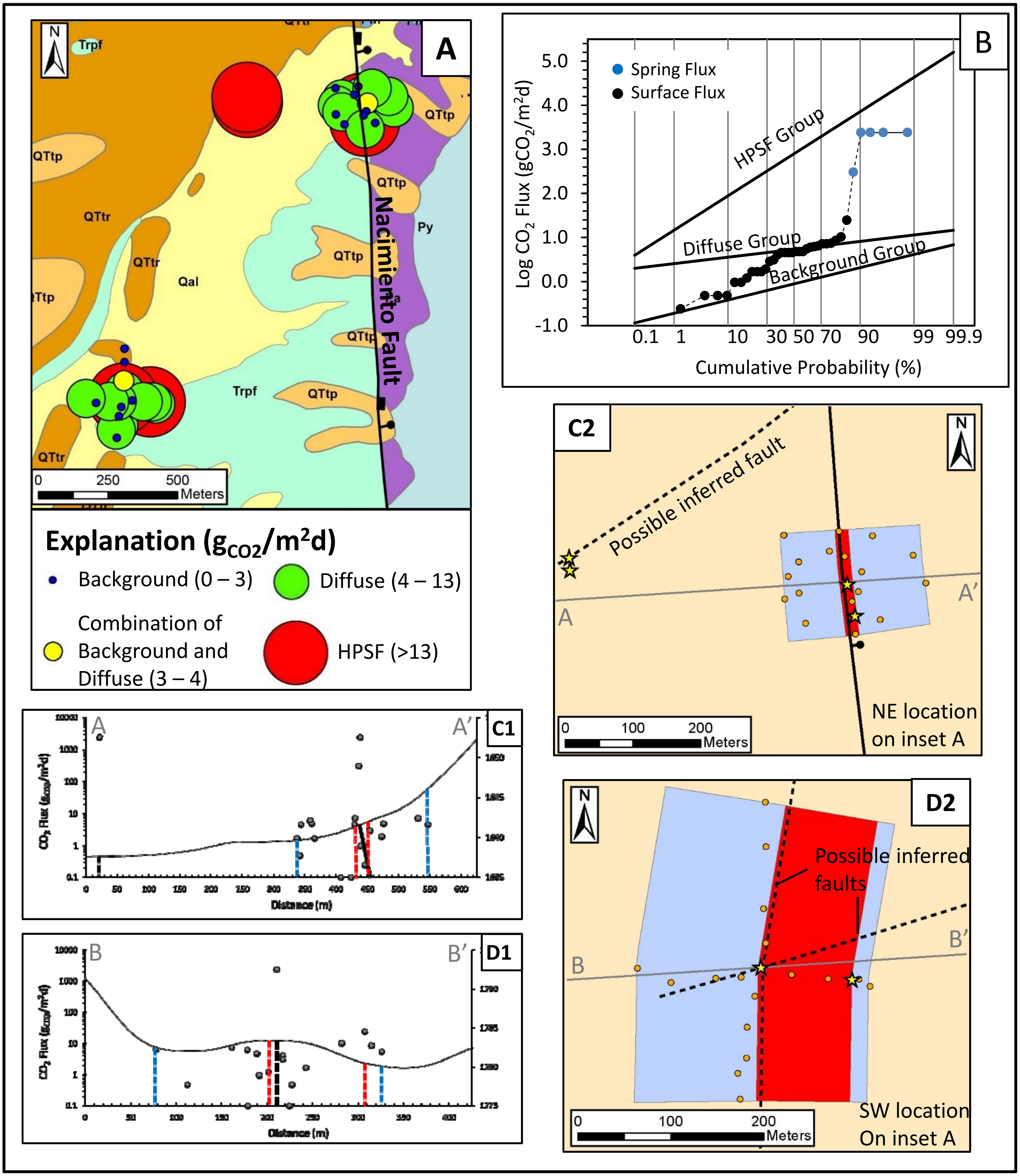
A
N
Trpf
QTtp
QTtr
Qal
Py
Nacimiento Fault
0 250 500 Meters
Explanation (g_{CO2}/m^2d)
Background (0 – 3)
Diffuse (4 – 13)
Combination of Background and Diffuse (3 – 4)
HPSF (>13)
B
Spring Flux
Surface Flux
HPSF Group
Diffuse Group
Background Group
Log CO_2 Flux (gCO_2/m^2d)
5.0
4.0
3.0
2.0
1.0
0.0
-1.0
0.1 1 10 30 50 70 90 99 99.9
Cumulative Probability (%)
C2
N
Possible inferred fault
A
A′
0 100 200 Meters
NE location on inset A
C1
A
A′
CO_2 Flux (g_{CO2}/m^2d)
Distance (m)
D1
B
B′
CO_2 Flux (g_{CO2}/m^2d)
Distance (m)
D2
N
Possible inferred faults
B
B′
0 100 200 Meters
SW location On inset A

Figure 14

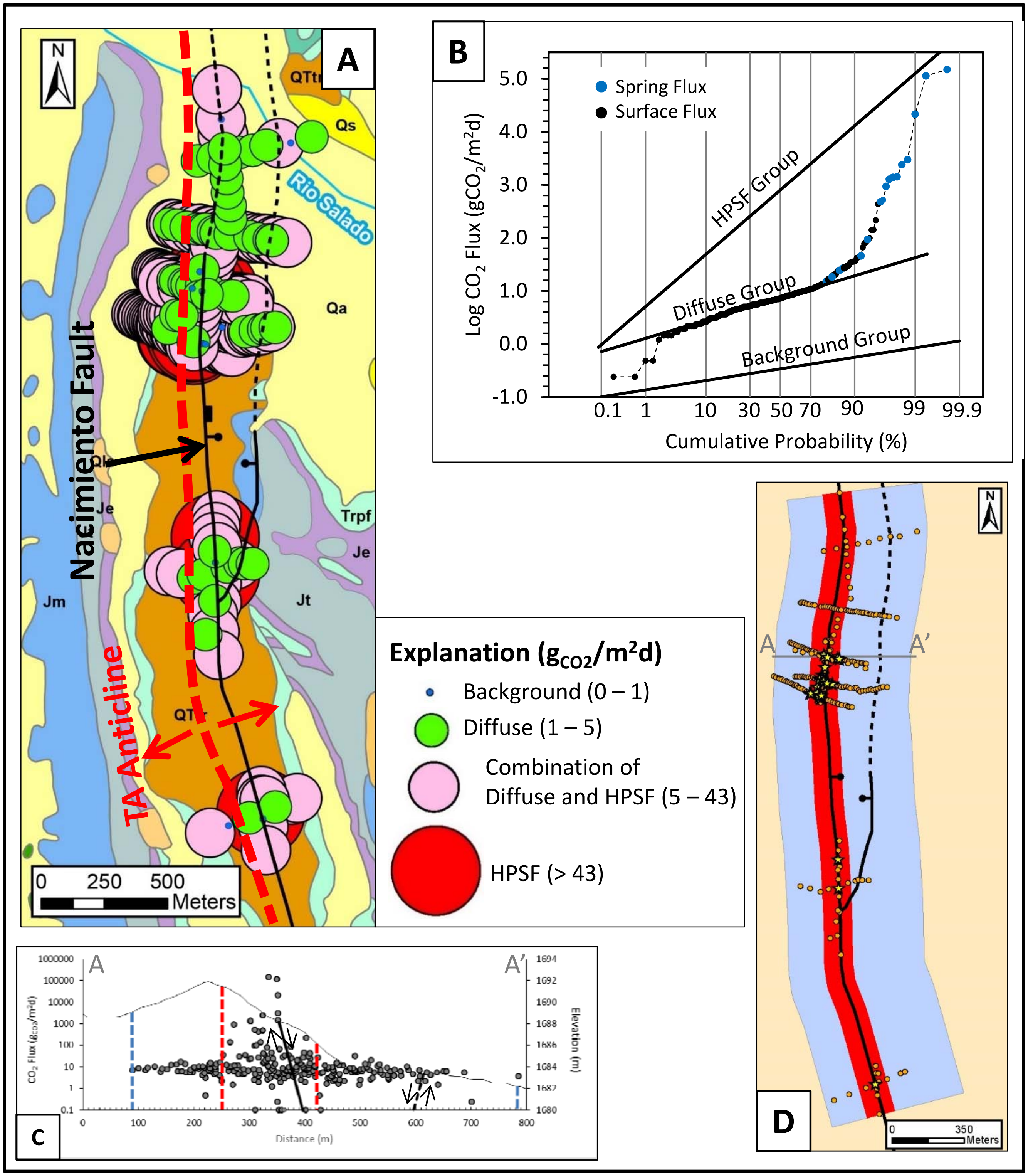
A
N
QTt
Qs
Rio Salado
Qa
Nacimiento Fault
Ql
Je
Trpf
Je
Jm
Jt
QT
TA Anticline
0 250 500 Meters
B
5.0
4.0
3.0
2.0
1.0
0.0
-1.0
Log CO2 Flux (gCO2/m2d)
Spring Flux
Surface Flux
HPSF Group
Diffuse Group
Background Group
0.1 1 10 30 50 70 90 99 99.9
Cumulative Probability (%)
Explanation (gCO2/m2d)
Background (0 – 1)
Diffuse (1 – 5)
Combination of Diffuse and HPSF (5 – 43)
HPSF (> 43)
C
A
A'
1000000
100000
10000
1000
100
10
1
0.1
CO2 Flux (gCO2/m2d)
1694
1692
1690
1688
1686
1684
1682
1680
Elevation (m)
0 100 200 300 400 500 600 700 800
Distance (m)
D
N
A
A'
0 350 Meters

Figure 15

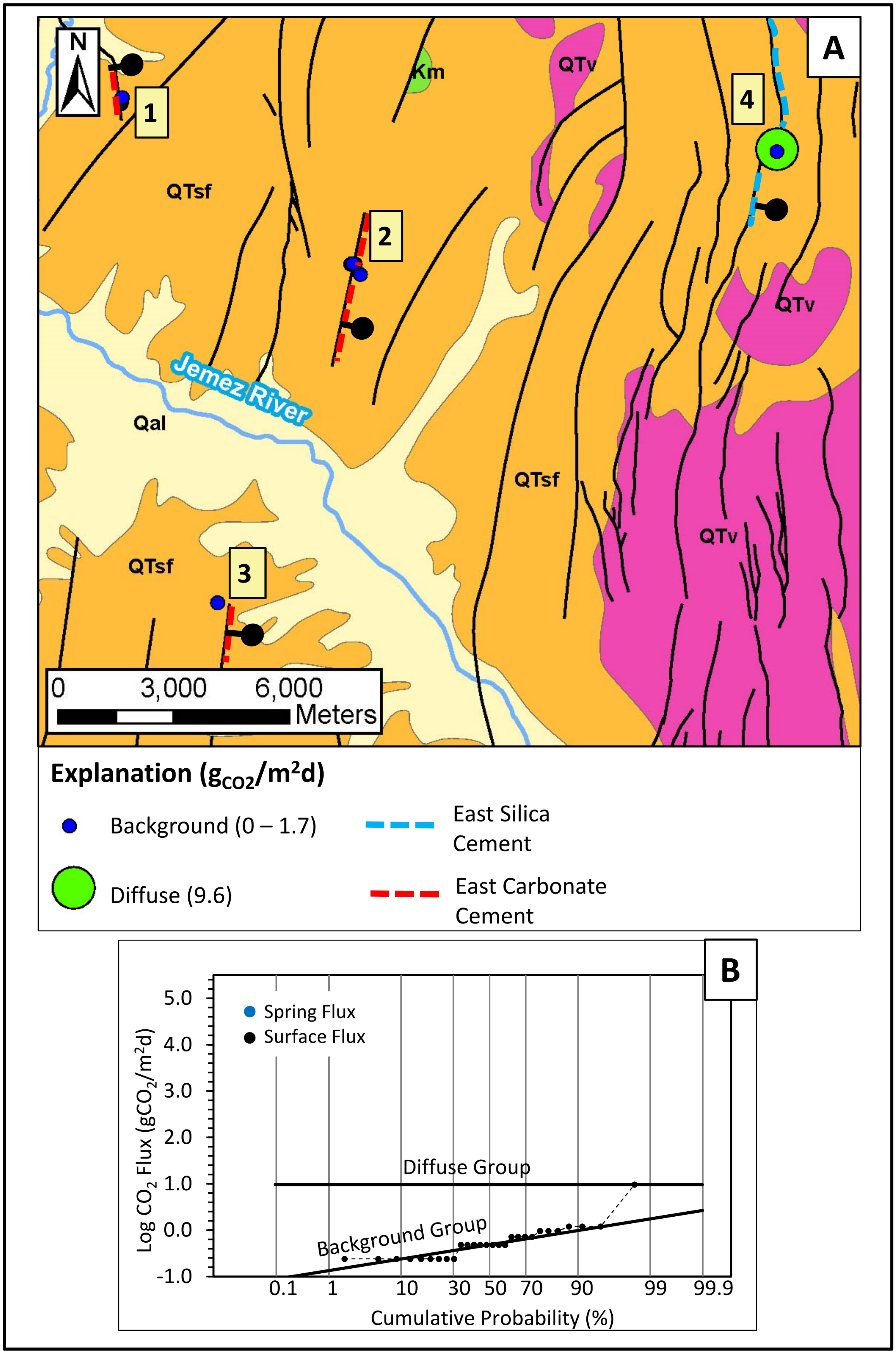
A
N
1
2
3
4
Km
QTv
QTsf
Qal
Jemez River
QTsf
QTsf
QTv
QTv
0 3,000 6,000 Meters
Explanation (g_{CO2}/m^2d)
● Background (0 – 1.7)
● Diffuse (9.6)
East Silica Cement
East Carbonate Cement
B
Spring Flux
Surface Flux
Log CO_2 Flux (gCO_2/m^2d)
5.0
4.0
3.0
2.0
1.0
0.0
-1.0
Diffuse Group
Background Group
0.1
1
10
30
50
70
90
99
99.9
Cumulative Probability (%)

Figure 16

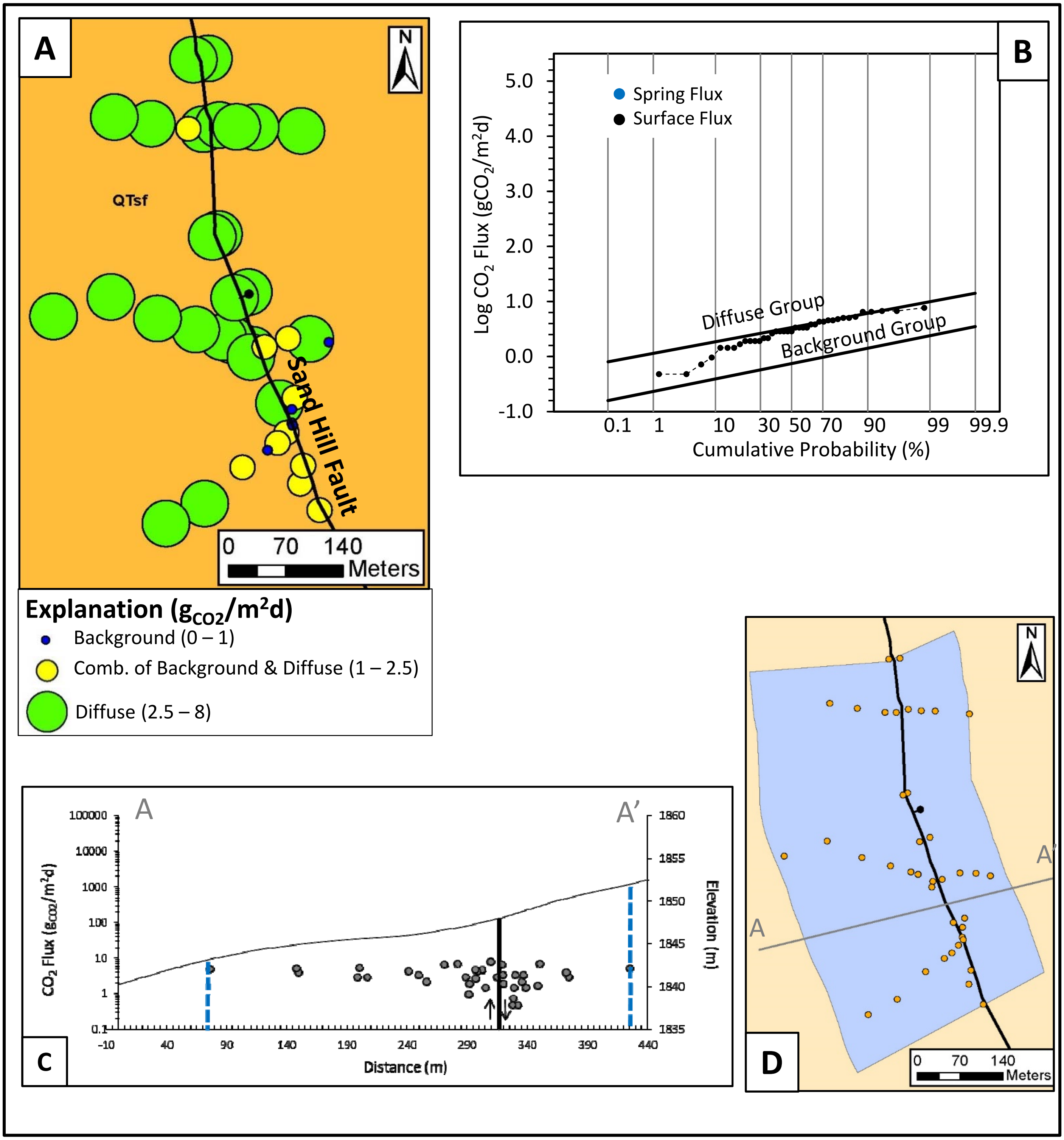
A
N
QTsf
Sand Hill Fault
0 70 140
Meters
Explanation (g_{CO2}/m^2d)
Background (0 – 1)
Comb. of Background & Diffuse (1 – 2.5)
Diffuse (2.5 – 8)
B
Spring Flux
Surface Flux
Log CO_2 Flux (gCO_2/m^2d)
5.0
4.0
3.0
2.0
1.0
0.0
-1.0
Diffuse Group
Background Group
0.1 1 10 30 50 70 90 99 99.9
Cumulative Probability (%)
C
A
A'
CO_2 Flux (g_{CO2}/m^2d)
100000
10000
1000
100
10
1
0.1
-10 40 90 140 190 240 290 340 390 440
Distance (m)
1860
1855
1850
1845
1840
1835
Elevation (m)
D
N
A
A'
0 70 140
Meters

Figure 17

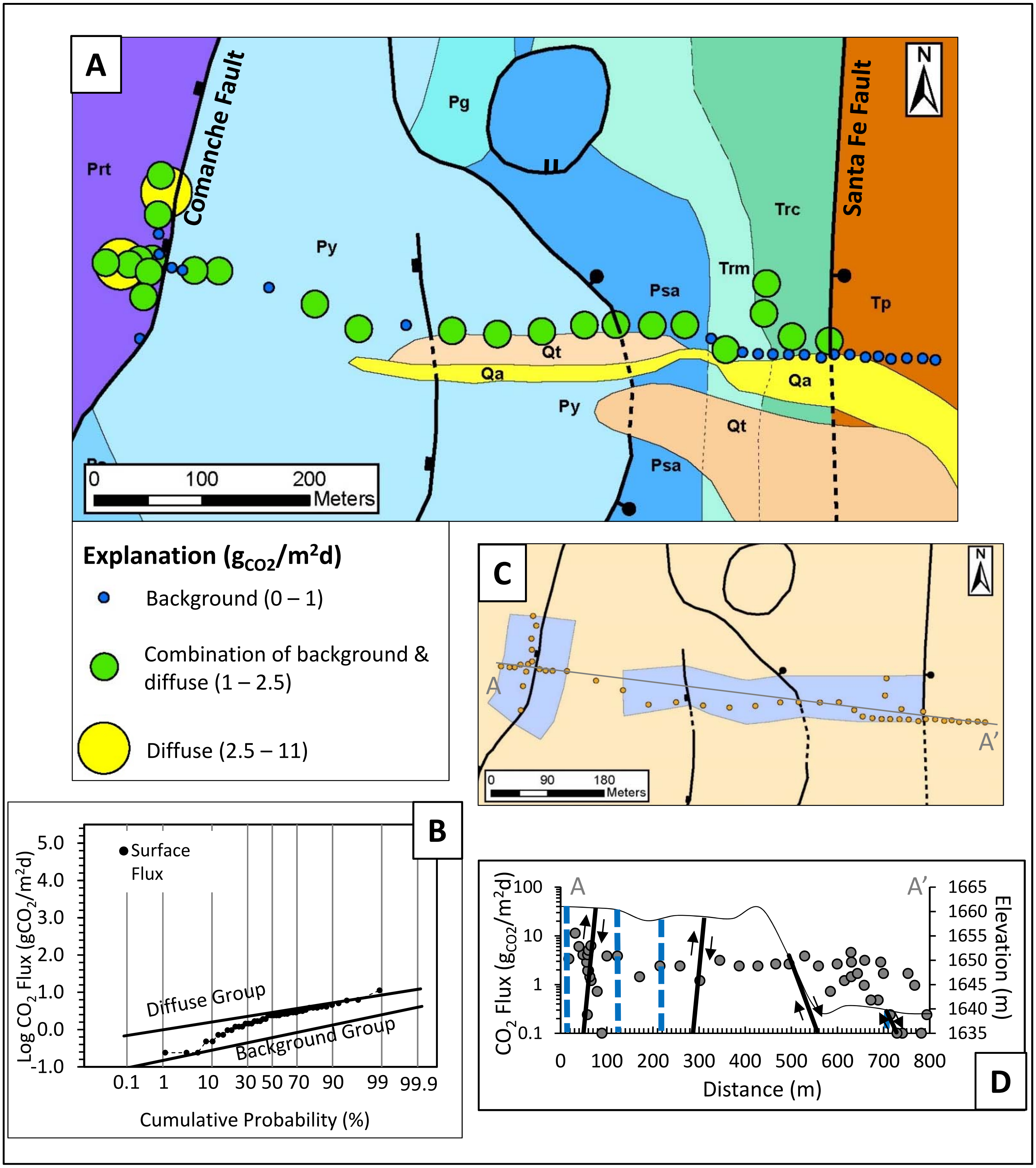
A
Comanche Fault
Santa Fe Fault
N
Prt
Pg
Py
Psa
Trc
Trm
Tp
Qt
Qa
0
100
200
Meters
Explanation (g_{CO2}/m^2d)
Background (0 – 1)
Combination of background & diffuse (1 – 2.5)
Diffuse (2.5 – 11)
C
A
A'
0
90
180
Meters
B
Surface Flux
Diffuse Group
Background Group
Log CO_2 Flux (gCO_2/m^2d)
5.0
4.0
3.0
2.0
1.0
0.0
-1.0
0.1
1
10
30
50
70
90
99
99.9
Cumulative Probability (%)
D
A
A'
CO_2 Flux (g_{CO2}/m^2d)
100
10
1
0.1
Elevation (m)
1665
1660
1655
1650
1645
1640
1635
0
100
200
300
400
500
600
700
800
Distance (m)

Figure 18

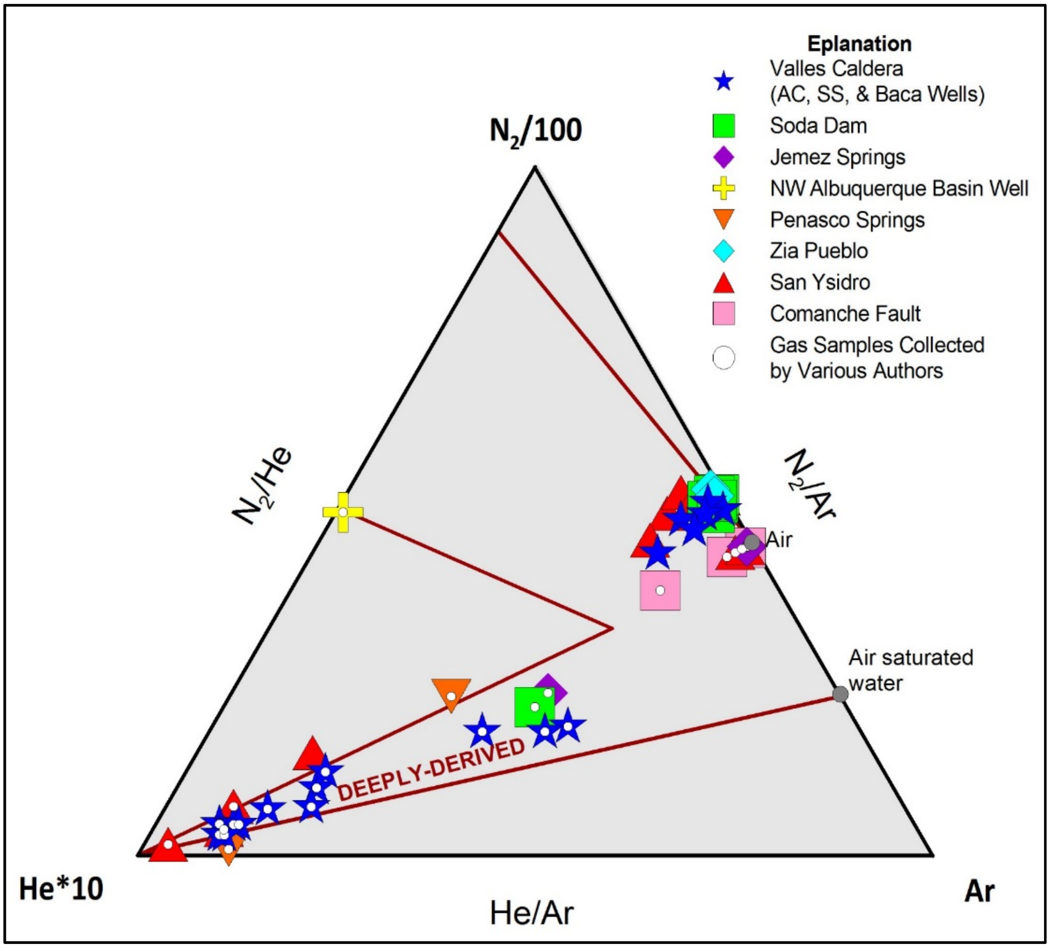
Eplanation
★ Valles Caldera
(AC, SS, & Baca Wells)
🟩 Soda Dam
◆ Jemez Springs
✚ NW Albuquerque Basin Well
▼ Penasco Springs
◆ Zia Pueblo
▲ San Ysidro
■ Comanche Fault
○ Gas Samples Collected
by Various Authors
$N_2/100$
N_2/He
N_2/Ar
Air
Air saturated
water
DEEPLY-DERIVED
He*10
He/Ar
Ar

Figure 19

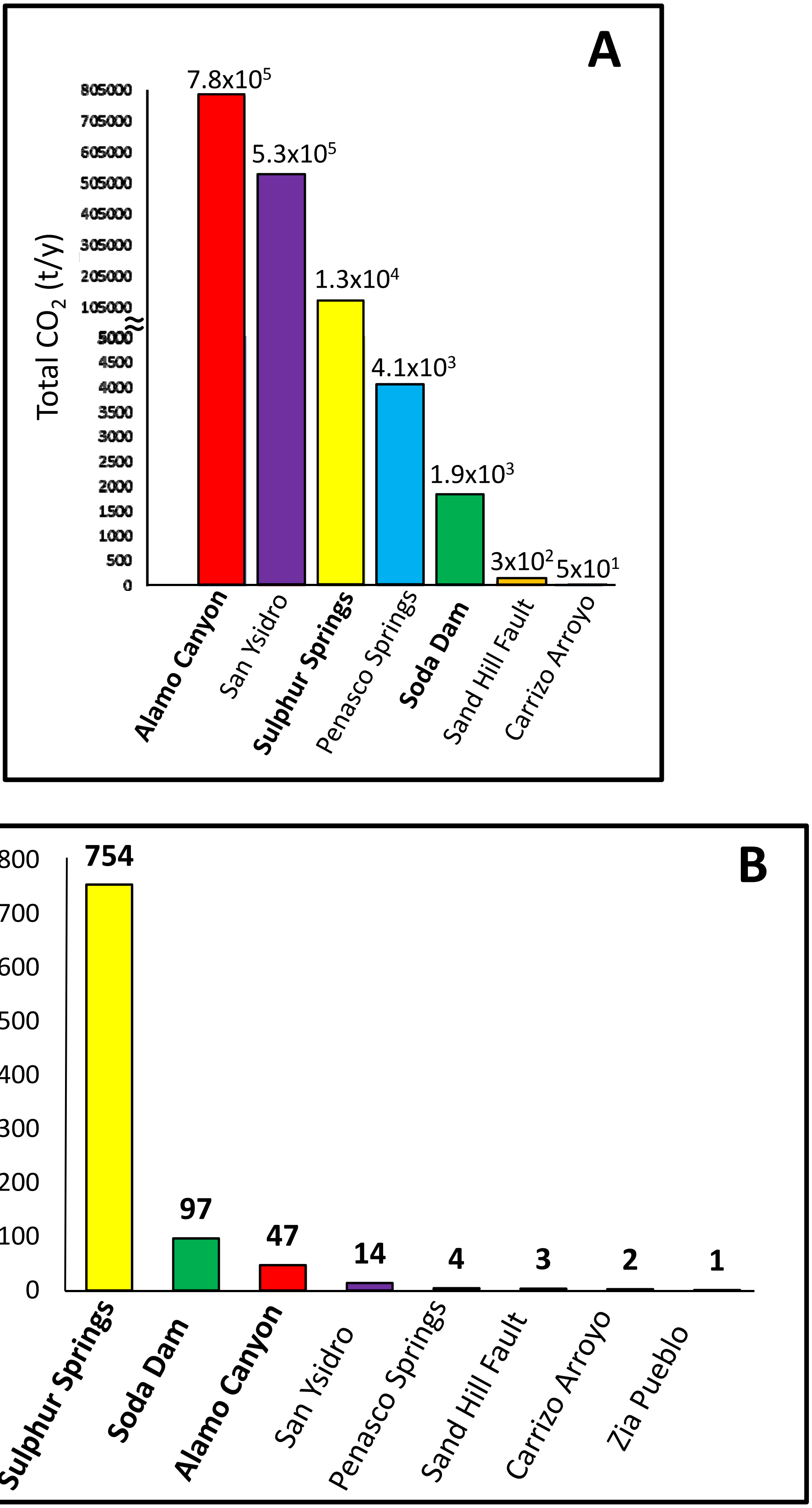
A
Total CO2 (t/y)
805000
705000
605000
505000
405000
305000
205000
105000
5000
4500
4000
3500
3000
2500
2000
1500
1000
500
0
7.8x10^5
5.3x10^5
1.3x10^4
4.1x10^3
1.9x10^3
3x10^2
5x10^1
Alamo Canyon
San Ysidro
Sulphur Springs
Penasco Springs
Soda Dam
Sand Hill Fault
Carrizo Arroyo
B
Average Surface CO2 Flux (g/m2d)
800
700
600
500
400
300
200
100
0
754
97
47
14
4
3
2
1
Sulphur Springs
Soda Dam
Alamo Canyon
San Ysidro
Penasco Springs
Sand Hill Fault
Carrizo Arroyo
Zia Pueblo

Figure 20

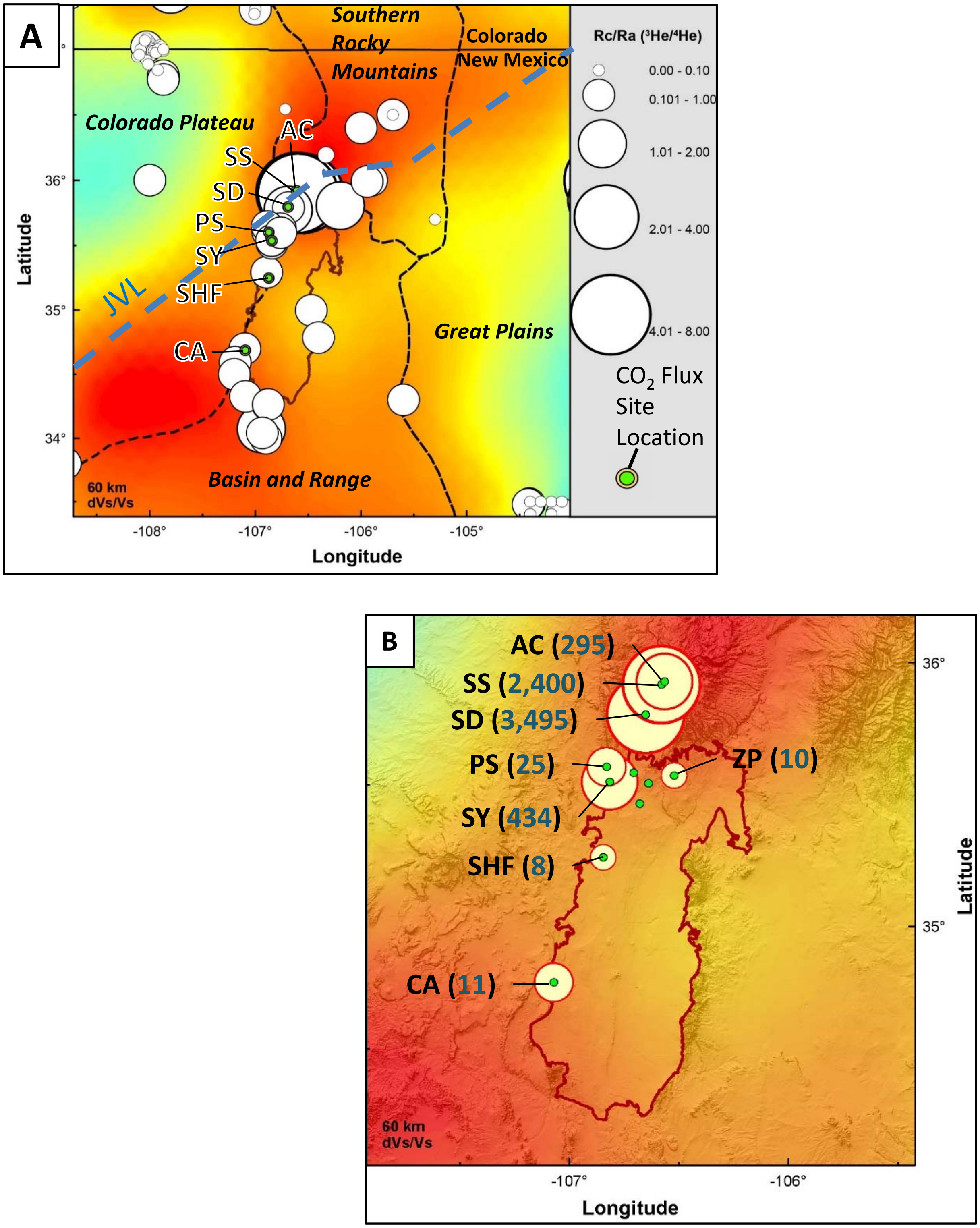
A
Southern Rocky Mountains
Colorado
New Mexico
Colorado Plateau
AC
SS
SD
PS
SY
SHF
JVL
CA
Great Plains
Basin and Range
60 km
dVs/Vs
Latitude
Longitude
36°
35°
34°
-108°
-107°
-106°
-105°
Rc/Ra (³He/⁴He)
0.00 - 0.10
0.101 - 1.00
1.01 - 2.00
2.01 - 4.00
4.01 - 8.00
CO₂ Flux Site Location
B
AC (295)
SS (2,400)
SD (3,495)
PS (25)
ZP (10)
SY (434)
SHF (8)
CA (11)
60 km
dVs/Vs
36°
35°
Latitude
-107°
-106°
Longitude

Figure 21

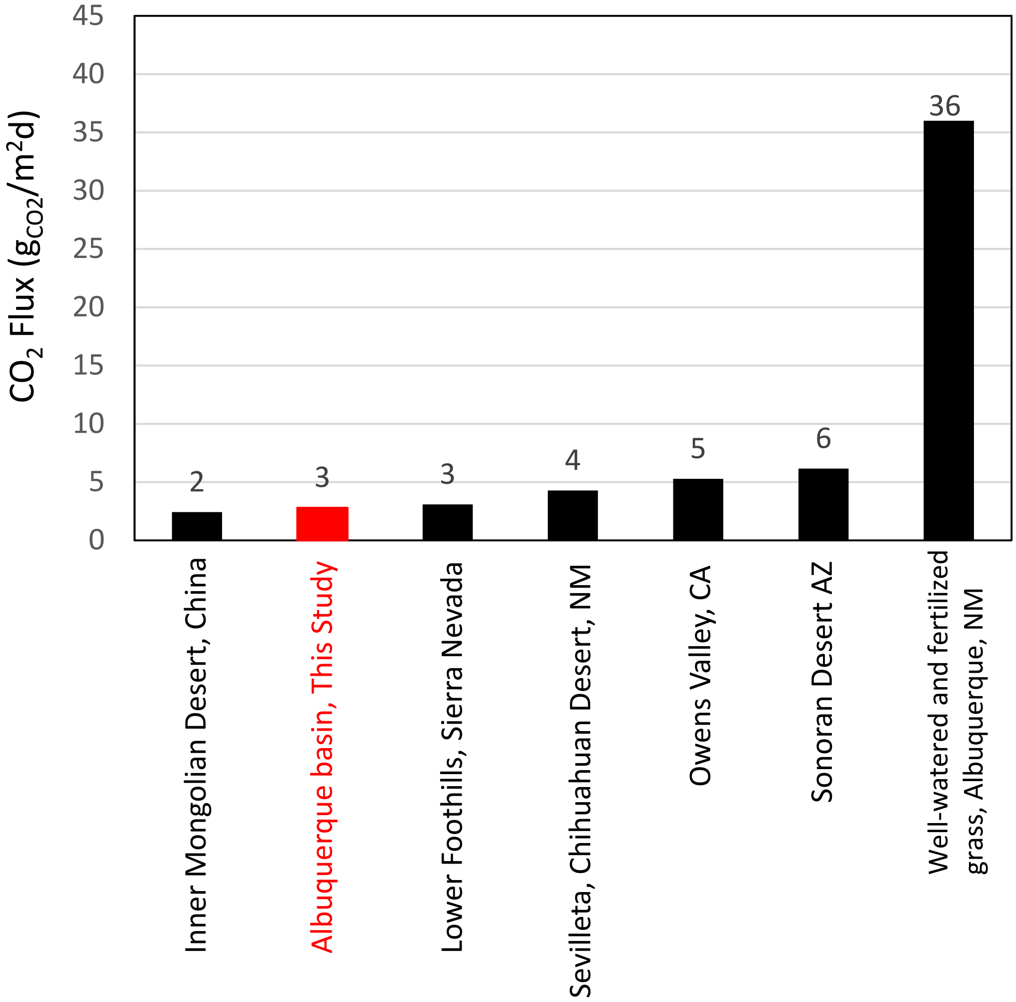
CO$_2$ Flux (g$_{CO2}$/m^{2}d)
0
5
10
15
20
25
30
35
40
45
2
3
3
4
5
6
36
Inner Mongolian Desert, China
Albuquerque basin, This Study
Lower Foothills, Sierra Nevada
Sevilleta, Chihuahuan Desert, NM
Owens Valley, CA
Sonoran Desert AZ
Well-watered and fertilized grass, Albuquerque, NM

Figure 22

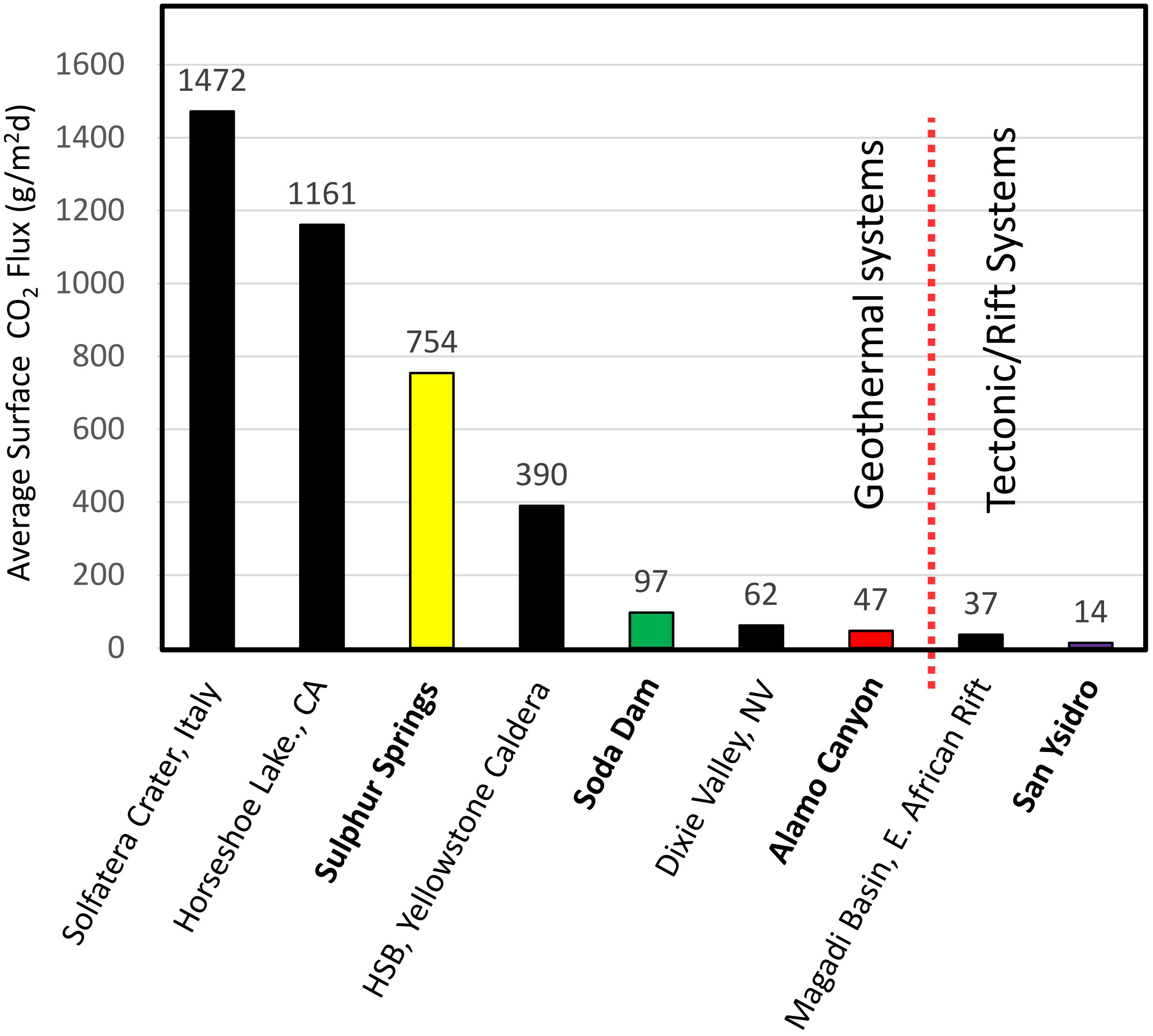
Average Surface CO$_2$ Flux (g/m^{2}d)
0
200
400
600
800
1000
1200
1400
1600
1472
1161
754
390
97
62
47
37
14
Geothermal systems
Tectonic/Rift Systems
Solfatera Crater, Italy
Horseshoe Lake., CA
Sulphur Springs
HSB, Yellowstone Caldera
Soda Dam
Dixie Valley, NV
Alamo Canyon
Magadi Basin, E. African Rift
San Ysidro

Table 1

Surface & Spring CO_2 Flux (g_{CO2}/m^2d)

Location	Mean	Min-Max	Count	95% Confidence Level
Zia Pueblo Faults	0.7	0.0 - 9.6	38	0.5
Carrizo Arroyo	2.4	0.0 - 11.3	48	0.6
Sand Hill Fault	3.3	0.0 - 7.7	40	0.6
Penasco Springs	251.2	0.0 - 2,400	40	232.5
Soda Dam	251.6	0.2 - 9,675	90	233.6
San Ysidro	1169.0	0.0 - 149,322	256	1448.4
Sulphur Springs	5937.0	8.6 - 170,0115	55	6850.9
Alamo Canyon	11285.7	0.7 - 144,240	60	8328.8

Surface CO_2 Flux (g_{CO2}/m^2d)

Location	Mean	Min - Max	Count	95% Confidence Level
Zia Pueblo Faults	0.7	0.0 - 9.6	38	0.5
Carrizo Arroyo	2.4	0.0 - 11.3	48	0.6
Sand Hill Fault	3.3	0.0 - 7.7	40	0.6
Penasco Springs	4.1	0.0 - 24.7	35	1.6
San Ysidro	13.8	0.2 - 434	238	4.5
Alamo Canyon	46.9	8.6 - 295	49	18.6
Soda Dam	96.6	0.2 - 3496	85	83.2
Sulphur Springs	754.3	8.6 - 2400	50	242.5

Spring CO_2 Flux (g_{CO2}/m^2d)

Location	Mean	Min - Max	Count	95% Confidence Level
Penasco Springs	1980.4	303 - 2400	5	1164.4
Soda Dam	2886.7	47.8 - 9675	5	4865.8
San Ysidro	16442.4	15.1 - 149,323	18	21166.3
Sulphur Springs	57759.0	2400 - 170,115	5	87521
Alamo Canyon	61349.1	2400 - 144,239	11	35275.6

Table 2

CO$_2$ flux (g$_{CO2}$/m^{2}d) Threshold Values (i.e. groups) for each Site					
Site	Background flux	Combination of background and diffuse flux	Diffuse flux	Combination of Diffuse and HPSF flux	HPSF flux
Alamo Canyon	0.7 - 4.0	4.0 - 15.5	15.5 - 1,778	NA	1,778 - 144,239
Sulphur Springs	NA	NA	8.6 - 60.3	60.3 - 302	302 - 170,112
Soda Dam	0.2 - 2.8	NA	2.8 - 32.4	32.4 - 200	200 - 9,675
Penasco Springs	0.0 - 2.5	2.51 - 4.0	4.0 - 13.2	NA	13.2 - 2,400
San Ysidro	0.0 - 1.3	NA	1.3 - 5.1	5.1 - 42.7	42.7 - 149,322
Zia Pueblo	0.0 - 1.7	NA	1.7 - 9.6	NA	NA
Sand Hill Fault	0.0 - 1.12	1.12 - 2.5	2.5 - 7.7	NA	NA
Carrizo Arroyo	0.0 - 1.0	1.0 - 2.5	2.5 - 11.3	NA	NA

NA = Not Applicable

Table 3

Comparisons of CO_2 Flux (g_{CO2}/m^2d)

Site Location	Mean	Min - Max	Count
Hot Spring Basin (Yellowstone Caldera)	320 ± 74	2 - 14,000	228
Solfatara of Pozzuoli Geothermal Field (Phlegraean Fields, Italy)	1,472	24 - 10,000	117
Grass Outside of Northrop Hall (EPS-UNM)	26	10 - 36	8
Arid Grassland(Sevilleta Wildlife Refuge)	N/A	0.95 - 3.9	>320
Average Anthropogenic CO_2 (Hydrocarbons - Temperate N. America)	N/A	1.3 - 1.5	N/A
Municipal Landfill (Hokhuvud, Sweden)	N/A	<0.0 - 63.4	N/A

(Chiodini, 1998; Werner et al, 2008; Vargas et al., 2012; Erickson et al., 2008; Borjesson and Svensson, 1997)

Appendices

Appendix A: General Stratigraphy of the Albuquerque Basin

Appendix B: CO_2 flux results for all sites

Appendix C: Helium isotope data for locations in New Mexico

Appendix D: Whole gas results for sites in this study and from other studies

Appendix A: General Stratigraphy of the Albuquerque Basin

Era	Period	Epoch	Stratigraphic units		Elevation (m)	Strat Thickness (m)
CENOZOIC	Neogene	Pliocene-Miocene	Santa Fe Group	Arroyo Ojito Fm	+ 1,747	847
				Zia Formation	+ 900	52
	Paleogene	Eocene	Gelisteo-San Jose Formation undivided		+ 848	205
MESOZOIC	Cretaceous	Late	Menefee Formation		+ 643	224
			Point Lookout Sandstone		+ 419	43
			Mancos Shale		+ 376	122
			Crevasse Canyon Formation		+ 254	236
			Niobrara Formation		+ 18	122
			Sanostee marker*		- 104	101
			Greenhorn Limestone		- 205	35
			Dakota Sandstone	“A” Sandstone Zone*	- 240	18
				“B” Sandstone Zone*	- 258	34
				“C” Sandstone Zone*	- 292	25
		Early		“D” Sandstone Zone*	- 317	35
	Jurassic	Late	Morrison Formation		- 352	166
			Todilto Limestone		- 518	23
		Early	Entrada Sandstone		- 541	70
	Triassic	Late	Chinle Formation		- 611	299
			Agua Zarca Sandstone Member		- 910	42
PALEOZOIC	Permian	Leonardian	San Andres Limestone		- 952	7
			Glorieta Sandstone		- 959	28
			Yeso Formation		- 987	117
			Meseta Blanca Sandstone Member		- 1,104	38
		Wolfcampian	Abo Formation		- 1,142	267
	Pennsylvanian		Madera Limestone		- 1,409	177
			Sandia Formation		Not Present	
PRE-CAMBRIAN	---	---	Precambrian		- 1,586	

General northern Albuquerque basin stratigraphy. Depths and stratigraphy units based on Santa Fe Pacific #1 well (modified from Black and Hiss, 1974). Elevation above (+) or below (-) sea level. * Marker beds and zones used locally in northwestern New Mexico.

Appendix B: Alamo Canyon CO_2 Flux Measurements

Plot #	Location	Latitude (DD)	Longitude (DD)	Day	Month	Hour	Min	ATMP (mb)	H_2O (mb)	CO_2 (ppm)	Time Elapsed (sec)	CO_2 Flux ($g/m^2/hr$)	CO_2 Flux ($g/m^2/day$)	CO_2 Flux ($mol/m^2/d$)
1	AC-W-NW	35.92000	-106.60260	22	7	10	34	757	699	1424	124	4.1	97.2	2.20
3	AC-W-NW-M-SP	35.91997	-106.60258	22	7	10	46	757	9999	42323	14	2634.3*	63223.2*	1433.63*
4	AC-W-NW-WS-SP	35.91990	-106.60240	22	7	10	49	757	9999	84014	14	6009.9*	144239.0*	3270.73*
5	AC-W-NW-S-SP	35.91970	-106.60230	22	7	10	53	757	9999	11193	24	436.0*	10464.6*	237.3*
6	AC-W-NW	35.91958	-106.60218	22	7	11	0	757	52	491	86	0.4	10.3	0.23
7	AC-W-NW	35.91948	-106.60202	22	7	11	5	757	33	463	124	0.2	4.6	0.10
8	AC-W-NW	35.91940	-106.60188	22	7	11	9	757	0	495	124	0.7	15.6	0.35
9	AC-W-NW	35.91929	-106.60186	22	7	11	17	757	5	446	124	0.0	0.7	0.02
10	AC-W-NW	35.91910	-106.60171	22	7	11	21	757	54	515	48	0.8	19.4	0.44
11	AC-W-NW	35.91918	-106.60163	22	7	11	23	757	111	628	14	5.6	133.4	3.03
12	AC-W-NW	35.91913	-106.60158	22	7	11	25	757	207	689	48	3.1	74.9	1.70
13	AC-W-NW	35.91907	-106.60151	22	7	11	29	757	36	467	124	0.2	5.0	0.11
14	AC-W-NW	35.91900	-106.60160	22	7	11	33	757	210	677	72	2.1	50.4	1.14
15	AC-W-NW	35.91872	-106.60138	22	7	11	39	757	1061	1685	62	12.3	295.0	6.69
16	AC-W-NW	35.91859	-106.60131	22	7	11	42	757	343	791	124	2.0	47.5	1.08
17	AC-W-NW	35.91830	-106.60117	22	7	11	47	757	83	520	124	0.5	11.5	0.26
18	AC-W-NE	35.91955	-106.60129	22	7	12	0	756	251	747	124	1.5	34.8	0.79
19	AC-W-NE	35.91947	-106.60139	22	7	12	4	756	75	518	124	0.4	10.3	0.23
20	AC-W-NE	35.91931	-106.60158	22	7	12	7	757	98	538	124	0.6	13.7	0.31
21	AC-W-NE	35.91916	-106.60176	22	7	12	11	757	14	444	124	0.1	1.9	0.04
22	AC-W-NE	35.91895	-106.60205	22	7	12	15	757	297	811	124	1.7	41.3	0.94
23	AC-W-NE	35.91884	-106.60222	22	7	12	19	757	100	533	124	0.6	13.9	0.32
24	AC-W-NE	35.91867	-106.60251	22	7	12	24	757	50	485	124	0.3	6.7	0.15
25	AC-W-NE	35.91860	-106.60268	22	7	12	28	757	66	530	124	0.4	9.1	0.21
26	AC-W-NE	35.91834	-106.60282	22	7	12	33	757	42	480	124	0.2	5.8	0.13
27	SG-S-SP	35.91874	-106.60081	22	7	12	50	757	9999	19829	14	890.5*	21371.3*	484.61*
28	SG-C	35.91898	-106.60081	22	7	12	54	757	29	474	124	0.2	3.8	0.09
29	SG-N	35.91885	-106.60081	22	7	12	59	757	26	456	124	0.2	3.6	0.08
30	AC-C-NS	35.91883	-106.59449	22	7	13	51	752	112	534	124	0.6	15.4	0.35
31	AC-C-NS	35.91848	-106.59446	22	7	13	54	752	200	660	28	5.0	119.8	2.72
32	AC-C-NS	35.91832	-106.59446	22	7	13	58	753	200	620	100	1.4	34.1	0.77
33	AC-C-NS	35.91795	-106.59448	22	7	14	2	754	203	640	105	1.4	33.1	0.75
34	AC-C-NS	35.91736	-106.59445	22	7	14	6	755	216	785	28	5.4	129.6	2.94
35	AC-C-NS	35.91729	-106.59444	22	7	14	10	755	172	634	124	1.0	23.8	0.54
36	AC-C-NS	35.91684	-106.59452	22	7	14	19	755	211	962	19	7.9	190.6	4.32
37	AC-C-NS	35.91640	-106.59454	22	7	14	24	754	106	546	124	0.6	14.6	0.33
38	AC-C-NS	35.91620	-106.59452	22	7	14	27	754	201	664	86	1.7	40.1	0.91
39	AC-C-SP-1	35.91668	-106.59453	22	7	14	36	755	9999	12716	28	380.7*	9137.9*	207.21*
40	AC-C-SP-2	35.91671	-106.59452	22	7	14	39	755	9999	17244	14	1087.6*	26101.9*	591.88*
41	AC-C-SP-3	35.91680	-106.59454	22	7	14	41	755	9999	99999	14	5817.9*	139630.2*	3166.22*
42	AC-C-LS-SP-1	35.91721	-106.59445	22	7	14	51	755	9999	44907	14	2903.0*	69672.6*	1579.88*
43	AC-C-LS-SP-2	35.91723	-106.59442	22	7	14	57	755	9999	50057	14	3151.1*	75625.5*	1714.86*
44	AC-C-EW	35.91729	-106.59393	22	7	15	13	754	95	531	124	0.6	13.2	0.30
45	AC-C-EW	35.91730	-106.59420	22	7	15	17	754	140	592	124	0.8	19.2	0.44
46	AC-C-EW	35.91732	-106.59465	22	7	15	22	755	45	471	124	0.3	6.2	0.14
47	AC-C-EW	35.91738	-106.59496	22	7	15	27	755	43	482	124	0.3	6.0	0.14
48	AC-C-EW	35.91730	-106.59530	22	7	15	31	755	24	455	124	0.1	3.1	0.07
49	AC-E-NE	35.91550	-106.58260	22	7	16	14	749	206	708	72	2.0	49.0	1.11
50	AC-E-NE	35.91530	-106.58270	22	7	16	18	750	159	613	124	0.9	21.8	0.50
51	AC-E-NE	35.91513	-106.58292	22	7	16	23	750	0	726	124	4.2	100.8	2.29
52	AC-E-NE	35.91507	-106.58302	22	7	16	27	751	25	458	124	0.1	3.4	0.08
53	AC-E-NE	35.91498	-106.58323	22	7	16	30	751	213	665	67	2.3	54.5	1.24
54	AC-E-BBP-SP-1	35.91483	-106.58343	22	7	16	35	752	9999	71920	14	4707.3*	112974.2*	2561.77*
55	AC-E-NE	35.91449	-106.58387	22	7	16	51	751	296	766	124	1.7	40.6	0.92
56	AC-E-NE	35.91431	-106.58416	22	7	16	55	751	143	587	124	0.8	19.7	0.45
57	AC-E-EW	35.91459	-106.58317	22	7	17	4	751	53	534	124	0.3	7.2	0.16
58	AC-E-EW	35.91483	-106.58337	22	7	17	7	751	1827	2494	124	10.5	251.5	5.70
59	AC-E-EW	35.91486	-106.58367	22	7	17	11	751	1122	1581	124	6.4	154.3	3.50
60	AC-E-EW	35.91501	-106.58396	22	7	17	15	751	270	705	124	1.6	37.2	0.84
62	AC-E-BBP-SP-2	35.91480	-106.58349	22	7	17	23	752	9999	99999	14	100.0	2399.8	54.42

* Flux calculated by hand, see methods section
AC = Alamo Canyon
SP = Spring measurement
M = Muddy
WS = White Salamander
W = West
NW-NE = Northwest-Northeast
SG = Smelly Ground
N-S = North-South
C = Center
LS = Lake Spring
BBP = Bubbling Bonanza Pond

DD = Decimal Degrees (NAD 83)
Plot # = Instrument input #
ATMP = Atmospheric Pressure

Appendix B: Sulphur Springs CO_2 Flux Measurements

Plot #	Location	Latitude (DD)	Longitude (DD)	Day	Month	Hour	Min	ATMP (mb)	H_2O (mb)	CO_2 (ppm)	Time Elapsed (sec)	CO_2 Flux ($g/m^2/hr$)	CO_2 Flux ($g/m^2/day$)	CO_2 Flux ($mol/m^2/d$)
1	SS-NS	35.908467	106.617433	8	7	10	52	764	73	655	14	3.8	90.0	2.04
2	SS-NS	35.908000	106.616983	8	7	10	55	764	284	894	14	14.5	348.0	7.89
3	SS-NS	35.907717	106.616867	8	7	10	59	765	324	1299	14	16.6	397.4	9.01
4	SS-NS	35.907550	106.616733	8	7	11	2	764	110	731	14	5.6	135.4	3.07
5	SS-NS	35.907450	106.616617	8	7	11	5	764	435	1936	14	22.2	531.8	12.06
6	SS-NS	35.907283	106.616450	8	7	11	7	764	696	1963	14	35.5	851.3	19.30
7	SS-NS	35.907067	106.616333	8	7	11	9	764	1920	4505	14	97.8	2346.5	53.21
8	SS-NS	35.906967	106.616283	8	7	11	13	764	6498	11981	14	100.0	2399.8	54.42
10	SS-MB-SP**	35.906900	106.616150	8	7	11	23	764	9999	46108	14	3357.9*	80591.8*	1827.5*
11	SS-NS	35.906850	106.616200	8	7	11	39	764	9999	99999	14	100.0	2399.8	54.42
12	SS-NS	35.906650	106.616117	8	7	11	42	763	58	606	28	1.5	35.3	0.80
13	SS-NS	35.906500	106.615983	8	7	11	45	763	416	1277	14	21.2	508.1	11.52
14	SS-NS	35.906333	106.615867	8	7	11	48	760	57	556	14	2.9	69.6	1.58
15	SS-NS	35.906167	106.615600	8	7	11	52	759	72	614	14	3.7	87.6	1.99
16	SS-EW	35.906500	106.616650	8	7	12	48	762	55	530	52	0.8	18.2	0.41
17	SS-EW	35.906583	106.616483	8	7	12	50	763	398	1175	14	20.3	487.0	11.04
18	SS-EW	35.906700	106.616383	8	7	12	53	763	476	1839	14	24.2	581.3	13.18
19	SS-EW	35.906817	106.616250	8	7	12	55	763	1209	3328	14	61.5	1476.2	33.47
20	SS-EW	35.906767	106.615883	8	7	12	58	763	668	1714	14	34.0	815.3	18.49
21	SS-EW	35.907100	106.615833	8	7	13	1	763	63	544	24	1.9	46.6	1.06
22	SS-EW	35.907267	106.615700	8	7	13	3	763	300	1122	14	15.3	366.2	8.30
23	SS-EW	35.907483	106.615533	8	7	13	5	763	1022	2304	14	52.0	1248.5	28.31
24	SS-EW	35.907750	106.615317	8	7	13	8	763	2345	6142	14	100.0	2399.8	54.42
25	SS-EW	35.908050	106.615283	8	7	13	11	764	455	1319	14	23.2	555.8	12.60
26	SS-EW	35.908233	106.615233	8	7	13	13	763	1568	5776	14	79.8	1914.2	43.41
27	SS-EW	35.908500	106.615050	8	7	13	15	763	82	612	14	4.2	100.6	2.28
28	SS-EW	35.908817	106.615050	8	7	13	18	763	234	1059	14	11.9	285.8	6.48
29	SS-EW	35.909017	106.615000	8	7	13	22	762	61	588	14	3.1	74.6	1.69
30	SS-KK	35.908317	106.615667	8	7	13	36	763	51	482	100	0.4	8.6	0.20
31	SS-KK	35.907883	106.615700	8	7	13	38	764	2940	6436	14	100.0	2399.8	54.42
32	SS-KK	35.907550	106.615933	8	7	13	41	763	347	1405	14	17.6	421.2	9.55
33	SS-KK	35.907133	106.616317	8	7	13	45	763	73	727	14	3.7	88.6	2.01
34	SS-KK	35.906733	106.616250	8	7	13	48	763	2359	5223	14	100.0	2399.8	54.42
35	SS-KK	35.906600	106.616333	8	7	13	50	762	714	1984	14	36.0	864.7	19.61
36	SS-KK	35.906250	106.616550	8	7	13	55	762	200	817	14	10.1	242.4	5.50
37	SS-KK-WB-SP	35.906467	106.616367	8	7	14	1	763	9999	60867	14	100.0	2399.8	54.42
38	SS-KK-LS-SP	35.907333	106.616150	8	7	14	7	764	9999	25255	14	100.0	2399.8	54.42
40	SS-KK-TS-SP**	35.907717	106.615850	8	7	14	11	767	9999	99999	14	1386.9*	33285.3*	754.8*
42	SS-KK-FB-SP**	35.908017	106.615650	8	7	14	16	767	9999	99999	14	7088.1*	170115.8*	3857.5*
43	SS-IC	35.908033	106.615817	8	7	14	23	763	63	577	19	2.4	57.8	1.31
44	SS-IC	35.908217	106.616017	8	7	14	26	763	54	561	19	2.1	49.7	1.13
45	SS-IC	35.908117	106.616317	8	7	14	28	763	87	664	14	4.4	105.8	2.40
46	SS-IC	35.907933	106.616583	8	7	14	31	763	124	638	14	6.3	151.4	3.43
47	SS-IC	35.907667	106.616633	8	7	14	34	764	56	504	43	0.9	22.6	0.51
48	SS-IC	35.907417	106.616433	8	7	14	36	763	248	1296	14	12.5	300.7	6.82
49	SS-IC	35.907400	106.616000	8	7	14	39	763	1932	4294	14	97.6	2342.9	53.13
50	SS-IC	35.907500	106.615600	8	7	14	41	763	2895	8487	14	100.0	2399.8	54.42
51	SS-IC	35.907667	106.615533	8	7	14	43	764	1523	3953	14	77.0	1846.8	41.88
52	SS-IC	35.908000	106.615717	8	7	14	45	763	788	1931	14	39.8	956.2	21.68
53	SS-OC	35.908517	106.615900	8	7	14	50	763	55	523	24	1.7	40.1	0.91
54	SS-OC	35.908217	106.616400	8	7	14	52	763	198	757	14	10.0	241.0	5.46
55	SS-OC	35.908050	106.616667	8	7	14	54	763	1124	2973	14	56.8	1363.2	30.91
56	SS-OC	35.907683	106.616950	8	7	14	57	764	118	783	14	6.0	143.8	3.26
57	SS-OC	35.907383	106.616933	8	7	14	59	763	539	1291	14	27.3	654.7	14.85
58	SS-OC	35.907300	106.616767	8	7	15	1	763	62	530	24	1.9	45.36	1.03

* Flux calculated by hand, see methods section
**Values replaced by 2016 measurement (previous 2015 measurement omitted)
SS = Sulphur Springs
NS = North-South Transect
EW = East-West Transect
SP = Spring Measurement
KK = Karl Karlstrom Array
IC = Inner Circle
OC = Outer Circle
MB = Mens Bathhouse
2399.8 and 99999 = instruments maximum flux and concentration detection output

WB = Womens Bathhouse
LS = Lemon Spring
TS = Tony's Spring
FB = Footbath Spring
TS, FB, and MB taken on 4/10/2016 with Tehnuka and Hyunwoo
DD = Decimal Degrees (NAD 83)
Plot # = Instrument input #
ATMP = Atmospheric Pressure

Appendix B: Soda Dam CO_2 Flux Measurements

Plot #	Location	Latitude (DD)	Longitude (DD)	Day	Month	Hour	Min	ATMP (mb)	H_2O (mb)	CO_2 (ppm)	Time Elapsed (sec)	CO_2 Flux ($g/m^2/hr$)	CO_2 Flux ($g/m^2/day$)	CO_2 Flux ($mol/m^2/d$)
1-1	JZF-Park-Lot-Soil	35.792714	-106.687058	9	6	10	48	818	12	445	124	0.1	1.7	0.04
2-1	SDF-NS-E-Rd	35.791740	-106.686490	9	6	10	59	818	22	462	124	0.1	3.1	0.07
3-1	SDF-NS-E-Rd	35.791788	-106.686483	9	6	11	3	818	52	495	100	0.4	9.6	0.22
4-1	SDF-NS-E-Rd	35.791830	-106.686482	9	6	11	7	818	40	477	124	0.3	6.0	0.14
5-1	SDF-NS-E-Rd	35.791890	-106.686484	9	6	11	11	818	48	475	124	0.3	7.2	0.16
6-1	SDF-NS-E-Rd	35.791927	-106.686492	9	6	11	14	818	52	496	81	0.5	11.8	0.27
7-1	SDF-NS-E-Rd	35.791961	-106.686501	9	6	11	19	818	42	473	124	0.3	6.2	0.14
9-1	SDF-NS-E-Rd	35.792042	-106.686536	9	6	11	27	818	2	461	124	0.0	0.2	0.01
10-1	SDF-NS-E-Rd	35.792074	-106.686551	9	6	11	30	818	318	1318	14	17.1	409.4	9.28
11-1	SDF-NS-E-Rd	35.792116	-106.686580	9	6	11	35	818	170	850	14	9.2	219.6	4.98
12-1	SDF-NS-E-Rd	35.792153	-106.686598	9	6	11	38	818	142	816	14	7.6	183.4	4.16
13-1	SDF-NS-E-Rd	35.792191	-106.686616	9	6	11	41	818	86	692	14	4.6	110.9	2.51
14-1	SDF-NS-E-Rd	35.792261	-106.686635	9	6	11	44	818	59	586	14	3.2	76.6	1.74
15-1	SDF-NS-E-Rd	35.792307	-106.686650	9	6	11	48	818	53	531	57	0.7	17.0	0.39
16-1	SDF-NS-E-Rd	35.792357	-106.686674	9	6	11	52	818	50	493	67	0.6	13.7	0.31
17-1	SDF-NS-E-Rd	35.792392	-106.686695	9	6	11	56	818	53	491	48	0.9	20.4	0.46
18-1	SDF-NS-E-Rd	35.792431	-106.686706	9	6	11	59	818	52	483	76	0.5	12.5	0.28
19-1	SDF-NS-E-Rd	35.792450	-106.686722	9	6	12	2	818	51	487	48	0.8	19.4	0.44
20-1	SDF-NS-E-Rd	35.792487	-106.686739	9	6	12	5	817	50	486	48	0.8	19.2	0.44
21-1	SDF-EW-W-Rd	35.792080	-106.686840	9	6	13	25	816	51	513	38	1.0	25.0	0.57
22-1	SDF-EW-W-Rd	35.792060	-106.686820	9	6	13	30	816	51	488	81	0.5	11.5	0.26
23-1	SDF-EW-W-Rd	35.792110	-106.686840	9	6	13	32	816	85	577	14	4.6	110.6	2.51
24-1	SDF-EW-E-River	35.792317	-106.686356	9	6	13	40	817	53	513	19	2.2	51.8	1.18
25-1	SDF-EW-E-River	35.792283	-106.686329	9	6	13	44	817	51	491	72	0.6	13.4	0.30
26-1	SDF-EW-E-River	35.792246	-106.686300	9	6	13	48	817	64	538	19	2.6	62.4	1.41
27-1	SDF-EW-E-River	35.792204	-106.686252	9	6	13	50	817	64	522	19	2.6	62.2	1.41
29-1	SD-EW-F	35.792117	-106.686454	9	6	14	13	816	50	479	91	0.4	10.1	0.23
30-1	SD-EW-F	35.792083	-106.686417	9	6	14	15	816	476	1009	14	25.8	618.0	14.01
31-1	SD-EW-F	35.791987	-106.686277	9	6	14	19	816	54	515	52	0.8	19.2	0.44
32-1	SD-EW-F	35.791900	-106.686150	9	6	14	21	816	58	523	24	1.9	45.6	1.03
34-1	SD-EW-F	35.791833	-106.686083	9	6	14	28	816	52	503	24	1.7	40.6	0.92
35-1	RVR-MND-SP	35.791480	-106.686240	9	6	14	51	817	330	857	14	17.9	429.1	9.73
39-1	Background	35.792288	-106.686591	9	6	15	16	816	81	570	14	4.4	105.1	2.38
41-1	Background	35.792288	-106.686591	9	6	15	19	816	72	529	14	3.9	93.6	2.12
48-2	JZF-Park-Lot-Soil	35.792735	-106.687072	9	6	19	42	816	35	465	124	0.2	5.0	0.11
49-2	JZF-NS-W-Rd	35.792764	-106.687079	9	6	19	46	816	20	471	124	0.1	2.9	0.07
50-2	JZF-NS-W-Rd	35.792800	-106.687100	9	6	19	49	816	1	454	124	0.0	0.2	0.01
51-2	JZF-NS-W-Rd	35.792847	-106.687126	9	6	19	52	816	50	485	96	0.4	9.6	0.22
52-2	JZF-NS-W-Rd	35.792890	-106.687150	9	6	19	57	816	56	495	28	1.5	36.2	0.82
53-2	JZF-NS-W-Rd	35.792940	-106.687160	9	6	19	59	816	59	515	19	2.4	57.4	1.30
54-2	JZF-NS-W-Rd	35.792990	-106.687220	9	6	20	1	816	58	511	28	1.6	37.7	0.85
55-2	JZF-NS-W-Rd	35.793010	-106.687220	9	6	20	3	816	57	497	28	1.5	36.5	0.83
56-2	JZF-NS-W-Rd	35.793050	-106.687244	9	6	20	5	816	52	485	48	0.8	20.2	0.46
57-2	JZF-NS-W-Rd	35.793070	-106.687260	9	6	20	7	816	54	486	48	0.9	20.9	0.47
58-2	JZF-NS-W-Rd	35.793130	-106.687260	9	6	20	9	816	51	480	52	0.8	18.0	0.41
59-2	JZF-NS-W-Rd	35.793164	-106.687285	9	6	20	12	816	51	495	48	0.8	19.7	0.45
60-2	JZF-NS-W-Rd	35.793210	-106.687300	9	6	20	14	816	52	554	43	0.9	22.3	0.51
61-2	JZF-NS-W-Rd	35.793230	-106.687310	9	6	20	15	816	56	505	33	1.3	30.7	0.70
62-2	JZF-NS-W-Rd	35.793270	-106.687330	9	6	20	18	816	52	486	28	1.4	33.6	0.76
63-2	JZF-NS-W-Rd	35.793320	-106.687350	9	6	20	20	816	54	487	33	1.3	30.0	0.68
64-2	JZF-NS-W-Rd	35.793350	-106.687370	9	6	20	22	816	52	487	28	1.4	33.8	0.77
65-2	JZF-NS-W-Rd	35.793400	-106.687370	9	6	20	24	816	55	502	33	1.3	30.5	0.69
66-2	JZF-NS-W-Rd	35.793410	-106.687380	9	6	20	27	816	62	535	19	2.5	59.8	1.36
67-2	JZF-NS-W-Road-AVG	35.793410	-106.687420	9	6	20	30	816	59	523	14	3.2	76.4	1.73
68-2	JZF-NS-W-Road-AVG	35.793460	-106.687440	9	6	20	34	816	173	717	14	9.3	222.0	5.03
69-2	JZF-NS-W-Rd	35.792690	-106.687030	9	6	20	39	816	54	494	43	1.0	23.3	0.53
70-2	JZF-NS-W-Rd	35.792650	-106.687030	9	6	20	42	816	52	478	100	0.4	9.4	0.21
71-2	JZF-NS-W-Rd	35.792610	-106.686990	9	6	20	46	816	9	436	124	0.1	1.4	0.03
72-2	JZF-NS-W-Rd	35.792587	-106.686972	9	6	20	50	816	8	435	124	0.1	1.2	0.03
73-2	JZF-NS-W-Rd	35.792570	-106.686950	9	6	20	53	816	25	451	124	0.2	3.6	0.08
74-2	JZF-NS-W-Rd	35.792540	-106.686929	9	6	20	56	816	30	445	124	0.2	4.3	0.10
75-2	JZF-NS-W-Rd	35.792493	-106.686918	9	6	21	0	816	10	437	124	0.1	1.4	0.03
76-2	JZF-NS-W-Rd	35.792450	-106.686900	9	6	21	1	816	53	493	24	1.7	41.0	0.93
77-2	JZF-NS-W-Rd	35.792410	-106.686870	9	6	21	3	816	87	573	14	4.7	111.8	2.54
78-2	JZF-NS-W-Rd	35.792378	-106.686841	9	6	21	5	816	116	606	14	6.3	150.0	3.40
79-2	JZF-EW	35.792500	-106.687300	9	6	22	13	813	52	495	72	0.6	13.2	0.30
80-2	JZF-EW	35.792510	-106.687370	9	6	22	15	813	51	498	19	2.0	49.0	1.11
81-2	JZF-EW	35.792560	-106.687380	9	6	22	17	813	68	559	14	3.6	86.4	1.96
82-2	JZF-EW	35.792770	-106.686670	9	6	22	21	814	51	490	19	2.0	48.5	1.10
83-2	JZF-EW	35.792800	-106.686720	9	6	22	24	814	53	488	28	1.4	34.1	0.77
84-2	JZF-EW	35.792720	-106.686630	9	6	22	27	814	55	492	38	1.1	26.2	0.59
85-2	JZF-EW-SP	35.792560	-106.686340	9	6	22	38	816	1475	2052	14	78.4	1881.8	42.67
86-2	JZF-EW	35.792580	-106.686290	9	6	22	42	814	52	516	33	1.2	28.8	0.65
87-2	JZF-EW	35.792510	-106.686310	9	6	22	44	816	50	495	43	0.9	21.4	0.48
88-2	RVR-MND-TO-JZF	35.791490	-106.686310	9	6	23	3	816	23	476	124	0.1	3.4	0.08

Appendix B: Soda Dam CO_2 Flux Measurements

Plot #	Location	Latitude (DD)	Longitude (DD)	Day	Month	Hour	Min	ATMP (mb)	H_2O (mb)	CO_2 (ppm)	Time Elapsed (sec)	CO_2 Flux ($g/m^2/hr$)	CO_2 Flux ($g/m^2/day$)	CO_2 Flux ($mol/m^2/d$)
89-2	RVR-MND-TO-JZF	35.791540	-106.686350	9	6	23	5	816	51	486	81	0.5	11.3	0.26
90-2	RVR-MND-TO-JZF	35.791580	-106.686320	9	6	23	9	814	50	496	28	1.4	32.4	0.73
91-2	RVR-MND-TO-JZF	35.791660	-106.686360	9	6	23	11	814	50	500	14	2.7	63.6	1.44
92-2	RVR-MND-TO-JZF	35.791720	-106.686360	9	6	23	13	814	63	506	19	2.5	60.7	1.38
93-2	RVR-MND-TO-JZF	35.791770	-106.686420	9	6	23	14	814	374	1038	14	19.8	475.9	10.79
94-2	RVR-MND-TO-JZF	35.791830	-106.686420	9	6	23	17	814	50	534	76	0.5	11.8	0.27
95-2	SD-BASE	35.791816	-106.686221	9	6	23	20	814	56	495	38	1.1	26.9	0.61
96-2	SD-BASE	35.791790	-106.686260	9	6	23	23	814	52	565	100	0.4	9.4	0.21
97-2	SD-BASE	35.791730	-106.686300	9	6	23	24	814	68	562	33	1.5	37.0	0.84
9-2016**	SD-ML-2016	35.792117	-106.686743	28	2	12	30	814	9999	99999	14	100.0	2399.8	54.42
10-2016**	SD-RBP-2016	35.792142	-106.686719	28	2	12	30	813	9999	13782	28	403.1*	9675.0*	219.4*
11-2016	SD-Grotto-2016	35.791814	-106.686107	28	2	12	30	814	315	1582	124	2.0	47.8	1.08
12-2016	SD-SF-2016	35.792138	-106.686585	28	2	12	30	814	523	892	124	3.3	79.4	1.80
13-2016	SD-PLF-2016	35.792428	-106.687072	28	2	12	30	813	9999	12037	72	145.6*	3495.4*	79.3*
14-2016	SD-Background-2016	35.792820	-106.687215	28	2	13	30	813	176	648	124	1.1	26.6	0.60

* Flux calculated by hand, see methods section

**Values replaced by 2016 measurement (previous 2015 measurement omitted)

Plot # = Instrument input #

ATMP = Atmospheric Pressure

SD = Soda Dam

JZF = Jemez Fault

SDF = Soda Dam Fault

RD = Road

f = Fissure

RVR = River

MND = Mound

ML = Mother Load

RBP = Roadside Bubbling Pool

SF = Surface Flux

PL F= Parking Lot Fence

DD = Decimal Degrees (NAD 83)

Appendix B: Penasco Springs CO_2 Flux Measurements

Plot #	Location	Latitude (DD)	Longitude (DD)	Day	Month	Hour	Min	ATMP (mb)	H_2O (mb)	CO_2 (ppm)	Time Elapsed (sec)	CO_2 Flux ($g/m^2/hr$)	CO_2 Flux ($g/m^2/day$)	CO_2 Flux ($mol/m^2/d$)
45	PS-23-NS	35.593750	-106.865233	13	6	7	35	827	3	445	124	0.0	0.5	0.01
46	PS-23-NS	35.593317	-106.865217	13	6	7	40	827	1	432	124	0.0	0.0	0.00
47	PS-23-NS	35.592717	-106.865233	13	6	7	45	827	21	454	124	0.1	3.1	0.08
48	PS-23-NS	35.592383	-106.865200	13	6	7	50	829	27	463	124	0.2	4.1	0.10
49	PS-23-NS	35.591867	-106.865317	13	6	7	55	829	7	445	124	0.1	1.2	0.03
50	PS-23-NS	35.591567	-106.865400	13	6	7	59	829	7	446	124	0.0	1.0	0.02
51	PS-23-NS	35.591267	-106.865400	13	6	8	5	829	31	470	124	0.2	4.6	0.11
52	PS-23-NS	35.591117	-106.865500	13	6	8	10	829	41	484	124	0.3	6.2	0.16
53	PS-23-NS	35.590867	-106.865467	13	6	8	15	829	0	437	124	0.0	0.0	0.00
54	PS-23-EW	35.591983	-106.863950	13	6	8	27	829	37	481	124	0.2	5.5	0.14
55	PS-23-EW	35.592050	-106.864167	13	6	8	30	829	55	526	43	1.0	24.7	0.62
56	PS-23-EW	35.592050	-106.864083	13	6	8	33	829	51	495	115	0.4	8.6	0.22
57	PS-23-EW	35.592050	-106.864450	13	6	8	38	829	52	499	96	0.4	10.3	0.26
58	PS-23-EW	35.592083	-106.864883	13	6	8	43	829	11	454	124	0.1	1.7	0.04
59	PS-23-EW	35.592050	-106.865483	13	6	8	47	829	31	465	124	0.2	4.8	0.12
60	PS-23-EW	35.592033	-106.865783	13	6	8	52	829	48	485	124	0.3	7.4	0.19
61	PS-23-EW	35.591983	-106.866317	13	6	8	57	829	3	435	124	0.0	0.5	0.01
62	PS-23-EW	35.592117	-106.866717	13	6	9	2	829	42	495	124	0.3	6.5	0.16
63	PS-23-Spr	35.592150	-106.865250	13	6	9	11	830	9999	29794	14	100.0	2399.8	59.99
64	PS-SP-Spr	35.601667	-106.856017	13	6	9	53	823	231	732	14	12.6	302.9	7.57
65	PS-SP-E	35.601567	-106.855833	13	6	9	58	822	2	433	124	0.0	0.2	0.01
66	PS-SP-NE	35.601833	-106.855783	13	6	10	2	822	19	452	124	0.1	2.9	0.07
67	PS-SP-N	35.602033	-106.856067	13	6	10	7	822	48	482	124	0.3	7.2	0.18
68	PS-SP-NW	35.602100	-106.856317	13	6	10	11	822	0	447	124	0.0	0.0	0.00
69	PS-SP-W	35.601950	-106.856817	13	6	10	16	823	40	472	124	0.3	6.0	0.15
70	PS-SP-SW	35.601750	-106.856983	13	6	10	20	823	31	463	124	0.2	4.6	0.11
71	PS-SP-SW	35.601533	-106.856800	13	6	10	24	823	32	468	124	0.2	4.8	0.12
72	PS-SP-SE	35.601433	-106.855933	13	6	10	29	822	7	436	124	0.0	1.0	0.02
73	PS-SP-SE-Spr	35.601250	-106.855883	13	6	10	33	822	9999	13272	14	100.0	2399.8	59.99
74	PS-SP-E	35.601200	-106.855467	13	6	10	38	822	13	445	124	0.1	1.9	0.05
75	PS-SP-NE	35.601700	-106.854733	13	6	10	47	820	31	462	124	0.2	4.6	0.11
76	PS-SP-N	35.602067	-106.854950	13	6	10	56	820	48	480	124	0.3	7.2	0.18
77	PS-SP-N	35.602317	-106.855617	13	6	11	2	821	31	456	124	0.2	4.8	0.12
78	PS-SP-W	35.602367	-106.856167	13	6	11	7	821	0	428	124	0.0	0.0	0.00
79	PS-SP-W	35.602300	-106.857067	13	6	11	13	823	3	428	124	0.0	0.5	0.01
80	PS-SP-SW	35.601450	-106.857033	13	6	11	19	823	11	439	124	0.1	1.7	0.04
81	PS-SP-S	35.601133	-106.856683	13	6	11	23	823	12	434	124	0.1	1.7	0.04
82	PS-SP-SE	35.601000	-106.855867	13	6	11	30	822	30	454	124	0.2	4.6	0.11
83	PS-BS-1-Spr	35.601783	-106.860550	13	6	11	48	824	9999	63718	14	100.0	2399.8	59.99
84	PS-BS-2-Spr	35.601950	-106.860567	13	6	11	51	824	9999	99999	14	100.0	2399.8	59.99

PS = Penasco Springs
Spr = Spring measurement
23 = Dave Deckers Spring#
NSEW = North South or East West Transect OR location around spring
SP = Swimming Pool Spring
BS = Bubbling Spring
DD = Decimal Degrees (NAD 83)
2399.8 an d 99999 = instruments maximum flux and concentration detection output

Plot # = Instrument input #
ATMP = Atmospheric Pressure

Appendix B: San Ysidro CO_2 Flux Measurements

Plot #	Location	Latitude (DD)	Longitude (DD)	Day	Month	Hour	Min	ATMP (mb)	H_2O (mb)	CO_2 (ppm)	Time Elapsed (sec)	CO_2 Flux ($g/m^2/hr$)	CO_2 Flux ($g/m^2/day$)	CO_2 Flux ($mol/m^2/d$)
1-1-08-2015	SY-TM-L2	35.537330	-106.849580	29	8	9	48	845	39	455	124	0.25	6.00	0.1
2-1-08-2015	SY-TM-L2	35.537300	-106.849490	29	8	9	52	845	40	455	124	0.26	6.24	0.1
3-1-08-2015	SY-TM-L2	35.537270	-106.849400	29	8	9	55	846	35	451	124	0.23	5.52	0.1
4-1-08-2015	SY-TM-L2	35.537230	-106.849270	29	8	9	59	846	33	447	124	0.22	5.28	0.1
5-1-08-2015	SY-TM-L2	35.537190	-106.849150	29	8	10	2	846	50	464	120	0.34	8.16	0.2
6-1-08-2015	SY-TM-L2	35.537170	-106.849040	29	8	10	6	846	32	443	124	0.21	5.04	0.1
7-1-08-2015	SY-TM-L2	35.537130	-106.848930	29	8	10	10	846	51	460	120	0.35	8.40	0.2
8-1-08-2015	SY-TM-L2	35.537090	-106.848840	29	8	10	13	846	29	440	124	0.19	4.56	0.1
9-1-08-2015	SY-TM-L2	35.537060	-106.848740	29	8	10	17	846	27	437	124	0.17	4.08	0.1
10-1-08-2015	SY-TM-L2	35.537040	-106.848660	29	8	10	19	846	51	466	28	1.46	35.04	0.8
11-1-08-2015	SY-TM-L2	35.537000	-106.848560	29	8	10	23	846	50	464	105	0.39	9.36	0.2
12-1-08-2015	SY-TM-L2	35.536980	-106.848450	29	8	10	27	846	40	454	124	0.26	6.24	0.1
13-1-08-2015	SY-TM-L2	35.536960	-106.848360	29	8	10	34	846	30	440	124	0.19	4.56	0.1
14-1-08-2015	SY-TM-L2	35.536930	-106.848230	29	8	10	37	846	31	442	124	0.20	4.80	0.1
15-1-08-2015	SY-TM-L2	35.536900	-106.848160	29	8	10	41	846	42	449	124	0.27	6.48	0.1
16-1-08-2015	SY-TM-L2	35.536870	-106.848020	29	8	10	44	846	29	439	124	0.19	4.56	0.1
18-1-08-2015	SY-TM-L2	35.536840	-106.847820	29	8	10	50	845	54	488	52	0.83	19.92	0.5
19-1-08-2015	SY-TM-L2	35.536830	-106.847720	29	8	10	57	846	39	443	124	0.26	6.24	0.1
20-1-08-2015	SY-TM-L2	35.536910	-106.847600	29	8	11	1	846	23	431	124	0.15	3.60	0.1
21-1-08-2015	SY-TM-L2	35.536840	-106.847480	29	8	11	3	846	55	459	38	1.18	28.32	0.6
22-1-08-2015	SY-TM-L2	35.536750	-106.847360	29	8	11	7	846	52	468	28	1.49	35.76	0.8
23-1-08-2015	SY-TM-L2	35.536740	-106.847260	29	8	11	13	846	21	436	124	0.14	3.36	0.1
24-1-08-2015	SY-TM-L2	35.536730	-106.847140	29	8	11	16	846	50	478	48	0.85	20.40	0.5
25-1-08-2015	SY-TM-L2	35.536700	-106.847050	29	8	11	18	846	55	492	24	1.89	45.36	1.0
26-1-08-2015	SY-TM-L2	35.536670	-106.846930	29	8	11	23	846	52	477	24	1.78	42.72	1.0
27-1-08-2015	SY-TM-L2	35.536650	-106.846820	29	8	11	26	846	51	462	105	0.40	9.60	0.2
28-1-08-2015	SY-TM-L2	35.536610	-106.846700	29	8	11	30	846	32	438	124	0.21	5.04	0.1
29-1-08-2015	SY-TM-L2	35.536620	-106.846630	29	8	11	33	846	50	461	86	0.47	11.28	0.3
30-1-08-2015	SY-TM-L2	35.536590	-106.846560	29	8	11	37	846	50	462	100	0.41	9.84	0.2
31-1-08-2015	SY-TM-L2	35.536560	-106.846440	29	8	11	42	846	17	422	124	0.11	2.64	0.1
33-1-08-2015	SY-TM-L2	35.536560	-106.846240	29	8	11	51	846	14	422	124	0.09	2.16	0.0
34-1-08-2015	SY-TM-L2	35.536540	-106.846120	29	8	11	55	846	48	459	124	0.32	7.68	0.2
35-1-08-2015	SY-TM-L2	35.536520	-106.845980	29	8	11	59	846	37	450	124	0.24	5.76	0.1
36-1-08-2015	SY-TM-L2	35.536520	-106.845890	29	8	12	4	846	39	450	124	0.26	6.24	0.1
37-1-08-2015	SY-TM-L2	35.536500	-106.845770	29	8	12	7	846	52	465	81	0.52	12.48	0.3
38-1-08-2015	SY-TM-L2	35.536500	-106.845710	29	8	12	10	846	54	465	52	0.85	20.40	0.5
39-1-08-2015	SY-TM-L2	35.536480	-106.845580	29	8	12	14	846	51	462	96	0.44	10.56	0.2
40-1-08-2015	SY-TM-L2	35.536473	-106.845512	29	8	12	18	846	43	456	124	0.28	6.72	0.2
41-1-08-2015	SY-TM-L4	35.535850	-106.850430	29	8	13	23	844	45	453	124	0.29	6.96	0.2
42-1-08-2015	SY-TM-L4	35.535800	-106.850320	29	8	13	26	844	51	458	120	0.35	8.40	0.2
43-1-08-2015	SY-TM-L4	35.535770	-106.850180	29	8	13	30	844	44	453	124	0.29	6.96	0.2
44-1-08-2015	SY-TM-L4	35.535740	-106.850130	29	8	13	33	844	50	455	105	0.38	9.12	0.2
45-1-08-2015	SY-TM-L4	35.535720	-106.850000	29	8	13	37	844	52	461	100	0.42	10.08	0.2
46-1-08-2015	SY-TM-L4	35.535670	-106.849880	29	8	13	40	844	37	445	124	0.24	5.76	0.1
47-1-08-2015	SY-TM-L4	35.535640	-106.849750	29	8	13	44	844	48	458	124	0.31	7.44	0.2
48-1-08-2015	SY-TM-L4	35.535610	-106.849660	29	8	13	47	844	52	461	86	0.49	11.76	0.3
49-1-08-2015	SY-TM-L4	35.535580	-106.849560	29	8	13	51	843	50	459	76	0.53	12.72	0.3
50-1-08-2015	SY-TM-L4	35.535540	-106.849470	29	8	13	53	843	53	468	62	0.69	16.56	0.4
51-1-08-2015	SY-TM-L4	35.535500	-106.849380	29	8	13	56	843	51	463	76	0.55	13.20	0.3
52-1-08-2015	SY-TM-L4	35.535460	-106.849320	29	8	14	0	843	33	437	124	0.22	5.28	0.1
53-1-08-2015	SY-TM-L4	35.535460	-106.849200	29	8	14	6	843	51	467	100	0.41	9.84	0.2
54-1-08-2015	SY-TM-L4	35.535390	-106.849100	29	8	14	9	841	51	457	100	0.42	10.08	0.2
55-1-08-2015	SY-TM-L4	35.535360	-106.849040	29	8	14	13	841	26	443	124	0.17	4.08	0.1
56-1-08-2015	SY-TM-L4	35.535320	-106.848910	29	8	14	17	841	42	445	124	0.28	6.72	0.2
57-1-08-2015	SY-TM-L4	35.535250	-106.848760	29	8	14	22	841	52	466	76	0.56	13.44	0.3
58-1-08-2015	SY-TM-L4	35.535190	-106.848680	29	8	14	25	841	52	465	62	0.68	16.32	0.4
59-1-08-2015	SY-TM-L4	35.535180	-106.848550	29	8	14	28	841	52	467	86	0.49	11.76	0.3
60-1-08-2015	SY-TM-L4	35.535140	-106.848480	29	8	14	30	841	104	575	14	5.92	142.08	3.2
61-1-08-2015	SY-TM-L4-SP	35.535140	-106.848410	29	8	14	36	841	4660	8996	124	39.02	936.58	21.2
62-1-08-2015	SY-TM-L4	35.535100	-106.848300	29	8	14	42	841	51	479	33	1.23	29.52	0.7
63-1-08-2015	SY-TM-L4	35.535040	-106.848180	29	8	14	45	840	53	517	28	1.48	35.52	0.8
64-1-08-2015	SY-TM-L4	35.534960	-106.848010	29	8	14	49	840	48	468	124	0.31	7.44	0.2
65-1-08-2015	SY-TM-L4	35.534930	-106.847910	29	8	14	51	841	325	1001	14	18.10	434.40	9.9
66-1-08-2015	SY-TM-L4	35.534900	-106.847910	29	8	14	56	841	12	435	124	0.08	1.92	0.0
67-1-08-2015	SY-TM-L4	35.534900	-106.847800	29	8	14	59	840	50	468	57	0.69	16.56	0.4
68-1-08-2015	SY-TM-L4	35.534850	-106.847580	29	8	15	2	840	51	470	72	0.57	13.68	0.3
69-1-08-2015	SY-TM-L4	35.534840	-106.847500	29	8	15	7	840	0	412	124	0.00	0.00	0.0
70-1-08-2015	SY-TM-L4	35.534820	-106.847390	29	8	15	10	840	1	410	124	0.00	0.00	0.0
71-1-08-2015	SY-TM-L4	35.534760	-106.847260	29	8	15	14	840	43	451	124	0.27	6.48	0.1
72-1-08-2015	SY-TM-L4	35.534740	-106.847140	29	8	15	17	840	53	466	57	0.74	17.76	0.4
73-1-08-2015	SY-TM-L4	35.534720	-106.847000	29	8	15	22	839	50	500	120	0.33	7.92	0.2
74-1-08-2015	SY-TM-L4	35.534680	-106.846940	29	8	15	27	840	51	462	120	0.34	8.16	0.2
75-1-08-2015	SY-TM-L4	35.534640	-106.846780	29	8	15	30	840	50	459	91	0.44	10.56	0.2
77-1-08-2015	SY-TM-L4	35.534630	-106.846550	29	8	15	40	840	50	469	105	0.38	9.12	0.2
78-1-08-2015	SY-TM-L4	35.534590	-106.846430	29	8	15	43	840	51	463	100	0.40	9.60	0.2
79-1-08-2015	SY-TM-L4	35.534570	-106.846350	29	8	15	46	840	52	465	67	0.62	14.88	0.3
80-1-08-2015	SY-TM-L4	35.534560	-106.846220	29	8	15	49	840	52	467	91	0.46	11.04	0.3
82-1-08-2015	SY-TM-Srfc-N	35.537460	-106.847660	30	8	11	7	843	43	477	124	0.27	6.48	0.1
83-1-08-2015	SY-TM-Srfc-N	35.537460	-106.847560	30	8	11	11	844	31	444	124	0.20	4.80	0.1

Appendix B: San Ysidro CO_2 Flux Measurements

Plot #	Location	Latitude (DD)	Longitude (DD)	Day	Month	Hour	Min	ATMP (mb)	H_2O (mb)	CO_2 (ppm)	Time Elapsed (sec)	CO_2 Flux ($g/m^2/hr$)	CO_2 Flux ($g/m^2/day$)	CO_2 Flux ($mol/m^2/d$)
84-1-08-2015	SY-TM-Srfc-N	35.537420	-106.847400	30	8	11	14	844	44	456	124	0.28	6.72	0.2
85-1-08-2015	SY-TM-Srfc-N	35.537040	-106.847420	30	8	11	18	844	42	453	124	0.27	6.48	0.1
86-1-08-2015	SY-TM-Srfc-N	35.536600	-106.847760	30	8	11	24	843	52	475	91	0.45	10.80	0.2
87-1-08-2015	SY-TM-Srfc-N	35.536510	-106.847710	30	8	11	29	843	20	433	124	0.13	3.12	0.1
88-1-08-2015	SY-Seep	35.536300	-106.847690	30	8	11	41	843	296	828	124	1.90	45.60	1.0
89-1-08-2015	SY-Seep	35.535960	-106.847850	30	8	11	45	843	357	1776	14	19.95	478.80	10.9
90-1-08-2015	SY-Bbl-SP	35.535790	-106.847850	30	8	11	51	843	9999	99999	14	99.99	2399.76	54.4
91-1-08-2015	SY-Seep-Fe	35.535430	-106.848080	30	8	11	54	841	1034	3370	14	57.57	1381.68	31.3
92-1-08-2015	SY-Seep-Blk	35.535180	-106.847820	30	8	11	59	841	50	471	62	0.64	15.36	0.3
93-1-08-2015	SY-Seep-Fe	35.535170	-106.848080	30	8	12	2	841	958	2378	14	53.33	1279.92	29.0
94-1-08-2015	SY-Seep-Fe	35.535020	-106.847990	30	8	12	6	840	69	556	14	3.87	92.88	2.1
95-1-08-2015	SY-Seep-Fe	35.535020	-106.847990	30	8	12	7	841	389	1296	14	21.63	519.12	11.8
96-1-08-2015	SY-Seep-Blk	35.535020	-106.847910	30	8	12	11	841	54	488	38	1.13	27.12	0.6
97-1-08-2015	SY-Seep-Blk	35.535110	-106.847790	30	8	12	15	841	53	474	67	0.63	15.12	0.3
98-1-08-2015	SY-Seep-Blk	35.535310	-106.847760	30	8	12	20	841	54	478	57	0.76	18.24	0.4
99-1-08-2015	SY-Seep-Blk	35.534760	-106.848050	30	8	12	24	840	55	477	43	1.02	24.48	0.6
1-2-08-2015	SY-TM-L1	35.539084	-106.849059	29	8	18	45	844	21	442	124	0.13	3.12	0.1
2-2-08-2015	SY-TM-L1	35.539102	-106.848976	29	8	18	50	844	38	457	124	0.25	6.00	0.1
3-2-08-2015	SY-TM-L1	35.539091	-106.848859	29	8	18	54	844	49	465	124	0.32	7.68	0.2
4-2-08-2015	SY-TM-L1	35.539085	-106.848862	29	8	18	57	844	33	445	124	0.21	5.04	0.1
5-2-08-2015	SY-TM-L1	35.539049	-106.848740	29	8	19	1	844	14	426	124	0.09	2.16	0.0
6-2-08-2015	SY-TM-L1	35.539018	-106.848607	29	8	19	5	844	41	455	124	0.27	6.48	0.1
7-2-08-2015	SY-TM-L1	35.538995	-106.848429	29	8	19	9	845	50	463	115	0.36	8.64	0.2
8-2-08-2015	SY-TM-L1	35.538985	-106.848316	29	8	19	13	844	29	442	124	0.19	4.56	0.1
9-2-08-2015	SY-TM-L1	35.538932	-106.847969	29	8	19	16	845	32	446	124	0.21	5.04	0.1
10-2-08-2015	SY-TM-L1	35.538932	-106.847831	29	8	19	20	844	27	442	124	0.18	4.32	0.1
11-2-08-2015	SY-TM-L1	35.538944	-106.847722	29	8	19	23	845	50	466	120	0.34	8.16	0.2
12-2-08-2015	SY-TM-L1	35.538931	-106.847596	29	8	19	27	844	21	436	124	0.13	3.12	0.1
13-2-08-2015	SY-TM-L1	35.538927	-106.847492	29	8	19	31	844	31	444	124	0.20	4.80	0.1
14-2-08-2015	SY-TM-L1	35.538877	-106.847374	29	8	19	34	845	47	456	124	0.30	7.20	0.2
15-2-08-2015	SY-TM-L1	35.538861	-106.847269	29	8	19	38	845	32	445	124	0.21	5.04	0.1
16-2-08-2015	SY-TM-L1	35.538839	-106.847138	29	8	19	41	845	28	442	124	0.18	4.32	0.1
17-2-08-2015	SY-TM-L1	35.538801	-106.847011	29	8	19	45	845	27	438	124	0.18	4.32	0.1
18-2-08-2015	SY-TM-L1	35.538807	-106.846897	29	8	19	49	845	32	470	124	0.21	5.04	0.1
19-2-08-2015	SY-TM-L1	35.538792	-106.846629	29	8	19	53	845	50	465	120	0.34	8.16	0.2
20-2-08-2015	SY-TM-L1	35.538773	-106.846508	29	8	19	57	845	33	447	124	0.21	5.04	0.1
21-2-08-2015	SY-TM-L1	35.538767	-106.846393	29	8	20	1	845	30	445	124	0.19	4.56	0.1
22-2-08-2015	SY-TM-L1	35.538741	-106.846261	29	8	20	5	845	39	452	124	0.25	6.00	0.1
23-2-08-2015	SY-TM-L1	35.538743	-106.846150	29	8	20	8	844	35	452	124	0.23	5.52	0.1
24-2-08-2015	SY-TM-L1	35.538755	-106.846067	29	8	20	12	844	37	451	124	0.24	5.76	0.1
25-2-08-2015	SY-TM-L1	35.538718	-106.845913	29	8	20	15	845	51	461	124	0.33	7.92	0.2
26-2-08-2015	SY-TM-L1	35.538709	-106.845795	29	8	20	19	845	44	452	124	0.28	6.72	0.2
27-2-08-2015	SY-TM-L1	35.538695	-106.845695	29	8	20	22	844	35	446	124	0.23	5.52	0.1
28-2-08-2015	SY-TM-L1	35.538685	-106.845529	29	8	20	25	844	27	438	124	0.18	4.32	0.1
29-2-08-2015	SY-TM-L1	35.538632	-106.845370	29	8	20	30	844	39	447	124	0.25	6.00	0.1
30-2-08-2015	SY-TM-L1	35.538639	-106.845289	29	8	20	33	844	46	453	124	0.30	7.20	0.2
31-2-08-2015	SY-TM-L1	35.538617	-106.845162	29	8	20	37	844	25	438	124	0.16	3.84	0.1
32-2-08-2015	SY-TM-L1	35.538625	-106.845009	29	8	20	40	844	45	459	124	0.29	6.96	0.2
33-2-08-2015	SY-TM-L1	35.538614	-106.844796	29	8	20	44	844	45	460	124	0.29	6.96	0.2
34-2-08-2015	SY-TM-L1	35.538595	-106.844686	29	8	20	47	844	14	429	124	0.09	2.16	0.0
35-2-08-2015	SY-TM-L1	35.538571	-106.844579	29	8	20	51	844	27	441	124	0.18	4.32	0.1
36-2-08-2015	SY-TM-L1	35.538574	-106.844445	29	8	20	54	844	36	457	124	0.23	5.52	0.1
37-2-08-2015	SY-TM-L1	35.538554	-106.844320	29	8	20	58	844	38	449	124	0.25	6.00	0.1
38-2-08-2015	SY-TM-L1	35.535330	-106.845354	29	8	21	1	844	27	442	124	0.17	4.08	0.1
39-2-08-2015	SY-TM-L1	35.538570	-106.844570	29	8	21	5	844	26	438	124	0.17	4.08	0.1
40-2-08-2015	SY-TM-L1	35.538502	-106.843904	29	8	21	8	844	36	446	124	0.23	5.52	0.1
41-2-08-2015	SY-TM-L3	35.535849	-106.849290	29	8	22	14	841	36	450	124	0.23	5.52	0.1
42-2-08-2015	SY-TM-L3	35.535855	-106.849184	29	8	22	18	841	51	463	115	0.36	8.64	0.2
43-2-08-2015	SY-TM-L3	35.535845	-106.849043	29	8	22	21	841	50	463	96	0.42	10.08	0.2
44-2-08-2015	SY-TM-L3	35.535861	-106.848908	29	8	22	24	841	52	470	81	0.52	12.48	0.3
45-2-08-2015	SY-TM-L3	35.535841	-106.848791	29	8	22	27	841	50	471	100	0.40	9.60	0.2
46-2-08-2015	SY-TM-L3	35.535825	-106.848694	29	8	22	31	841	23	442	124	0.15	3.60	0.1
47-2-08-2015	SY-TM-L3	35.535838	-106.848566	29	8	22	34	841	50	471	81	0.50	12.00	0.3
48-2-08-2015	SY-TM-L3	35.535811	-106.848442	29	8	22	37	841	10	424	124	0.06	1.44	0.0
49-2-08-2015	SY-TM-L3	35.535824	-106.848338	29	8	22	41	841	52	474	91	0.46	11.04	0.3
50-2-08-2015	SY-TM-L3	35.535787	-106.848231	29	8	22	44	841	50	501	124	0.32	7.68	0.2
51-2-08-2015	SY-TM-L3	35.535754	-106.848115	29	8	22	47	841	54	494	48	0.92	22.08	0.5
52-2-08-2015	SY-TM-L3	35.535765	-106.847976	29	8	22	49	841	73	553	14	4.14	99.36	2.3
54-2-08-2015	SY-TM-L3	35.535708	-106.847754	29	8	22	53	840	57	572	14	3.22	77.28	1.8
55-2-08-2015	SY-TM-L3	35.535673	-106.847641	29	8	22	56	841	54	510	43	1.02	24.48	0.6
56-2-08-2015	SY-TM-L3	35.535627	-106.847508	29	8	22	59	840	65	533	19	2.75	66.00	1.5
57-2-08-2015	SY-TM-L3	35.535629	-106.847404	29	8	23	2	840	50	489	28	1.42	34.08	0.8
58-2-08-2015	SY-TM-L3	35.535575	-106.847281	29	8	23	4	840	61	552	14	3.47	83.28	1.9
59-2-08-2015	SY-TM-L3	35.535539	-106.847170	29	8	23	7	840	48	471	124	0.31	7.44	0.2
60-2-08-2015	SY-TM-L3	35.535500	-106.847043	29	8	23	10	840	51	473	100	0.41	9.84	0.2
61-2-08-2015	SY-TM-L3	35.535469	-106.846918	29	8	23	14	840	52	475	91	0.46	11.04	0.3
62-2-08-2015	SY-TM-L3	35.535429	-106.846819	29	8	23	18	840	42	456	124	0.27	6.48	0.1
63-2-08-2015	SY-TM-L3	35.535430	-106.846682	29	8	23	22	840	0	501	124	0.00	0.00	0.0
64-2-08-2015	SY-TM-L3	35.535465	-106.846565	29	8	23	26	840	0	470	124	0.38	9.12	0.2

Appendix B: San Ysidro CO_2 Flux Measurements

Plot #	Location	Latitude (DD)	Longitude (DD)	Day	Month	Hour	Min	ATMP (mb)	H_2O (mb)	CO_2 (ppm)	Time Elapsed (sec)	CO_2 Flux ($g/m^2/hr$)	CO_2 Flux ($g/m^2/day$)	CO_2 Flux ($mol/m^2/d$)
65-2-08-2015	SY-TM-L3	35.535425	-106.846430	29	8	23	30	840	42	458	124	0.27	6.48	0.1
66-2-08-2015	SY-TM-L3	35.535386	-106.846320	29	8	23	33	840	51	468	86	0.48	11.52	0.3
67-2-08-2015	SY-TM-L3	35.535398	-106.846113	29	8	23	38	840	51	468	115	0.36	8.64	0.2
68-2-08-2015	SY-TM-L3	35.535409	-106.846007	29	8	23	40	840	53	509	33	1.30	31.20	0.7
69-2-08-2015	SY-TM-L3	35.535307	-106.845884	29	8	23	44	840	48	459	124	0.31	7.44	0.2
70-2-08-2015	SY-TM-L3	35.535247	-106.845795	29	8	23	47	840	50	472	72	0.56	13.44	0.3
71-2-08-2015	SY-TM-L3	35.535290	-106.845650	29	8	23	51	840	21	450	124	0.13	3.12	0.1
72-2-08-2015	SY-TM-L3	35.535299	-106.845492	29	8	23	56	840	32	444	124	0.21	5.04	0.1
73-2-08-2015	SY-TM-L3	35.535320	-106.845357	29	8	23	59	840	50	462	110	0.37	8.88	0.2
74-2-08-2015	SY-TM-L3	35.535355	-106.845224	30	8	0	2	840	25	434	124	0.16	3.84	0.1
75-2-08-2015	SY-TM-L3	35.535315	-106.845095	30	8	0	6	841	38	452	124	0.25	6.00	0.1
76-2-08-2015	SY-TM-L3	35.535355	-106.844965	30	8	0	9	841	51	467	96	0.43	10.32	0.2
77-2-08-2015	SY-TM-L3	35.535392	-106.844851	30	8	0	13	841	30	441	124	0.19	4.56	0.1
78-2-08-2015	SY-TM-L3	35.535437	-106.844711	30	8	0	17	841	24	437	124	0.15	3.60	0.1
79-2-08-2015	SY-TM-L3	35.535469	-106.844581	30	8	0	20	841	33	447	124	0.22	5.28	0.1
80-2-08-2015	SY-TM-L3	35.535461	-106.844352	30	8	0	24	841	10	427	124	0.06	1.44	0.0
25-1-06-2015	SY-GM-EW	35.517350	-106.846783	18	6	13	32	836	51	471	115	0.34	8.16	0.2
26-1-06-2015	SY-GM-EW	35.517617	-106.845983	18	6	13	37	835	4	428	124	0.02	0.48	0.0
27-1-06-2015	SY-GM-EW	35.517917	-106.845083	18	6	13	43	833	15	432	124	0.10	2.40	0.1
28-1-06-2015	SY-GM-EW	35.518183	-106.844400	18	6	13	47	832	53	489	38	1.08	25.92	0.6
29-1-06-2015	SY-GM-EW	35.518317	-106.843967	18	6	13	52	832	23	439	124	0.14	3.36	0.1
30-1-06-2015	SY-GM-EW	35.518583	-106.843250	18	6	13	57	833	41	462	124	0.26	6.24	0.1
31-1-06-2015	SY-GM-EW	35.518650	-106.843017	18	6	14	1	833	52	477	100	0.40	9.60	0.2
32-1-06-2015	SY-GM-NS	35.518883	-106.844583	18	6	14	9	831	50	476	96	0.41	9.84	0.2
33-1-06-2015	SY-GM-NS	35.518567	-106.844567	18	6	14	14	832	35	456	124	0.22	5.28	0.1
34-1-06-2015	SY-GM-NS	35.518550	-106.844433	18	6	14	16	832	52	491	48	0.85	20.40	0.5
36-1-06-2015	SY-GM-NS	35.517883	-106.844500	18	6	14	33	832	1	419	124	0.00	0.00	0.0
37-1-06-2015	SY-GM-NS	35.517600	-106.844467	18	6	14	36	832	36	455	124	0.23	5.52	0.1
38-1-06-2015	SY-GM-NS	35.516767	-106.844333	18	6	14	40	832	51	471	91	0.43	10.32	0.2
1-1-06-2015	SY-HM-EW	35.526683	-106.848800	18	6	10	41	838	51	476	105	0.38	9.12	0.2
2-1-06-2015	SY-HM-EW	35.526600	-106.848267	18	6	10	45	838	51	480	96	0.43	10.32	0.2
3-1-06-2015	SY-HM-EW	35.526450	-106.847717	18	6	10	50	836	24	448	124	0.15	3.60	0.1
4-1-06-2015	SY-HM-EW	35.526583	-106.847283	18	6	10	55	836	13	436	124	0.08	1.92	0.0
5-1-06-2015	SY-HM-EW	35.526867	-106.846250	18	6	11	2	836	22	445	124	0.14	3.36	0.1
6-1-06-2015	SY-HM-EW	35.526967	-106.845850	18	6	11	7	836	51	483	115	0.35	8.40	0.2
7-1-06-2015	SY-HM-EW	35.527017	-106.845700	18	6	11	12	837	15	435	124	0.10	2.40	0.1
8-1-06-2015	SY-HM-EW	35.527000	-106.845500	18	6	11	18	836	18	444	124	0.11	2.64	0.1
9-1-06-2015	SY-HM-EW	35.527000	-106.845150	18	6	11	23	835	21	443	124	0.13	3.12	0.1
10-1-06-2015	SY-HM-NS	35.528700	-106.846767	18	6	11	39	835	51	467	105	0.38	9.12	0.2
11-1-06-2015	SY-HM-NS	35.528283	-106.846800	18	6	11	43	835	46	478	124	0.29	6.96	0.2
13-1-06-2015	SY-HM-NS	35.527917	-106.846867	18	6	11	48	835	54	493	38	1.11	26.64	0.6
14-1-06-2015	SY-HM-NS	35.527567	-106.846717	18	6	11	53	835	50	488	67	0.59	14.16	0.3
15-1-06-2015	SY-HM-NS	35.527417	-106.846817	18	6	11	57	835	31	453	124	0.19	4.56	0.1
16-1-06-2015	SY-HM-NS	35.527017	-106.846783	18	6	12	1	834	0	414	124	0.00	0.00	0.0
18-1-06-2015	SY-HM-NS	35.526267	-106.846717	18	6	12	22	833	52	499	33	1.23	29.52	0.7
19-1-06-2015	SY-HM-NS	35.525583	-106.846683	18	6	12	28	832	37	458	124	0.23	5.52	0.1
20-1-06-2015	SY-HM-NS	35.525650	-106.846767	18	6	12	33	833	13	433	124	0.08	1.92	0.0
21-1-06-2015	SY-HM-NS	35.525167	-106.846850	18	6	12	37	833	50	490	67	0.58	13.92	0.3
22-1-06-2015	SY-HM-NS	35.524550	-106.846767	18	6	12	42	833	51	478	120	0.33	7.92	0.2
23-1-06-2015	SY-HM-NS	35.524433	-106.847150	18	6	12	47	833	19	434	124	0.12	2.88	0.1
24-1-06-2015	SY-HM-NS	35.523717	-106.846567	18	6	12	52	832	44	463	124	0.27	6.48	0.1
22-2-06-2015	SY-QF-EW	35.541367	-106.847883	18	6	21	56	839	17	440	124	0.11	2.64	0.1
23-2-06-2015	SY-QF-EW	35.541483	-106.847217	18	6	22	0	839	16	444	124	0.10	2.40	0.1
24-2-06-2015	SY-QF-EW	35.541567	-106.846650	18	6	22	5	839	20	441	124	0.13	3.12	0.1
25-2-06-2015	SY-QF-EW	35.541700	-106.846067	18	6	22	8	840	10	431	124	0.06	1.44	0.0
26-2-06-2015	SY-QF-EW	35.541783	-106.845483	18	6	22	12	839	18	442	124	0.11	2.64	0.1
27-2-06-2015	SY-QF-EW	35.541967	-106.844900	18	6	22	16	839	15	439	124	0.09	2.16	0.0
28-2-06-2015	SY-QF-EW	35.542050	-106.844333	18	6	22	20	839	40	552	124	0.25	6.00	0.1
29-2-06-2015	SY-QF-EW	35.542067	-106.843833	18	6	22	30	839	2	421	124	0.01	0.24	0.0
30-2-06-2015	SY-QF-EW	35.542300	-106.842917	18	6	22	34	839	24	445	124	0.15	3.60	0.1
31-2-06-2015	SY-QF-NS	35.539317	-106.846400	18	6	22	58	838	17	450	124	0.10	2.40	0.1
32-2-06-2015	SY-QF-NS	35.539783	-106.846433	18	6	23	2	838	11	430	124	0.07	1.68	0.0
33-2-06-2015	SY-QF-NS	35.540250	-106.846550	18	6	23	5	838	15	438	124	0.09	2.16	0.0
34-2-06-2015	SY-QF-NS	35.540750	-106.846600	18	6	23	9	838		448	124	0.15	3.60	0.1
35-2-06-2015	SY-QF-NS	35.541250	-106.846683	18	6	23	12	838	19	438	124	0.12	2.88	0.1
36-2-06-2015	SY-QF-NS	35.541817	-106.846717	18	6	23	17	839	12	435	124	0.07	1.68	0.0
37-2-06-2015	SY-QF-NS	35.542317	-106.846800	18	6	23	20	839	36	458	124	0.23	5.52	0.1
38-2-06-2015	SY-QF-NS	35.542867	-106.846883	18	6	23	24	838	4	427	124	0.02	0.48	0.0
39-2-06-2015	SY-QF-NS	35.542867	-106.846917	18	6	23	26	838	55	487	38	1.14	27.36	0.6
40-2-06-2015	SY-QF-NS	35.543933	-106.847100	18	6	23	31	838	36	455	124	0.22	5.28	0.1
0-2-06-2015	SY-TM-EW	35.536700	-106.847583	18	6	18	58	840	2	433	124	0.01	0.24	0.0
1-2-06-2015	SY-TM-EW	35.537000	-106.849317	18	6	19	14	840	47	469	124	0.30	7.20	0.2
2-2-06-2015	SY-TM-EW	35.536917	-106.848917	18	6	19	17	840	53	477	67	0.63	15.12	0.3
3-2-06-2015	SY-TM-EW	35.536867	-106.848433	18	6	19	21	840	53	478	91	0.46	11.04	0.3
4-2-06-2015	SY-TM-EW	35.536800	-106.848017	18	6	19	29	840	0	421	124	0.00	0.00	0.0
5-2-06-2015	SY-TM-EW	35.536600	-106.847367	18	6	19	35	840	24	453	124	0.15	3.60	0.1
6-2-06-2015	SY-TM-EW	35.536533	-106.846917	18	6	19	40	840	54	484	43	1.00	24.00	0.5
7-2-06-2015	SY-TM-EW	35.536467	-106.846467	18	6	19	44	840	47	473	124	0.30	7.20	0.2
8-2-06-2015	SY-TM-EW	35.536400	-106.846033	18	6	19	48	840	45	472	124	0.28	6.72	0.2

Appendix B: San Ysidro CO_2 Flux Measurements

Plot #	Location	Latitude (DD)	Longitude (DD)	Day	Month	Hour	Min	ATMP (mb)	H_2O (mb)	CO_2 (ppm)	Time Elapsed (sec)	CO_2 Flux ($g/m^2/hr$)	CO_2 Flux ($g/m^2/day$)	CO_2 Flux ($mol/m^2/d$)
9-2-06-2015	SY-TM-EW	35.536267	-106.845533	18	6	19	51	840	51	483	76	0.53	12.72	0.3
10-2-06-2015	SY-TM-NS	35.535067	-106.847867	18	6	20	14	838	105	579	14	5.83	139.92	3.2
11-2-06-2015	SY-TM-NS	35.534733	-106.847900	18	6	20	18	838	46	475	124	0.29	6.96	0.2
12-2-06-2015	SY-TM-NS	35.535417	-106.847800	18	6	20	25	839	55	494	28	1.53	36.72	0.8
13-2-06-2015	SY-TM-NS	35.535733	-106.847833	18	6	20	27	839	52	476	24	1.75	42.00	1.0
14-2-06-2015	SY-TM-NS	35.536067	-106.847750	18	6	20	30	840	54	484	43	0.99	23.76	0.5
15-2-06-2015	SY-TM-NS	35.536483	-106.847650	18	6	20	33	840	51	475	91	0.45	10.80	0.2
16-2-06-2015	SY-TM-NS	35.537000	-106.847483	18	6	20	37	840	50	471	115	0.35	8.40	0.2
17-2-06-2015	SY-TM-NS	35.537367	-106.847367	18	6	20	40	840	51	474	105	0.39	9.36	0.2
18-2-06-2015	SY-TM-NS	35.537700	-106.847267	18	6	20	44	840	39	461	124	0.25	6.00	0.1
19-2-06-2015	SY-TM-NS	35.538050	-106.847117	18	6	20	46	840	50	471	81	0.49	11.76	0.3
20-2-06-2015	SY-TM-NS	35.538383	-106.847067	18	6	20	50	840	51	469	115	0.35	8.40	0.2
1-2016	SY-Background	35.537402	-106.847705	27	2	9	27	841	8	440	124	0.05	1.20	0.0
3-2016	SY-TMW-SP	35.536850	-106.847757	27	2	9	50	843	9999	99999	14	6221.8*	149322.5*	3385.99*
4-2016	SY-TME-SP**	35.536750	-106.847570	27	2	9	54	841	9999	24672	14	896.1*	21505.9*	487.66*
5-2016	SY-LB	35.535599	-106.847567	27	2	10	3	839	9999	99999	14	4729.3*	113503.43*	2573.77*
6-2016	SY-DS**	35.527900	-106.846800	27	2	10	23	834	1363	1867	124	9.0	214.80	4.9
7-2016	SY-HM**	35.526647	-106.846740	27	2	10	30	830	9040	9887	124	59.1	1418.40	32.2
8-2016	SY-GM**	35.518100	-106.844583	27	2	10	30	827	9999	8733	67	124.1*	2978.1*	67.53*

* Flux calculated by hand, see methods section

**Values replaced by 2016 measurement (previous 2015 measurement omitted)

SY = San Ysidro
TM = Twin Mounds
L1,2,3,4 = Line-1,2,3,4
SP = Spring
E = East
N = North
W = West
Srfc = Surface measurement

Bbl = Bubbling
Fe = Iron
Blk = Black
LB = Little Bubbler
DS = Dry Spring
HS = High Mound
GS = Grassy mound
DD = Decimal Degrees (NAD 83)
Plot # = Instrument input #
ATMP = Atmospheric Pressure

Appendix B: Zia Pueblo CO_2 Flux Measurements

Plot #	Location	Latitude (DD)	Longitude (DD)	Day	Month	Hour	Min	ATMP (mb)	H_2O (mb)	CO_2 (ppm)	Time Elapsed (sec)	CO_2 Flux ($g/m^2/hr$)	CO_2 Flux ($g/m^2/day$)	CO_2 Flux ($mol/m^2/d$)
1	ZP-SA-Stop1-Fault	35.082683	-106.622767	3	12	10	10	838	0.0	432	124	0.02	0.48	0.01
2	ZP-SA-Stop1-Fault	35.082683	-106.622767	3	12	10	14	838	0.0	434	124	0.02	0.48	0.01
3	ZP-SA-Stop1-Fault	35.532233	-106.668083	3	12	10	18	838	0.0	436	124	0.02	0.48	0.01
4	ZP-SA-Stop1-Fault	35.534650	-106.670933	3	12	10	23	838	0.0	442	124	0.05	1.20	0.03
5	ZP-SA-Stop1-Fault	35.534667	-106.670833	3	12	10	26	839	0.0	440	124	0.02	0.48	0.01
6	ZP-SA-Stop1-Fault	35.534667	-106.670667	3	12	10	29	839	0.0	439	124	0.00	0.00	0.00
7	ZP-SA-Stop1-Fault	35.534683	-106.670600	3	12	10	33	839	0.0	432	124	0.03	0.72	0.02
8	ZP-SA-Stop1-Fault	35.534667	-106.670567	3	12	10	37	839	0.0	427	124	0.01	0.24	0.01
9	ZP-SA-Stop1-Fault	35.534617	-106.670467	3	12	10	41	840	0.0	429	124	0.02	0.48	0.01
10	ZP-SA-Stop1-Fault	35.534650	-106.670517	3	12	10	45	840	0.0	442	124	0.00	0.00	0.00
11	ZP-SA-Stop1-Fault	35.534650	-106.670383	3	12	10	49	839	0.0	429	124	0.03	0.72	0.02
12	ZP-SA-Stop1-Fault	35.534650	-106.670267	3	12	10	54	839	0.0	428	124	0.02	0.48	0.01
13	ZP-SA-Stop1-Fault	35.534617	-106.670217	3	12	10	58	838	0.0	427	124	0.00	0.00	0.00
14	ZP-SA-Stop1-Fault	35.534700	-106.670017	3	12	11	2	839	0.0	423	124	0.00	0.00	0.00
16	ZP-SA-Stop1-Fault	35.534750	-106.669983	3	12	11	10	839	0.0	425	124	0.00	0.00	0.00
17	ZP-SA-Stop1-Fault	35.534700	-106.669583	3	12	11	15	839	0.0	428	124	0.01	0.24	0.01
18	ZP-SA-Stop1-Fault	35.534783	-106.670550	3	12	11	23	840	0.0	457	124	0.01	0.24	0.01
19	ZP-SA-Stop1-Fault	35.534817	-106.670300	3	12	11	28	840	0.0	432	124	0.01	0.24	0.01
20	ZP-SC-Stop2-Fault	35.563117	-106.550217	3	12	12	22	830	0.0	423	124	0.00	0.00	0.00
23	ZP-SC-Stop2-Fault	35.562590	-106.549990	3	12	12	33	830	0.0	423	124	0.00	0.00	0.00
25	ZP-SC-Stop2-Fault	35.562710	-106.549740	3	12	12	40	830	0.0	425	124	0.00	0.00	0.00
26	ZP-SC-Stop2-Fault	35.562530	-106.549590	3	12	12	44	830	0.0	426	124	0.00	0.00	0.00
27	ZP-SC-Stop2-Fault	35.563200	-106.549417	3	12	12	52	826	0.0	480	100	0.40	9.60	0.22
29	ZP-SC-Stop2-Fault	35.562600	-106.549450	3	12	13	12	827	0.0	429	124	0.00	0.00	0.00
30	ZP-CN-Stop3-Fault	35.571890	-106.737533	3	12	14	41	840	0.0	432	124	0.04	0.96	0.02
31	ZP-CN-Stop3-Fault	35.571217	-106.737533	3	12	14	45	840	0.0	424	124	0.01	0.24	0.01
32	ZP-CN-Stop3-Fault	35.571483	-106.737400	3	12	14	49	840	0.0	424	124	0.01	0.24	0.01
33	ZP-CN-Stop3-Fault	35.571917	-106.737533	3	12	14	53	840	0.0	425	124	0.02	0.48	0.01
34	ZP-CN-Stop3-Fault	35.572183	-106.737400	3	12	14	57	840	0.0	424	124	0.03	0.72	0.02
35	ZP-CN-Stop3-Fault	35.572240	-106.737350	3	12	15	0	840	0.0	426	124	0.04	0.96	0.02
36	ZP-CN-Stop3-Fault	35.572260	-106.737383	3	12	15	4	840	0.0	428	124	0.04	0.96	0.02
37	ZP-CN-Stop3-Fault	35.572250	-106.737380	3	12	15	7	840	0.0	432	124	0.05	1.20	0.03
38	ZP-CN-Stop3-Fault	35.572360	-106.737320	3	12	15	15	840	0.0	432	124	0.05	1.20	0.03
39	ZP-CN-Stop3-Fault	35.572540	-106.737210	3	12	15	18	840	0.0	430	124	0.03	0.72	0.02
40	ZP-CN-Stop3-Fault	35.572670	-106.737150	3	12	15	22	840	0.0	430	124	0.01	0.24	0.01
41	ZP-SF-Stop4-Fault	35.454833	-106.707430	3	12	16	22	840	0.0	424	124	0.02	0.48	0.01
42	ZP-SF-Stop4-Fault	35.454840	-106.707340	3	12	16	26	840	0.0	421	124	0.01	0.24	0.01
43	ZP-SF-Stop4-Fault	35.454820	-106.707280	3	12	16	30	840	0.0	421	124	0.01	0.24	0.01

ZP = Zia Pueblo
SA = Santa Ana
SC = Silica Cemented fault
CN = Cerrito Negro
SF = Southern Fault
DD = Decimal Degrees (NAD 83)
Plot # = Instrument input #
ATMP = Atmospheric Pressure

Appendix B: Sand Hill Fault CO_2 Flux Measurements

Plot #	Location	Latitude (DD)	Longitude (DD)	Day	Month	Hour	Min	ATMP (mb)	H_2O (mb)	CO_2 (ppm)	Time Elapsed (sec)	CO_2 Flux ($g/m^2/hr$)	CO_2 Flux ($g/m^2/day$)	CO_2 Flux ($mol/m^2/d$)
0	SHF-EW-C	35.245867	-106.869767	26	6	8	14	822	0	424	124	0.0	0.0	0.00
1	SHF-EW-C	35.245900	-106.870026	26	6	8	20	823	20	440	124	0.1	2.9	0.07
3	SHF-EW-C	35.245900	-106.870317	26	6	8	28	823	12	432	124	0.1	1.7	0.04
4	SHF-EW-C	35.245800	-106.870633	26	6	8	37	823	14	439	124	0.1	1.9	0.04
5	SHF-EW-C	35.245767	-106.870800	26	6	8	42	823	31	453	124	0.2	4.6	0.10
6	SHF-EW-C	35.245867	-106.871067	26	6	8	46	823	44	463	124	0.3	6.7	0.15
7	SHF-EW-C	35.245900	-106.871200	26	6	8	49	824	43	458	124	0.3	6.5	0.15
8	SHF-EW-C	35.245983	-106.871567	26	6	8	53	824	29	448	124	0.2	4.3	0.10
9	SHF-EW-C	35.246100	-106.872083	26	6	8	57	824	19	438	124	0.1	2.9	0.07
10	SHF-EW-C	35.246333	-106.872717	26	6	9	1	824	25	441	124	0.2	3.8	0.09
11	SHF-EW-C	35.246100	-106.873483	26	6	9	6	825	32	452	124	0.2	4.8	0.11
12	SHF-EW-S	35.245233	-106.870217	26	6	9	20	827	10	427	124	0.1	1.4	0.03
13	SHF-EW-S	35.245100	-106.870250	26	6	9	24	827	3	423	124	0.0	0.5	0.01
14	SHF-EW-S	35.244950	-106.870250	26	6	9	28	829	3	420	124	0.0	0.5	0.01
15	SHF-EW-S	35.244917	-106.870233	26	6	9	33	829	6	423	124	0.0	0.7	0.02
16	SHF-EW-S	35.244833	-106.870317	26	6	9	38	829	14	430	124	0.1	1.9	0.04
17	SHF-EW-S	35.244717	-106.870433	26	6	9	42	829	10	429	124	0.1	1.4	0.03
18	SHF-EW-S	35.244633	-106.870567	26	6	9	48	829	6	423	124	0.0	1.0	0.02
19	SHF-EW-S	35.244433	-106.870900	26	6	9	59	829	14	430	124	0.1	2.2	0.05
20	SHF-EW-S	35.244017	-106.871400	26	6	10	4	830	35	452	124	0.2	5.3	0.12
21	SHF-EW-S	35.243783	-106.871917	26	6	10	9	831	34	454	124	0.2	5.0	0.11
22	SHF-NS	35.243967	-106.869850	26	6	10	22	829	15	432	124	0.1	2.2	0.05
23	SHF-NS	35.244261	-106.870117	26	6	10	28	827	13	429	124	0.1	1.9	0.04
24	SHF-NS	35.244467	-106.870083	26	6	10	31	827	9	432	124	0.1	1.4	0.03
25	SHF-NS	35.245167	-106.870417	26	6	10	41	826	23	437	124	0.1	3.4	0.08
27	SHF-NS	35.245683	-106.870817	26	6	11	9	824	29	447	124	0.2	4.3	0.10
28	SHF-NS	35.246417	-106.870867	26	6	11	15	825	19	436	124	0.1	2.9	0.07
29	SHF-NS	35.246350	-106.871050	26	6	11	18	825	31	444	124	0.2	4.6	0.10
30	SHF-NS	35.247067	-106.871283	26	6	11	24	825	18	434	124	0.1	2.6	0.06
31	SHF-NS	35.247033	-106.871367	26	6	11	27	825	19	434	124	0.1	2.9	0.07
32	SHF-NS	35.248250	-106.871517	26	6	11	33	826	51	473	124	0.3	7.7	0.17
33	SHF-NS	35.248300	-106.871300	26	6	11	37	826	23	442	124	0.1	3.4	0.08
34	SHF-NS	35.249050	-106.871467	26	6	11	43	826	22	441	124	0.1	3.4	0.08
35	SHF-NS	35.249033	-106.871667	26	6	11	47	826	43	463	124	0.3	6.5	0.15
36	SHF-EW-N	35.248250	-106.870200	26	6	11	55	825	34	453	124	0.2	5.0	0.11
37	SHF-EW-N	35.248283	-106.870817	26	6	11	59	825	26	444	124	0.2	3.8	0.09
38	SHF-EW-N	35.248283	-106.871067	26	6	12	3	826	44	458	124	0.3	6.7	0.15
39	SHF-EW-N	35.248250	-106.871717	26	6	12	7	826	14	438	124	0.1	1.9	0.04
40	SHF-EW-N	35.248300	-106.872217	26	6	12	11	826	22	439	124	0.1	3.4	0.08
41	SHF-EW-N	35.248367	-106.872717	26	6	12	16	825	20	436	124	0.1	2.9	0.07

SHF = Sand Hill Fault
C = Center Transect
S = Southern Transect
N = Northern Transect
DD = Decimal Degrees (NAD 83)
Plot # = Instrument input #
ATMP = Atmospheric Pressure

Appendix B: Carrizo Arroyo CO_2 Flux Measurements

Plot #	Location	Latitude (DD)	Longitude (DD)	Day	Month	Hour	Min	ATMP (mb)	H_2O (mb)	CO_2 (ppm)	Time Elapsed (sec)	CO_2 Flux (g/m^2/hr)	CO_2 Flux (g/m^2/day)	CO_2 Flux (mol/m^2/d)
1	CA-01-EW	34.76943	-107.08076	6	2	12	11	853	2	430	124	0.01	0.24	0.01
2	CA-02-EW	34.76944	-107.08089	6	2	12	14	853	0	430	124	0.00	0.00	0.00
3	CA-03-EW	34.76944	-107.08105	6	2	12	19	853	6	435	124	0.04	0.96	0.02
4	CA-04-EW	34.76943	-107.08121	6	2	12	23	853	10	440	124	0.07	1.68	0.04
5	CA-05-EW	34.76945	-107.08134	6	2	12	27	853	0	431	124	0.00	0.00	0.00
6	CA-06-EW	34.76944	-107.08147	6	2	12	30	853	0	428	124	0.00	0.00	0.00
7	CA-07-EW	34.76946	-107.08163	6	2	12	34	853	2	427	124	0.01	0.24	0.01
8	CA-08-EW	34.76946	-107.08179	6	2	12	38	853	10	435	124	0.07	1.68	0.04
9	CA-09-EW	34.76943	-107.08192	6	2	12	42	852	3	428	124	0.02	0.48	0.01
10	CA-10-EW	34.76945	-107.08209	6	2	12	46	852	3	429	124	0.02	0.48	0.01
11	CA-11-EW	34.76945	-107.08225	6	2	12	50	852	7	432	124	0.04	0.96	0.02
12	CA-12-EW	34.76945	-107.08241	6	2	12	54	853	10	436	124	0.07	1.68	0.04
13	CA-13-EW	34.76945	-107.08256	6	2	12	58	852	8	435	124	0.06	1.44	0.03
14	CA-14-EW	34.76946	-107.08272	6	2	13	2	852	8	436	124	0.05	1.20	0.03
15	CA-15-EW	34.76948	-107.08289	6	2	13	5	852	16	443	124	0.11	2.64	0.06
16	CA-16-EW	34.76957	-107.08304	6	2	13	10	852	5	431	124	0.03	0.72	0.02
17	CA-17-EW	34.76968	-107.08331	6	2	13	14	851	14	443	124	0.10	2.40	0.05
18	CA-18-EW	34.76967	-107.08364	6	2	13	18	851	24	459	124	0.16	3.84	0.09
19	CA-19-EW	34.76967	-107.08401	6	2	13	22	851	16	446	124	0.11	2.64	0.06
20	CA-20-EW	34.76966	-107.08433	6	2	13	27	851	17	452	124	0.11	2.64	0.06
21	CA-21-EW	34.76960	-107.08476	6	2	13	31	850	15	446	124	0.10	2.40	0.05
22	CA-22-EW	34.76957	-107.08521	6	2	13	36	850	15	446	124	0.10	2.40	0.05
23	CA-23-EW	34.76959	-107.08567	6	2	14	0	850	19	450	124	0.13	3.12	0.07
24	CA-24-EW	34.76963	-107.08614	6	2	14	5	849	8	433	124	0.05	1.20	0.03
25	CA-25-EW	34.76959	-107.08662	6	2	14	10	849	15	440	124	0.10	2.40	0.05
26	CA-26-EW	34.76979	-107.08707	6	2	14	15	849	15	437	124	0.10	2.40	0.05
27	CA-27-EW	34.76992	-107.08754	6	2	14	20	848	9	432	124	0.06	1.44	0.03
28	CA-28-EW	34.77005	-107.08805	6	2	14	25	849	23	489	124	0.16	3.84	0.09
29	CA-29-EW	34.77005	-107.08830	6	2	14	29	849	23	446	124	0.16	3.84	0.09
30	CA-30-EW	34.77005	-107.08842	6	2	14	37	849	0	423	124	0.00	0.00	0.00
31	CA-31-EW	34.77007	-107.08853	6	2	14	41	849	5	428	124	0.03	0.72	0.02
32	CA-32-EW	34.77014	-107.08873	6	2	14	46	849	31	458	124	0.21	5.04	0.11
33	CA-33-EW	34.77013	-107.08886	6	2	14	50	848	25	451	124	0.17	4.08	0.09
34	CA-34-EW	34.77009	-107.08896	6	2	14	54	848	36	462	124	0.25	6.00	0.14
35	CA-35-EW	34.77009	-107.08905	6	2	14	57	847	50	483	91	0.47	11.28	0.26
36	CA-36-EW	34.77010	-107.08920	6	2	15	2	848	21	446	124	0.14	3.36	0.08
37	CA-37-NS1	34.77084	-107.08866	6	2	15	10	849	26	448	124	0.17	4.08	0.09
38	CA-38-NS1	34.77070	-107.08860	6	2	15	14	849	38	459	124	0.26	6.24	0.14
39	CA-39-NS1	34.77051	-107.08868	6	2	15	19	849	11	433	124	0.08	1.92	0.04
40	CA-40-NS1	34.77035	-107.08867	6	2	15	23	848	9	435	124	0.06	1.44	0.03
41	CA-41-NS1	34.77018	-107.08866	6	2	15	27	848	8	435	124	0.05	1.20	0.03
42	CA-42-NS1	34.77003	-107.08876	6	2	15	31	848	12	443	124	0.08	1.92	0.04
43	CA-43-NS1	34.76982	-107.08881	6	2	15	35	848	18	442	124	0.12	2.88	0.07
44	Ca-44-NS1	34.76947	-107.08884	6	2	15	43	848	1	426	124	0.01	0.24	0.01
45	CA-45-NS2	34.77004	-107.08249	6	2	15	59	847	29	457	124	0.19	4.56	0.10
46	CA-46-NS2	34.76979	-107.08251	6	2	16	3	847	19	444	124	0.12	2.88	0.07
47	CA-47-NS2	34.76960	-107.08222	6	2	16	8	849	19	449	124	0.13	3.12	0.07
48	CA-48-NS2	34.76957	-107.08184	6	2	16	12	849	18	448	124	0.12	2.88	0.07

CA = Carrizo Arroyo
EW = East West Transect
NS = North South Transect (no. 1 or no. 2)
DD = Decimal Degrees (NAD 83)
Plot # = Instrument input #
ATMP = Atmospheric Pressure

Appendix C: R_C/R_A Gas Results from Various Authors

Location	State	Spring Name	Source Reference	Latitude	Longitude	Rc/Ra
Pagosa Springs	CO	Pagosa Hot Spr - south of main terrace	Newell et al., 2005	37.300000	-107.000000	0.11
Pagosa Springs	CO	Pagosa Hot Spr - travertine summit	Newell et al., 2005	37.300000	-107.000000	0.09
Pagosa Springs	CO	Pagosa Springs	Crossey et al., 2016	37.264529	-107.010831	0.08
San Juan Basin	CO	San Juan Basin Carter Ute 100	Zhou et al., 2005	37.027851	-107.904577	0.10
San Juan Basin	CO	San Juan Basin Carter Ute 102	Zhou et al., 2005	37.015627	-107.886042	0.10
San Juan Basin	CO	San Juan Basin Ute 112	Zhou et al., 2005	37.030579	-108.012568	0.10
San Juan Basin	CO	San Juan Basin Ute 121	Zhou et al., 2005	37.030603	-107.993923	0.10
San Juan Basin	CO	San Juan Basin Ute 152	Zhou et al., 2005	37.015657	-108.029485	0.30
San Juan Basin	CO	San Juan Basin, Ute 101	Zhou et al., 2005	37.044192	-107.993895	0.10
San Juan Basin	CO	San Juan Basin, Ute 132	Zhou et al., 2005	37.016535	-107.995067	0.10
San Juan Basin	CO	San Juan Basin, Ute 161	Zhou et al., 2005	37.016102	-108.047572	0.10
San Juan Basin	CO	San Juan Basin, Ute 202	Zhou et al., 2005	37.004799	-108.064063	0.10
San Juan Basin	CO	San Juan Basin, Ute 212	Zhou et al., 2005	37.004337	-108.047102	0.10
San Juan Basin	CO	San Juan Basin, Ute 221	Zhou et al., 2005	37.003892	-108.029018	0.10
San Juan Basin	CO	San Juan Basin, Ute 231	Zhou et al., 2005	37.004296	-108.013226	0.10
San Juan Basin	CO	San Juan Basin, Ute 242	Zhou et al., 2005	37.004759	-107.995178	0.10
San Juan Basin	CO	San Juan Basin, Ute 301	Zhou et al., 2005	37.044645	-108.029503	0.10
San Juan Basin	CO	San Juan Basin, Ute 351	Zhou et al., 2005	37.064129	-108.011073	0.10
San Juan Basin	CO	San Juan Basin, Ute 401	Zhou et al., 2005	37.045530	-108.047625	0.10
San Juan Basin	CO	San Juan Basin, Ute 901	Zhou et al., 2005	37.029711	-108.046419	0.10
San Juan Basin	CO	San Juan Basin Ute 141	Zhou et al., 2005	37.016076	-108.013129	0.10
San Juan Basin	CO	Southern Ute 300	Zhou et al., 2005	37.063676	-108.046654	0.09
San Juan Basin	CO	Southern Ute 304	Zhou et al., 2005	37.079051	-108.029748	0.10
Abiquiu	NM	Abiquiu, NM 1	n.a.	36.194637	-106.331480	0.23
Abiquiu	NM	Abiquiu, NM 2	n.a.	36.194637	-106.331480	0.20
Abiquiu	NM	Abiquiu, NM 3	n.a.	36.194637	-106.331480	0.18
ABQ Basin	NM	coyote fault well	Williams et al., 2013	35.291615	-106.893990	0.62
ABQ Basin	NM	coyote spring - short sample	Williams et al., 2013	35.291615	-106.893990	0.60
ABQ Basin	NM	Coyote Sprs	Williams et al., 2013	34.998576	-106.471256	0.87
ABQ Basin	NM	Tierra Amarilla - twin mounds	Crossey et al., 2016	35.536744	-106.847567	0.17
ABQ Basin	NM	Tierra Amarilla Anticline - Grassy Spr	Newell et al., 2005	35.516175	-106.843978	0.20
ABQ Basin	NM	Tierra Amarilla N of highway	Crossey et al., 2016	35.547150	-106.826790	0.39
ABQ Basin	NM	Zia Hot Well	Goff and Janik, 2002	35.645590	-106.889102	0.23
ABQ Basin	NM	San Acacia puddle	Williams et al., 2013	34.263610	-106.884160	0.95
ABQ Basin	NM	Laguna Mound Spring	n.a. LC13-NM-LAG-1	34.849992	-107.089483	0.25
ABQ Basin	NM	Eddelman Spring	Williams et al., 2013	34.785890	-106.404110	0.85
ABQ Basin	NM	Four Daughters Spring	Williams et al., 2013	34.593292	-107.191490	0.59
ABQ Basin	NM	Jemez Pueblo Upper Owl Spr	Newell et al., 2005	35.628845	-106.762875	0.38
ABQ Basin	NM	Jemez Pueblo,Salt Spr	Newell et al., 2005	35.597751	-106.760471	0.11
ABQ Basin	NM	Salado Arroyo Spr	Newell et al., 2005	34.700000	-107.100000	0.61
ABQ Basin	NM	San Acacia Spring	Williams et al., 2013	34.263840	-106.878760	0.26
ABQ Basin	NM	San Acacia Well	Williams et al., 2013	34.263730	-106.884520	0.80
Bitter Lakes	NM	Bitter Lakes- Sinkhole-17	Crossey et al., 2016	33.484658	-104.408411	0.60
Bitter Lakes	NM	Bitter Lakes- Sago Spring	Crossey et al., 2016	33.478156	-104.419800	0.17
Chama	NM	Chama hot spring	Crossey et al., 2016	36.543144	-106.717472	0.06
Chimayo	NM	Chimayo Geyser Well	Crossey et al., 2016	35.990394	-105.943833	0.52
Chimayo	NM	Chimayo Well	Goff and Janik, 2002	36.000000	-105.900000	0.65
Delaware Basin	NM	Delaware Basin, Bajillo Draw "WQ"	Phinney et al., 1978	33.400000	-104.400000	0.10
Delaware Basin	NM	Delaware Basin, Barn Federal	Phinney et al., 1978	33.400000	-104.400000	0.09
Delaware Basin	NM	Delaware Basin, Carrot Federal	Phinney et al., 1978	33.400000	-104.400000	0.04
Delaware Basin	NM	Delaware Basin, China Federal	Phinney et al., 1978	33.400000	-104.400000	0.06
Delaware Basin	NM	Delaware Basin, Dee "OQ" State	Phinney et al., 1978	33.500000	-104.200000	0.05
Delaware Basin	NM	Delaware Basin, Duncan Federal	Phinney et al., 1978	33.400000	-104.200000	0.08
Delaware Basin	NM	Delaware Basin, Long Arroyo "OW"	Phinney et al., 1978	33.500000	-104.100000	0.04
Delaware Basin	NM	Delaware Basin, Macho State	Phinney et al., 1978	33.500000	-104.400000	0.09
Delaware Basin	NM	Delaware Basin, Middle Fork Federal	Phinney et al., 1978	33.500000	-104.300000	0.03
Delaware Basin	NM	Delaware Basin, Spear "OA"	Phinney et al., 1978	33.400000	-104.100000	0.13
Delaware Basin	NM	Delaware basin, Thorpe "MI" Federal	Phinney et al., 1978	33.400000	-104.200000	0.07
Delaware Basin	NM	Delaware Basin, Williamson "LC" Federal	Phinney et al., 1978	33.400000	-104.200000	0.02
Espanola Basin	NM	Lucero Uplift Unnamed Mineral Spr	Newell et al., 2005	34.500000	-107.200000	0.47
Espanola Basin	NM	Manby Hot Spr Pool bathhouse*	Newell et al., 2005	36.500000	-105.700000	0.32
Espanola Basin	NM	Manby Hot Spr Pool S of bathhouse	Newell et al., 2005	36.500000	-105.700000	0.30
Espanola Basin	NM	Pajarito Spring- Jemez	Crossey et al., 2016	35.805464	-106.197114	1.83
Great Plains	NM	Ponce de Leon Hot Spr Hottest in concrete	Newell et al., 2005	34.300000	-105.600000	0.20
Jemez Mountains	NM	Jemez, Soda Dam Hot Spr	Goff and Janik, 2002	35.791000	-106.686000	0.84
Jemez Mountains	NM	Jemez Hot Spr Travertine Mound	Goff and Janik, 2002	35.771981	-106.690110	1.27
La Madera	NM	La Madera pool	Blomgren, 2016	36.360990	-106.050700	0.39
La Madera	NM	Statue Spring	Blomgren, 2016	36.382080	-106.060130	0.26
La Madera	NM	La Madera - Travertine Spr	Newell et al., 2005	36.400000	-106.000000	0.33
Ojo Caliente	NM	Ojo Caliente hot well	Blomgren, 2016	36.305492	-106.051980	0.14
Ojo Caliente	NM	Ojo Caliente Iron spring	Blomgren, 2016	36.304573	-106.052953	0.16
Penasco	NM	Penasco Springs	n.a. - LC14-NM-PS-22	35.590086	-106.865891	0.19

Appendix C: R_C/R_A Gas Results from Various Authors

Location	State	Spring Name	Source Reference	Latitude	Longitude	Rc/Ra
San Juan Basin	NM	Atlantic C 202	Zhou et al., 2005	36.840691	-107.924273	0.10
San Juan Basin	NM	Burroughs Com A100	Zhou et al., 2005	36.984604	-107.887385	0.10
San Juan Basin	NM	Culpepper Martin 103	Zhou et al., 2005	36.957310	-108.099885	0.08
San Juan Basin	NM	Culpepper Martin 109	Zhou et al., 2005	36.942423	-108.118567	0.10
San Juan Basin	NM	Decker 100	Zhou et al., 2005	36.996170	-108.086770	0.10
San Juan Basin	NM	Grenier 101	Zhou et al., 2005	36.913197	-108.030766	0.10
San Juan Basin	NM	Grenier 103	Zhou et al., 2005	36.884431	-108.013587	0.10
San Juan Basin	NM	Heizer 100	Zhou et al., 2005	36.984411	-107.869764	0.10
San Juan Basin	NM	King 200	Zhou et al., 2005	36.797467	-107.871341	0.20
San Juan Basin	NM	Maddox Com 100	Zhou et al., 2005	36.995876	-107.977124	0.10
San Juan Basin	NM	Maddox Mark 102	Zhou et al., 2005	36.984875	-107.976695	0.10
San Juan Basin	NM	Maddox Waller 101	Zhou et al., 2005	36.984489	-107.959078	0.10
San Juan Basin	NM	Page Com 100	Zhou et al., 2005	36.996595	-107.923047	0.10
San Juan Basin	NM	Primo Mudge 100	Zhou et al., 2005	36.970787	-107.941443	0.10
San Juan Basin	NM	San Juan Basin Gas	Zhou et al., 2005	36.000000	-108.000000	0.13
San Juan Basin	NM	Sanchez 2	Zhou et al., 2005	36.768797	-107.872298	0.20
San Juan Basin	NM	Stull 100	Zhou et al., 2005	36.996439	-107.870217	0.10
San Ysidro	NM	San Ysidro (LC07-SY-1)	Crossey et al., 2016	35.534908	-106.846977	0.17
Sandia Mountains	NM	Montezuma Hot Spr* (Bench Mk 290 1957)	Newell et al., 2005	35.700000	-105.300000	0.08
Socorro	NM	Socorro spring	Williams et al., 2013	34.041405	-106.935070	0.20
Socorro	NM	Socorro, Sedillo Sp.	Newell et al., 2005	34.000000	-106.900000	0.40
Socorro	NM	NM WT well- Socorro-1	Crossey et al., 2016	34.073233	-106.945010	1.41
Socorro	NM	NM WT well- Socorro-2	Crossey et al., 2016	34.073233	-106.945010	1.91
Socorro	NM	Rio Salado Box	Williams et al., 2013	34.327580	-107.094570	0.37
T or C	NM	Palomas Basin Artesian Well	n.a. - LC15-NM-SBR-1	33.325054	-107.363413	0.30
Taos	NM	Big Spring	n.a. - VB15_Big_Spring	36.278600	-105.793500	0.87
Taos	NM	No Agua	n.a. - VB15_No_Agua	36.761831	-105.958264	0.12
Taos	NM	Tusas Warm Spring	n.a. - VB15_Warm_spring	36.834718	-106.214072	0.95
Taos	NM	Black Rock Hot Spring	Newell et al., 2005	36.500000	-105.700000	0.09
Valles Caldera	NM	Jemez sulfur Sp womens bths	Goff and Janik, 2002	35.907000	-106.614000	6.16
Valles Caldera	NM	Jemez, Baca wells	Goff and Janik, 2002	35.900000	-106.600000	4.75
Valles Caldera	NM	Jemez, sulfur sp Footbath Spr. N=12	Goff and Janik, 2002	35.907000	-106.614000	5.16
Valles Caldera	NM	Jemez, VC-2a well	Goff and Janik, 2002	35.900000	-106.550000	5.00
Valles Caldera	NM	Jemez, VC-2b well	Goff and Janik, 2002	35.900000	-106.600000	5.72
Valles Caldera	NM	Womens Bath House, Sulphur Sprs - Jemez	Goff and Janik, 2002	35.907000	-106.614000	6.16
Valles Caldera	NM	Zia, C spr	Goff and Janik, 2002	35.606568	-106.885398	0.32
Valles Caldera	NM	Baca well 24	Truesdell and Janik, 1986	35.885825	-106.581993	3.39
Valles Caldera	NM	Baca well 4	Truesdell and Janik, 1986	35.888989	-106.571063	3.86
Valles Caldera	NM	Baca well 15	Truesdell and Janik, 1986	35.893188	-106.580717	4.14

n.a. unpublished data - sample ID given -Laura Crossey (LC) and Valerie Blomgren (VB)

Appendix D: Descriptions and Locations of Gas Results

Sample ID	Location	Site	Source	Latitude	Longitude
JS-ZP-SC-BKG	Albuquerque Basin	Background	This study	35.562600	-106.549450
JS-ZP-SC	Albuquerque Basin	Silica Cement Fault	This study	35.563200	-106.549417
JS-SY-BKG	Albuquerque Basin	Background	This study	35.53685	-106.847757
JS-SY-LB	Albuquerque Basin	Little Bubbler	This study	35.535599	-106.847567
JS-SD-BKG-air	Valles Caldera	Air	This study	35.7926000	-106.6870000
JS-SD-BKG	Valles Caldera	Background	This study	35.792820	-106.687215
JS-SD-SF	Valles Caldera	Surface Flux	This study	35.792138	-106.686585
JS-SD-Grotto	Valles Caldera	Grotto	This study	35.791814	-106.686107
JS-SY-TMW	Albuquerque Basin	Twin Mounds West	This study	35.53685	-106.847757
JS-SY-HM	Albuquerque Basin	High Mound	This study	35.526647	-106.84674
JS-SY-GM	Albuquerque Basin	Grassy Mound	This study	35.5181	-106.844583
JS-SD-PL	Valles Caldera	Parking Lot	This study	35.792428	-106.687072
JS-SY-TME	Albuquerque Basin	Twin Mounds East	This study	35.53675	-106.84757
JS-SY-DS	Albuquerque Basin	Dry Spring	This study	35.5279	-106.8468
Mud Spring	Valles Caldera	Mud Spring	This study	35.91997	-106.60258
White Smoker Spring	Valles Caldera	White Smoker Spring	This study	35.91990	-106.60240
JS-SD-RSS	Valles Caldera	Road Side Spring	This study	35.792142	-106.686719
Salamander Spring	Valles Caldera	Salamander Spring	This study	35.91970	-106.60230
Lake Spring-1	Valles Caldera	Lake Spring -1	This study	35.91721	-106.59445
Lake Spring-2	Valles Caldera	Lake Spring - 2	This study	35.91723	-106.59442
JS-SD-ML	Valles Caldera	Motherload	This study	35.792117	-106.686743
Bubbles Galore Spring	Valles Caldera	Bubbles Galore Spring	This study	35.91483	-106.58343
Footbath Spring	Valles Caldera, Sulphur Springs	Footbath Spring	Goff et al., 2002	35.9080448	-106.6155986
Tony's Spring	Valles Caldera, Sulphur Springs	Tony's Spring	Goff et al., 2002	35.907717	-106.615850
Men's Bath	Valles Caldera, Sulphur Springs	Men's Bath	Goff et al., 2002	35.906900	-106.616150
Women's Bath	Valles Caldera, Sulphur Springs	Women's Bath	Goff et al., 2002	35.906467	-106.616367
Main Fumarole	Valles Caldera, Sulphur Springs	Main Fumarole	Goff et al., 2002	35.90731	-106.616168
Soda Dam	Valles Caldera	Soda Dam	Goff et al., 2002	35.792117	-106.686743
Jemez Springs	Valles Caldera	Jemez Springs	Goff et al., 2002	35.772103	-106.690798
C Spring	Penasco Springs	Penasco Springs	Goff et al., 2002	35.60657	-106.88540
Baca wells (avg. of 5 wells)	Valles Caldera	minsep (7 msrmnts 5 wlls)	Goff et al., 2002	n.a.	n.a.
Jemez, VC-2a well	Valles Caldera	minsep	Goff et al., 2002	35.9075949	-106.615534
Jemez, VC-2b well	Valles Caldera	in situ	Goff et al., 2002	35.9075949	-106.615534
Baca Well 4	Vales Caldera	Baca Well 4	Truesdell and Janik, 1986	35.888989	-106.571063
Baca Well 13	Vales Caldera	Baca Well 13	Truesdell and Janik, 1986	35.896512	-106.568831
Baca Well 13	Vales Caldera	Baca Well 13	Truesdell and Janik, 1986	35.896512	-106.568831
Baca Well 15	Vales Caldera	Baca Well 15	Truesdell and Janik, 1986	35.893188	-106.580717
Baca Well 19	Vales Caldera	Baca Well 19	Truesdell and Janik, 1986	35.893188	-106.580717
Baca Well 24	Vales Caldera	Baca Well 24	Truesdell and Janik, 1986	35.885825	-106.581993
Baca Well 24	Vales Caldera	Baca Well 24	Truesdell and Janik, 1986	35.885825	-106.581993
Tierra Amarilla Anticline - unamed 1	Albuquerque Basin	San Ysidro	Newell et al., 2005	n.a.	n.a.
Tierra Amarilla Anticline - unamed 2	Albuquerque Basin	San Ysidro	Newell et al., 2005	n.a.	n.a.
Tierra Amarilla Anticline - unamed 3	Albuquerque Basin	San Ysidro	Newell et al., 2005	n.a.	n.a.
Tierra Amarilla Anticline - Grassy Spr	Albuquerque Basin	San Ysidro	Newell et al., 2005	35.5181	-106.844583
Tierra Amarilla Anticline - Blow-hole spr	Albuquerque Basin	San Ysidro	Newell et al., 2005	35.535790	-106.847830
Comanche Fault Spr - Salado arroyo	Albuquerque Basin	Carrizo Arroyo	Newell et al., 2005	34.690194	-107.106611
Comanche Fault - Salado Arroyo Stream	Albuquerque Basin	Carrizo Arroyo	Newell et al., 2005	35.697208	−106.122869
Comanche Fault -Salado Arroyo Spr	Albuquerque Basin	Carrizo Arroyo	Newell et al., 2005	35.697208	−106.122869
Tijeras Fault - Coyote Spr 1	Albuquerque Basin	Eastern ABQ Basin	Newell et al., 2005	34.998576	-106.471256
Tijeras Fault - Coyote Spr 2	Albuquerque Basin	Eastern ABQ Basin	Newell et al., 2005	34.998576	-106.471256
Eddleman Spr (to the W. of CA)	Colorado Plateau	Colorado Plateau	Newell et al., 2005	34.785887	-107.404114
Tunnel Spring – Sandia Pk	Sandia Mountains	Sandia Mountains	Newell et al., 2005	35.29161	-106.44001
Jemez Hot Spr	Jemez Mountains	Jemez Mountains	Newell et al., 2005	35.772103	-106.690798
Indian Hot Well - Jemez Pueblo	Penasco Springs	Penasco Springs	Newell et al., 2005	35.64555556	-106.8883333
Salt Spring - Jemez Pueblo	Albuquerque Basin	Albuquerque Basin	Newell et al., 2005	35.597759	-106.76047
San Antonio Hot Spr	Valles Caldera	Valles Caldera	Newell et al., 2005	35.939755	-106.64336

n.a. = not applicable, see authors notes
n.d. = non-detect
n.m = not measured
Assuming Ideal Gas law (PV = nRT)
AC = Alamo Canyon
MS = Mud Spring
LS = Lake Spring
WSS = White Smoker Spring
SS = Salamander Spring
BGS = Bubbles Galore Spring
SD = Mother load
RSS = Road Side Spring

SF = Surface Flux
PL = Parking Lot
BKG = Background
ZP = Zia Pueblo
SC = Silica Cemented
SY = San Ysidro
TMW = Twin Mounds West
TME = Twin Mounds East
LB = little Bubbler
DS = Dry Spring
HM = High Mound
GM = Grassy Mound

Appendix D: Results of Gas Samples Collected from Various Locations around the Albuquerque Basin and Valles Caldera

Sample ID	Source	Ar(%)	He(%)	N2(%)	O2(%)	CO2(%)	H2(%)	CH4(%)	CO(%)	H2S(%)	NH3(%)	Sum
JS-ZP-SC-BKG	This study	0.721	0.002	80.901	18.29	0.08	0.001	n.d.	0.004	n.m	n.m	100.0
JS-ZP-SC	This study	0.693	0.002	81.01	18.204	0.087	0.001	n.d.	0.004	n.m	n.m	100.0
JS-SY-BKG	This study	0.741	0.001	81.103	18.06	0.089	0.001	n.d.	0.005	n.m	n.m	100.0
JS-SY-LB	This study	0.788	0.382	80.794	17.942	0.089	0.001	n.d.	0.005	n.m	n.m	100.0
JS-SD-BKG-air	This study	0.736	0.002	80.751	18.414	0.091	0.001	n.d.	0.005	n.m	n.m	100.0
JS-SD-BKG	This study	0.721	0.004	80.579	18.432	0.236	0.023	n.d.	0.005	n.m	n.m	100.0
JS-SD-SF	This study	0.77	0.004	80.358	18.547	0.293	0.023	n.d.	0.005	n.m	n.m	100.0
JS-SD-Grotto	This study	0.721	0.001	80.549	18.17	0.552	0.001	n.d.	0.005	n.m	n.m	100.0
JS-SY-TMW	This study	0.687	0.014	81.693	17.021	0.581	0.001	n.d.	0.004	n.m	n.m	100.0
JS-SY-HM	This study	0.697	0.003	81.41	16.891	0.993	0.001	n.d.	0.005	n.m	n.m	100.0
JS-SY-GM	This study	0.692	0.006	81.281	16.967	1.029	0.02	n.d.	0.005	n.m	n.m	100.0
JS-SD-PL	This study	0.707	0.002	79.75	18.123	1.412	0.001	n.d.	0.005	n.m	n.m	100.0
JS-SY-TME	This study	0.727	0.022	80.101	17.544	1.582	0.02	n.d.	0.004	n.m	n.m	100.0
JS-SY-DS	This study	0.641	0.008	80.401	16.845	2.1	0.001	n.d.	0.004	n.m	n.m	100.0
Mud Spring	This study	0.762	0.002	78.779	18.238	2.215	0.001	n.d.	0.003	n.m	n.m	100.0
White Smoker Spring	This study	0.702	0.004	77.935	18.128	3.202	0.025	0.001	0.004	n.m	n.m	100.0
JS-SD-RSS	This study	0.72	0.002	77.96	18.049	3.244	0.02	n.d.	0.005	n.m	n.m	100.0
Salamander Spring	This study	0.73	0.006	77.676	18.243	3.314	0.026	0	0.005	n.m	n.m	100.0
Lake Spring-1	This study	0.738	0.01	75.207	18.206	5.781	0.032	0.019	0.006	n.m	n.m	100.0
Lake Spring-2	This study	0.664	0.011	73.548	17.112	8.636	0.024	n.d.	0.005	n.m	n.m	100.0
JS-SD-ML	This study	0.638	0.002	68.838	16.266	14.248	0.002	n.d.	0.006	n.m	n.m	100.0
Bubbles Galore Spring	This study	0.516	0.015	52.096	12.58	34.656	0.082	0.045	0.01	n.m	n.m	100.0
Footbath Spring	Goff et al., 2002	0.011	0.012	0.62	0.03	97.9	0.48	0.064	n.m.	0.87	0.0012	100.0
Tony's Spring	Goff et al., 2002	0.0081	0.005	0.42	0.007	98.8	0.29	0.022	n.m.	0.48	0.0013	100.0
Men's Bath	Goff et al., 2002	0.016	0.0066	0.89	0.033	98.3	0.17	0.021	n.m.	0.52	0.0011	100.0
Women's Bath	Goff et al., 2002	0.01	0.004	0.69	0.0041	98.5	0.1	0.016	n.m.	0.71	0.0017	100.0
Main Fumarole	Goff et al., 2002	0.0055	0.0048	0.25	0.0016	99	0.044	0.033	n.m.	0.77	0.0017	100.1
Soda Dam	Goff et al., 2002	0.02	0.002	1.1	0.32	98.4	0.005	0.004	n.m.	0.02	0.002	99.9
Jemez Springs	Goff et al., 2002	0.012	0.0011	0.71	0.14	99.1	0.0001	0.005	n.m.	0.063	0.0008	100.0
C Spring	Goff et al., 2002	0.05	0.040	1.97	0.14	97.7	<0.005	0.004	n.m.	<0.02	n.d.	99.9
Baca wells (avg. of 5 wells)	Goff et al., 2002	0.013	0.0038	0.47	0.04	98.8	0.062	0.020	n.m.	0.47	0.029	99.9
Jemez, VC-2a well	Goff et al., 2002	0.016	0.002	0.9	0.0005	97.1	0.25	0.017	n.m.	0.72	0.84	99.9
Jemez, VC-2b well	Goff et al., 2002	0.0066	0.0051	0.29	0.11	96.9	1.85	0.24	n.m.	0.81	n.d.	100.2
Baca Well 4	Truesdell and Janik, 1986	0.0083	0.0067	0.353	n.m.	98.5	0.0645	0.0393	n.m.	0.995	0.027	100.0
Baca Well 13	Truesdell and Janik, 1986	0.0042	0.0042	0.142	n.m.	99.3	0.0403	0.0207	n.m.	0.482	0.018	100.0
Baca Well 13	Truesdell and Janik, 1986	0.0058	0.0054	0.181	n.m.	99.2	0.0494	0.0244	n.m.	0.534	0.017	100.0
Baca Well 15	Truesdell and Janik, 1986	0.027	0.0022	1.13	n.m.	96.7	0.14	0.0253	n.m.	1.77	0.071	99.9
Baca Well 19	Truesdell and Janik, 1986	0.015	0.0061	0.572	n.m.	98.4	0.106	0.0633	n.m.	0.806	0.049	100.0
Baca Well 24	Truesdell and Janik, 1986	0.017	0.0016	0.721	n.m.	98.5	0.0542	0.018	n.m.	0.672	0.042	100.0
Baca Well 24	Truesdell and Janik, 1986	0.013	0.0018	0.679	n.m.	98.4	0.0323	0.0085	n.m.	0.778	0.096	100.0
Tierra Amarilla Anticline - unamed 1	Newell et al., 2005	0.247	0.774	13.0	0.419	81.6	<3.41E-04	0.146	n.m.	3.71	n.m.	99.9
Tierra Amarilla Anticline - unamed 2	Newell et al., 2005	0.0769	<3.99E-04	6.36	1.72	91.5	0.0131	<9.64E-05	n.m.	n.d.	n.m.	99.7
Tierra Amarilla Anticline - unamed 3	Newell et al., 2005	0.0586	0.0572	2.47	0.0942	85.2	0.00205	<5.94E-05	n.m.	12.1	n.m.	100.0
Tierra Amarilla Anticline - Grassy Spr	Newell et al., 2005	0.00881	0.00869	0.729	0.106	98.6	<1.86E-05	3.57E-04	n.m.	0.57	n.m.	100.0
Tierra Amarilla Anticline - Blow-hole spr	Newell et al., 2005	1.73E-02	<3.92E-05	1.43	0.153	98.4	1.10E-04	7.63E-04	n.m.	n.d.	n.m.	100.0
Comanche Fault Spr - Salado arroyo	Newell et al., 2005	0.873	<1.84E-03	72.1	17.7	7.19	3.61E-03	<4.43E-04	n.m.	2.11	n.m.	100.0
Comanche Fault - Salado Arroyo Stream	Newell et al., 2005	0.757	0.02	62.6	16.8	19.9	1.05E-02	<4.16E-04	n.m.	n.d.	n.m.	100.1
Comanche Fault -Salado Arroyo Spr	Newell et al., 2005	0.783	6.19E-03	64.7	15.9	18.6	6.28E-03	<4.25E-04	n.m.	n.d.	n.m.	100.0
Tijeras Fault - Coyote Spr 1	Newell et al., 2005	0.55	<1.15E-03	45.5	10.8	43.2	4.02E-03	<2.78E-04	n.m.	n.d.	n.m.	100.1
Tijeras Fault - Coyote Spr 2	Newell et al., 2005	0.0743	7.03E-04	6.14	1.66	92.1	7.36E-04	<3.38E-05	n.m.	n.d.	n.m.	100.0
Eddleman Spr (to the W. of CA)	Newell et al., 2005	<2.26E-04	<1.67E-04	0.887	<2.19E-04	99.1	1.17E-03	5.53E-03	n.m.	n.d.	n.m.	100.0
Tunnel Spring – Sandia Pk	Newell et al., 2005	0.947	<2.04E-03	78.3	6.97	13.8	8.02E-03	<4.93E-04	n.m.	n.d.	n.m.	100.0
Jemez Hot Spr	Newell et al., 2005	0.668	<1.18E-03	55.2	16.4	26.7	6.84E-03	<2.86E-04	n.m.	1.02	n.m.	100.0
Indian Hot Well - Jemez Pueblo	Newell et al., 2005	0.521	0.0915	43.1	10	46.3	<2.80E-04	0.0296	n.m.	n.d.	n.m.	100.0
Salt Spring - Jemez Pueblo	Newell et al., 2005	<2.96E-04	1.51E-03	1.53	<2.93E-04	98.4	8.42E-04	5.08E-02	n.m.	n.d.	n.m.	100.0
San Antonio Hot Spr	Newell et al., 2005	0.935	<2.92E-03	77.3	16.4	5.34	0.0127	<7.05E-04	n.m.	n.d.	n.m.	100.0

n.a. = not applicable, see authors notes
n.d. = non-detect
n.m = not measured
Assuming Ideal Gas law (PV = nRT)
AC = Alamo Canyon
MS = Mud Spring
LS = Lake Spring

SF = Surface Flux
PL = Parking Lot
BKG = Background
ZP = Zia Pueblo
SC = Silica Cemented
SY = San Ysidro
TMW = Twin Mounds West

WSS = White Sm
SS = Salamander
BGS = Bubbles Ga
SD = Mother loa
RSS = Road Side

TME = Twin Mounds East
LB = little Bubbler
DS = Dry Spring
HM = High Mound
GM = Grassy Mound